Focused Laser Differential Interferometry: Recent Developments and Applications for Flow Measurements

Elizabeth K. Benitez*
U.S. Air Force Research Laboratory, Wright-Patterson AFB, OH 45433, USA

Andrew P. Ceruzzi†
Oxford Thermofluids Institute, University of Oxford, Oxford, OX2 0ES, United Kingdom

Mark Gragston‡
The University of Tennessee-Knoxville, Knoxville, TN 37996 USA

Nicholaus J. Parziale§
Stevens Institute of Technology, Hoboken, NJ 07030, USA

Bryan E. Schmidt¶
Case Western Reserve University, Cleveland, OH 44106, USA

Joshua M. Weisberger‖
NASA Langley Research Center, Hampton, VA 23681, USA

Focused laser differential interferometry (FLDI), first introduced in the 1970s, has developed into a powerful tool for the analysis of turbulent dynamics and fluctuations in fluid flows ranging from subsonic to hypersonic. This paper provides a review of recent FLDI developments and applications, including discussions on the basic theory of the instrument, various forms of FLDI, multi-point techniques, utilization in fluid flow measurements, quantitative measurement capabilities, and more.

Distribution Statement A: Approved for Public Release; Distribution is Unlimited. PA# AFRL-2024-6450; Cleared 11/19/2024.

Contents

I Introduction **2**

II Design and Setup of a Focused Laser Differential Interferometer **6**
II.A Basic FLDI Design and Setup 6
II.B Practical Setup and Design Considerations 8
II.C FLDI with Cylindrical Lenses 11
II.D Polarizing Prisms 13

III FLDI Theory and System Analysis **14**
III.A Relation Between Voltage and Phase Difference 14
III.B Relation Between Phase Difference and Refractive Index 15
III.C Spatial Resolution 18
III.D Experimental Validation of Theory 20

*Research Aerospace Engineer, High-Speed Aerodynamics Branch, AIAA Senior Member.
†Postdoctoral Research Assistant, Department of Engineering Science, University of Oxford, AIAA Member.
‡Assistant Professor, Mechanical, Aerospace, and Biomedical Engineering, AIAA Senior Member
§Associate Professor, Mechanical Engineering, AIAA Associate Fellow.
¶Assistant Professor, Mechanical and Aerospace Engineering, AIAA Senior Member.
‖Research Engineer, Advanced Measurements and Data Systems Branch, AIAA Senior Member.

III.E Signal Interpretation and Post-Processing Guide . . . 23
III.E.1 Prior to the experiment . . . 23
III.E.2 Prior to each test/run/shot . . . 23
III.E.3 Post-test . . . 23

IV Multi-Point FLDI Techniques 24
IV.A Additional Birefringent Prisms . . . 25
IV.B Cylindrical Optics Line FLDI . . . 26
IV.C Diffractive Optical Elements for Linear Array FLDI . . . 27
IV.D Microlens Array . . . 29
IV.E Spatial Light Modulator . . . 30
IV.F Scanning Point FLDI . . . 30
IV.G Multi-Point Data Acquisition . . . 31
IV.H Parallel Beam Propagation . . . 31

V Applications of FLDI for Flow Measurements 32
V.A Jets . . . 33
V.B Transitional and Turbulent Boundary Layer Flows . . . 34
V.C Wind Tunnel Freestream Turbulence . . . 35
V.D Reacting, High-Temperature Flows . . . 36

VI Computational and Quantitative FLDI 37
VI.A Ray Tracing Model . . . 38
VI.B Transfer Functions . . . 38
VI.C Computational FLDI Applications . . . 41

VII Specialized FLDI Configurations 44
VII.A Combined FLDI and Schlieren Imaging . . . 44
VII.B FLDI through Curved Windows . . . 46
VII.C Chromatic FLDI . . . 47
VII.D Mach-Zehnder Configuration . . . 50
VII.E Absorption Laser Differential Interferometry . . . 50
VII.F Miscellaneous Configurations . . . 51

VIII Perspective on Future Development and Applications 51

I. Introduction

The first publicly available description of a laser differential interferometer (LDI) for gas dynamics measurements is provided by G. Smeets and A. George in a technical report from the French-German Research Institute of Saint Louis (ISL) published in 1971 and translated from German to English by Andreas Goetz of Purdue University in 1996 [1]. The shock tube laboratory at ISL, led by Herbert Oertel [2], was a pioneer for many optical diagnostics, including differential interferometers which are mentioned in reports as early as 1961 [3]. As described by Smeets and George, the LDI was developed to interrogate low density flow fields where interferogram visualizations are not possible. Compared to previous interferometers, unique components of an LDI included a continuous wave (CW) laser (HeNe in this case), Wollaston prisms, and a photodiode which offered advantages in signal-to-noise, and spatial and temporal resolution while reducing the measurement domain to effectively a single "point". Figure 1 shows a simplified schematic of an LDI system. For cases where more spatial information is necessary, Smeets and George modified LDI using additional prisms and polarizers to enable multiple (up to 8) measurement points. Like many other optical techniques, the LDI is path-integrated and provides no spatial resolution along the optical axis (z-axis in Fig.1). To mitigate this, Smeets published another report in the same year (1971) detailing a modified LDI with "large diameter light bundles" which are focused to a region of interest [4]. This modification, now called focused laser differential interferometry (FLDI), has the effect of maximizing the instrument's sensitivity at the focus while reducing it away from the focus, thereby improving the spatial resolution of the technique in comparison with the non-focusing LDI

system. Figure 2 shows a simplified schematic of an FLDI set-up. Smeets and George published several articles on LDI and FLDI in the 1970s [5, 6] including a comprehensive ISL internal report in 1973 which was also translated by Andreas Goetz in 1996 [7]. This report discusses fundamental principles, optical arrangements, sensitivity, spatial resolution, multi-beam arrangements, applications in hypersonic flows and many more topics concerning LDI and FLDI. Many of the ideas, experimental arrangements, and applications published to this day were first suggested by Smeets and George. Per Smeets [5, 6], "G. Smeets was born in Rheydt, Germany, on May 28, 1935. He received the Physics Diploma and Doctorate degree from the University of Freiburg, Germany, in 1962 and 1964, respectively. Since 1964 he has been with the staff of the German-French Research Institute (ISL), Saint-Louis, France, where he is engaged with gasdynamics and aerodynamics. In resolving the experimental problems in this field, he has developed a variety of optical techniques." This review is dedicated to Smeets.

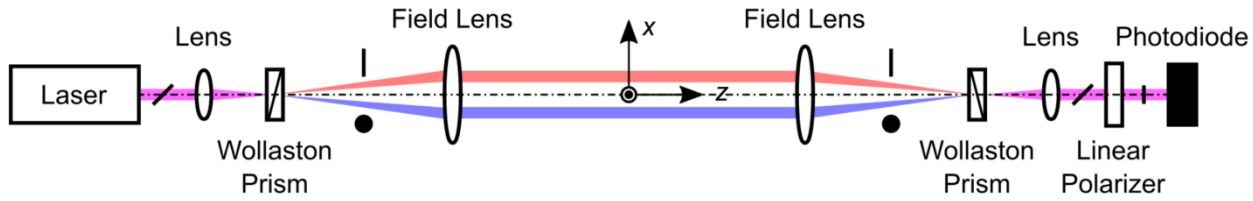

Fig. 1 Schematic of a non-focusing laser differential interferometer (LDI), with pitch side of instrument on the left and catch side on the right.

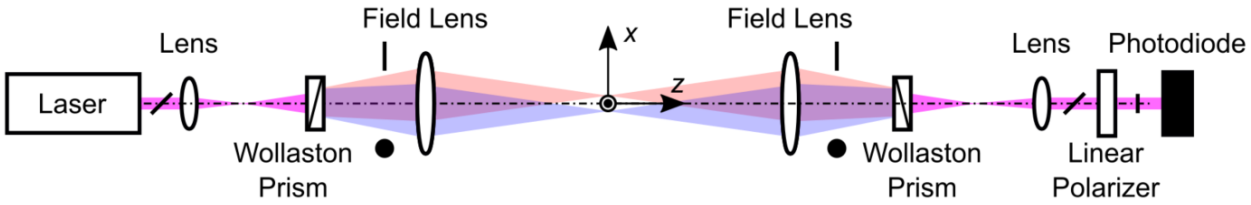

Fig. 2 Schematic of a focused laser differential interferometer (FLDI), with pitch side of the instrument on the left and catch side on the right.

The primary advantages of LDI over other non-intrusive techniques are:

1) **Speed**: photodiodes allow high-bandwidth measurement of fluctuations > 10 MHz
2) **Sensitivity**: interferometry techniques are sensitive enough to detect fluctuation amplitudes $< 10^{-4}$ kg/m^3, enabling measurement of weak instability waves and freestream turbulence
3) **Spatial Resolution**: Resolution below 100 μm is easily achieved along the axes orthogonal to the optical axis. FLDI has the added benefit of spatial resolution along the optical axis which allows measurements in the core flow of wind tunnels

These attributes make LDI and FLDI well suited for probing harsh, high velocity flows with short test times as well as instabilities and small-scale turbulent fluctuations which are weaker and higher frequency than the large scales. Such flows and scales are encountered in hypersonic boundary layer transition experiments where freestream disturbances, receptivity to these disturbances, and growth of instabilities are all important [8–13]. LDI was applied sparsely from 1980 to 2010 to detect boundary layer transition [14, 15] and to study blunt body receptivity [16, 17]. In the early 2010s, Parziale *et al.* [18–21] used FLDI to measure boundary layer instabilities in excess of 1 MHz as well as freestream disturbances in Caltech's T5 Hypervelocity facility. As an example of FLDI's ability to reject off-focus signals, Parziale [19] used a CO_2 jet to assess RMS response versus focus; this data, shown in Fig. 3, indicates that just 15 mm from the sharp focus, the FLDI setup is relatively insensitive to the broadband response of the CO_2 jet.

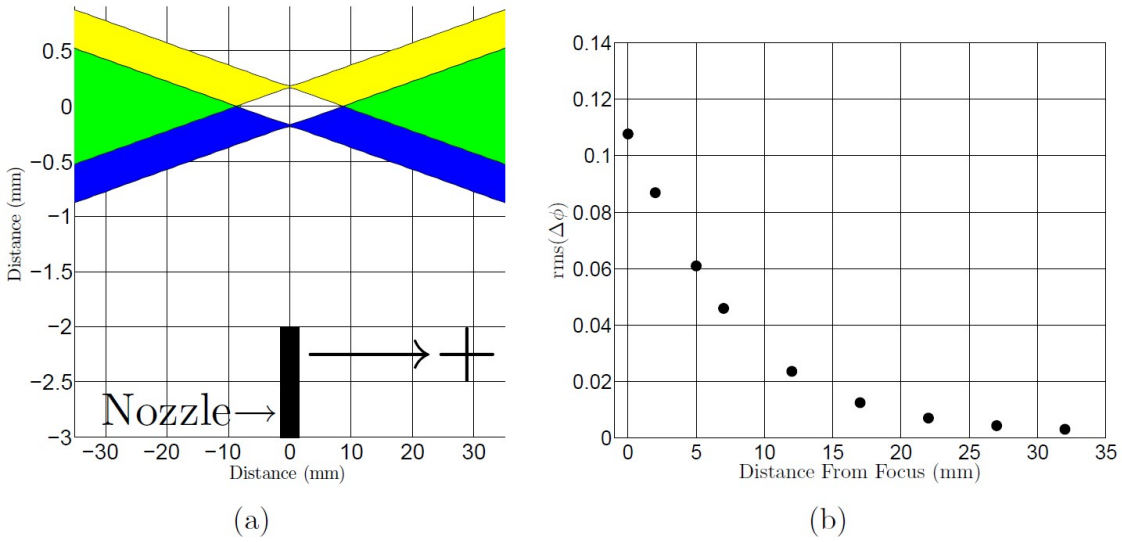

Fig. 3 (a) Schematic of the small CO_2 nozzle and laser beam profile, with the arrow denoting the direction of nozzle traversal. The yellow and blue shaded areas denotes where the laser is polarized either along the streamwise direction or normal to the page, respectively. The green shaded region denotes the area where the two laser beams overlap. (b) Results of the bench test, demonstrating the decrease in response of the FLDI with increasing distance from the tightly-focused sensitive region. Used with permission of N. Parziale [19].

The first results from Parziale *et al.* [18], reproduced here in Fig. 4a, illustrated that FLDI could be used to measure the second mode in a facility like T5. At that time, the stability and transition community was skeptical of this result. Questions included: Were the extreme frequencies at which the second mode was most amplified (> 1 MHz) being confused with high-frequency RF noise? Also, what was the transition mechanism for a slender body in hypervelocity flow generated by an allegedly 'noisy' free-piston, reflected-shock tunnel? The former question was valid. Several AM

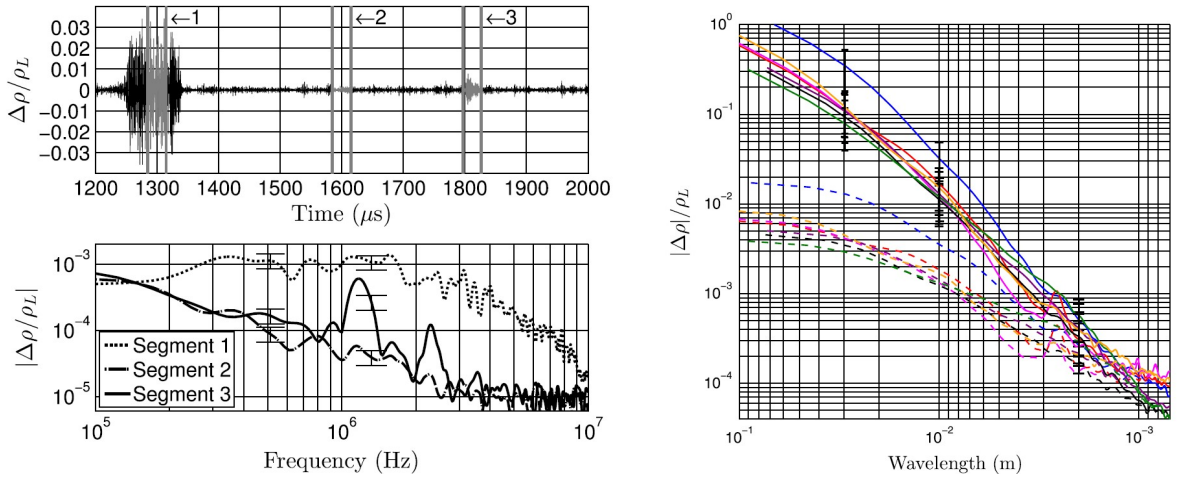

Fig. 4 (a) FLDI results from shot 2702: the processed response (top) and spectral response from the three chosen segments (bottom) [18]. (b) Wavelength spectrum of tunnel noise time traces for a range of T5 run conditions. The lower amplitude data (dashed lines) have not been corrected for the sensitivity of the FLDI technique to wavelength, while the higher amplitude data (solid lines) have been corrected for the sensitivity of the FLDI technique to wavelength [20].

radio stations broadcasting from Mount Wilson were unfortunately right at the estimated second mode frequency. Care regarding wire placement and signal termination helped reduce these concerns. The second question was addressed with facility noise measurements, shown here in Fig. 4b, where the peaks between 2 mm and 3 mm are RF spikes that are registered when the tunnel is not in operation.

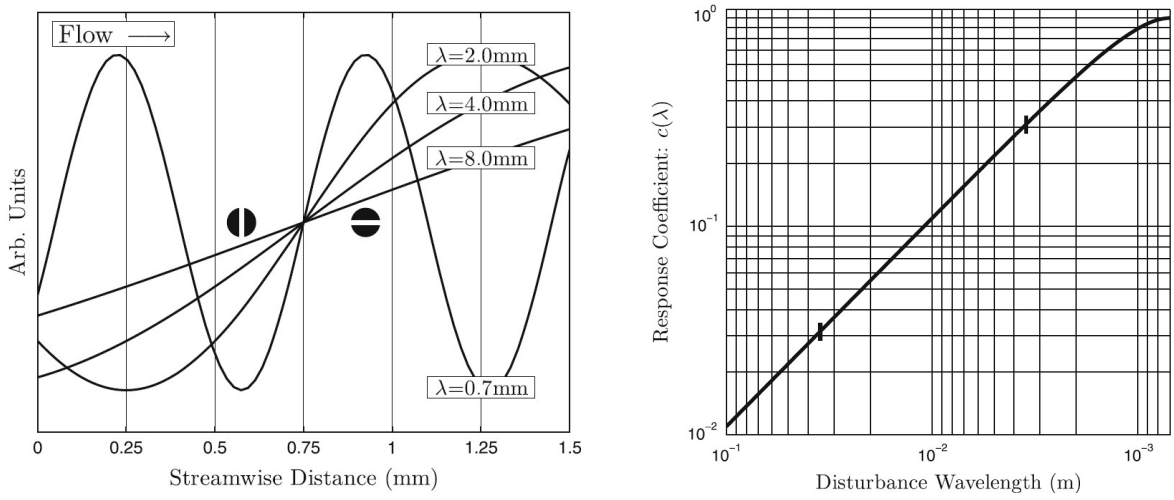

(a) **(b)**

Fig. 5 (a) Four sine waves representative of density disturbances of equal amplitude with wavelengths: 0.7, 2, 4, and 8 mm, with two circles representing the beam polarized in the streamwise and spanwise direction, denoted by the horizontal and vertical lines though the circles, respectively. (b) Plot of the response coefficient as a function of wavelength. The error bars here represent the error due to the beam spacing. Figures reproduced from Ref. [20].

In that paper, Parziale *et al.* [20] also introduced a correction for the dependence on wavelength, shown in Fig. 5. In Fig. 5a, the streamwise direction is from left to right while the spanwise direction is into and out of the page. The four sine waves shown are representative of density disturbances of equal amplitude with wavelengths of 0.7, 2, 4, and 8 mm, and the two circles represent the beam polarized in the streamwise and spanwise direction, denoted by the horizontal and vertical lines though the circles, respectively. In Fig. 5b, the response coefficient is plotted as a function of the wavelength, demonstrating the behavior of reduced response with increasing disturbance wavelength.

More complete analysis of the second mode was reported in Parziale *et al.* [21], shown here in Fig. 6. In Fig. 6a, a head-on view of a cone is shown, where the cone tip is located out of the page, and where the FLDI measurement volume was located within the boundary layer of the cone. Lines on the plot include the cone surface (solid thick line), the calculated boundary-layer thickness for shot 2789 (dashed line), density eigenfunction for shot 2789 (solid thin lines), and the laser beam profile (gray filled area), where the focus of the beam is located at the zero of the abscissa. The power spectral density estimates for two high enthalpy air shot series are plotted in Fig. 6b, showing differences in the amplitude of the narrow-band disturbance near 1.2 MHz, increasing with increasing unit Reynolds number, and which are consistent with the instability mode described by Mack [22]. Figure 6c plots the computed linear-stability diagram and experimental spectra for a high enthalpy shot, where the shaded area is the unstable region, and darker shading indicates larger negative imaginary wavenumber (spatial growth rate). The circular markers represent the maximum in $\Delta\rho/\rho_{\mathrm{L}}$ from the PSD estimates, and the black line represents full-width at half-maximum of the peak in the power spectral density.

These successful experiments exploited all of FLDI's advantages and set an example for the hypersonics research community. In the years to follow, a renewed interest in hypersonics research caused the use of FLDI to skyrocket. From 2014 to the present, labs across the globe have employed FLDI with over a hundred publications employing or exploring the technique. The aim of this paper is to review these recent developments. A general introduction to the FLDI instrument is provided in Section II, including guidelines and practical considerations when assembling a system, a brief overview of its use with cylindrical lenses, and a summary of the beam splitting options. Methods for analyzing

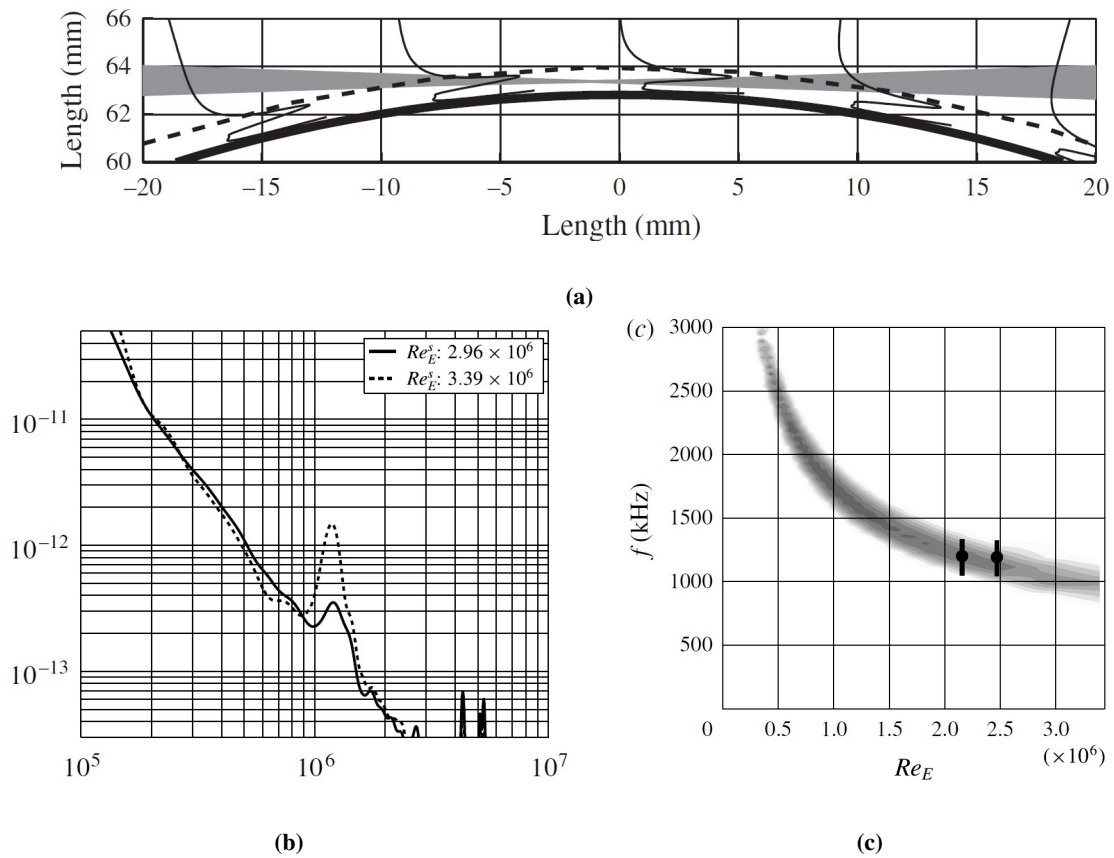

Fig. 6 (a) FLDI measurement volume located within the boundary layer of a cone, with overlay of the cone surface (solid thick line), calculated boundary-layer thickness for shot 2789 (dashed line), density eigenfunction for shot 2789 (solid thin lines), and laser beam profile (gray filled area). (b) Power spectral density estimates for the high-enthalpy air shot series. (c) Computed linear-stability diagrams and experimental spectra for a high enthalpy shot. Figures reproduced from Ref. [21].

and interpreting the data acquired with the FLDI system are described in Section III. The conversion of a conventional single-point FLDI system to a multi-point system is described in Section IV, and applications of FLDI for a variety of fluid flows are given in Section V. The use of computational simulations to simulate the FLDI system and its response to fluid flows is discussed in Section VI, and recent specialized applications and configurations of the FLDI system are outlined in Section VII. Finally, a brief overview of the perspective for future development and application of the FLDI system is provided in Section VIII.

II. Design and Setup of a Focused Laser Differential Interferometer

While many versions of the FLDI instrument exist, this section describes the design and setup of a basic system (Section II.A) and the practical considerations to be aware of during the alignment process (Section II.B). The inclusion of cylindrical lenses in the FLDI system is discussed in Section II.C, allowing for near-surface measurements of wide, flat geometries. Finally, the various polarizing prism options currently in use are outlined in Section II.D.

A. Basic FLDI Design and Setup

The aim of this subsection is to describe the design and setup of the most common, basic form the FLDI instrument. A detailed discussion of an FLDI system design and setup is provided by Neet *et al.* [23], which can be consulted

for further setup and design information. Being a simpler setup, and the instrument upon which the FLDI is based, a description of the LDI system is first outlined, using the schematic of Fig. 1, with what is typically termed the *pitch side* of the system on the left, and the *catch side* of the system on the right. The collimated light from the laser is first focused by a plano-convex lens. Without the Wollaston prism present in the system, the beam continues to expand past its focal point, and if the focal point of the beam expander lens is placed at the focal point of the field lens, the beam remains collimated as it travels along the optical axis (z-axis) of the system. A Wollaston prism is placed at the focal point of the pitch side beam expander lens and field lens, such that the incident beam is split into two orthogonal linearly polarized beams, traveling away from each other at a fixed divergence angle. The amount of laser power split to each beam depends on the incoming polarization state of the beam at the Wollaston prism. If using linearly polarized light (such as that typically emitted from a laser), the polarization should be oriented at 45° relative to the splitting axis of the beams from the Wollaston for equal power splitting. This is shown in the schematic of Fig. 1 by the diagonal line at the exit of the laser, indicating 45° linear polarization, which is then split equally into horizontal and vertical polarization beams (line and dot). If the output from the laser is not correctly oriented relative to the Wollaston prism, a half-wave plate can rotate the linear polarization state to any desired angle, or a linear polarizer can be used. If a quarter-wave plate is used instead, the beam can be made to be circularly polarized, and the splitting at the Wollaston will result in equal power beams. Because the Wollaston prism is also placed at the focal point of the field lens, the two beams travel parallel to one another until reaching the catch side field lens, which then focuses both beams down to the focal point of the lens, where a matching Wollaston prism is placed, making the beams colinear with each other once again. A second lens on the catch side collimates the colinear beams, and a linear polarizer is used to make the beams interfere before the light is incident on a photodiode. Density fluctuations that cause an optical path length difference between the split beams results in changes in the intensity measured by the photodiode.

The method of converting an LDI system to an FLDI system is simple, requiring only a shift of the optics relative to one another along the optical axis (z-axis in the schematics). The schematics of Fig. 2 and Fig. 7 show simple FLDI systems, with the only difference being the choice of beam expanding lens being used; Fig. 2 uses a plano-convex lens to first focus and then expand the beam, while Fig. 7 uses a plano-concave lens to only expand the beam without first focusing it. The focal point of the beam expander lens has now been shifted farther away from the fields compared to its position in the LDI system. Now, instead of the beams being collimated after passing through the field lens, they focus down to a point between the field lens, at a distance that can roughly be computed using the thin lens equation. The position of the Wollaston prism remains the same as in the LDI system, located at the focal point of the field lens, such that the two orthogonally polarized beam travel between the field lenses parallel to one another, even while focusing and expanding. Because the two orthogonally polarized beams have a finite angular deviation as they exit the Wollaston prism, they have a finite separation as they traverse the path between the field lenses, Δx, a key aspect of the FLDI system. The beam separation is related to the prism splitting angle and the field lens focal length, f_{FL}, by:

$$\Delta x = 2 f_{\mathrm{FL}} \tan\left(\frac{\epsilon}{2}\right) \approx f_{\mathrm{FL}} \epsilon \tag{1}$$

The splitting angle ϵ is typically very small (< 10 arcmin in most applications); thus, the small angle approximation is appropriate. For the catch side, the optics are effectively mirrored, with a matching plano-convex field lens collecting the beams and focusing them through the catch-side Wollaston prism. It is important to note that identical field lenses and Wollaston prisms should be used on the receiving side, which are necessary to ensure the beams optimally recombine (i.e., are made exactly colinear). Following the second Wollaston prism, a polarizer is used to make the colinear beams interfere and produce a fringe pattern. A lens is also often used to focus the light to the appropriate size on a photodetector. An alternative setup using a polarizing beamsplitter and two photodetectors has also been used [24–29]. Although this setup has advantages in noise rejection and signal interpretation, it is more seldom used.

It is advised that ray tracing calculations be performed to quickly examine how optic choices and positioning affect the light path (for example, see simple MATLAB™ code in [30]). For wind tunnels, the system needs to be designed such that the test section fits between the two field lenses. If using a setup similar to that in Fig. 7 with beam expander lens of focal length f_{BE} and field lenses of focal length f_{FL}, the spacing between the two field lenses, S, can be analytically computed as:

$$S = 2\left[\frac{1}{f_{\mathrm{FL}}} - \frac{1}{d - f_{\mathrm{BE}}}\right]^{-1} \tag{2}$$

The distance d is the spacing between the expansion lens and the first field lens. While there is a large degree of flexibility for spacing lenses, consideration must also be given to the size of the expanded beam when it reaches the

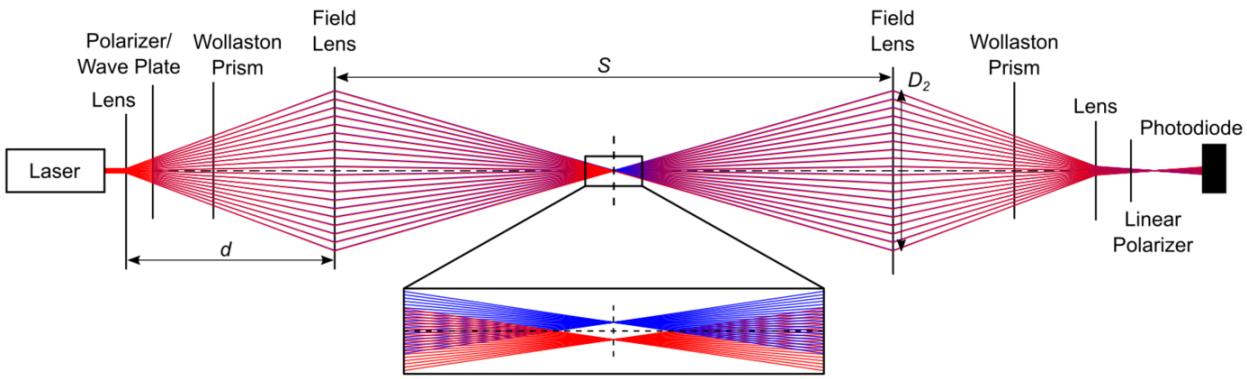

Fig. 7 The optical layout and ray trace of a basic FLDI system, including the following components: (1) Laser, (2) plano-concave lens for beam expansion, (3) polarizer or half-wave plate, (4) Wollaston prism, (5) plano-convex field lenses, (6) secondary plano-concave lens, and (7) photodetector.

first field lens since the local beam diameter should not exceed the clear aperture of the lens when mounted. Again, assuming a setup like that described in Fig. 7, for a given input beam diameter D_{BE} into the expansion lens of focal length f_{BE}, the beam diameter D_{FL} at the subsequent field lens will be:

$$D_{\mathrm{FL}} = D_{\mathrm{BE}} \frac{d - f_{\mathrm{BE}}}{|f_{\mathrm{BE}}|} \tag{3}$$

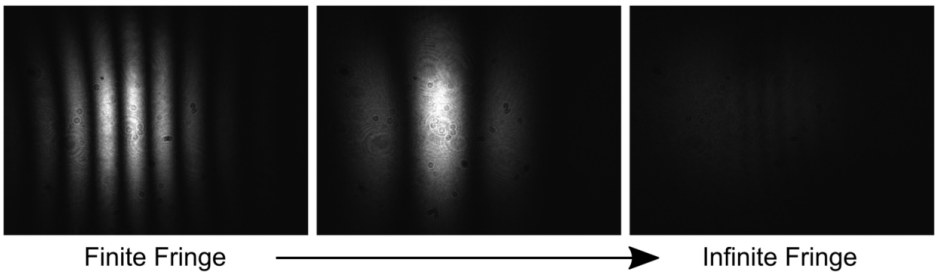

Fig. 8 Images of the fringe pattern produced as the recombination Wollaston prism is moved along the optical axis. Note the phase of the fringe will determine if the infinite fringe appears totally dark, totally bright, or somewhere in between.

It is also important to note that the position of the catch-side Wollaston prism is set to provide an infinite fringe condition, which is shown in Fig. 8. The infinite fringe condition provides the optimal response and minimizes phase wrapping effects from nearby fringes. The phase of the FLDI system should also be set such that measurements are in the linear region, which corresponds to half-way between complete constructive interference and complete destructive interference (see Fig. 11 in Section III.A).

B. Practical Setup and Design Considerations

There is great variability in the setup of an FLDI instrument from one research group to the next. Different optics can be used to accomplish the same task, and setup-specific space limitations dictate the use of certain optics over others. However, all systems must be assembled to be rigid, since the interferometric signal measured at the photodiodes will be affected by any vibrations of the optics, and of the pitch and catch boards relative to one another. If constructing the FLDI system in a laboratory that is to be transferred to a wind tunnel facility, for example, the optics for the pitch and catch portions must be fixed relative to each other. One option is to use robust optical rails, while another is to use optical cage system hardware. Final alignment of the system at the wind tunnel must always be performed to ensure its operation matches that of the initial setup in the laboratory. Vibration isolation/suppression when installed at the wind

tunnel facility will help maintain alignment of the system throughout long testing campaigns.

Initial Beam Centering on the Optical Axis

A critical aspect of the system setup is to ensure the laser beam travels along a straight path, centered in the optics. Even a small offset/angling of the beam will result in substantial offsets/angles of the beam later in the system. The first step in setting up the system should thus be to align the laser beam along the system's optical axis. One method to ensure alignment is to use two irises set to the exact same height (e.g., by adjusting their height at a common location, usually the laser exit) and to adjust the height/angle of the laser such that it passes through both irises along the optical axis. Another method is to use two 90° turning mirrors to fold the laser beam path 180° from its initial orientation. This allows a "beam-walk" to be performed using both mirrors in an iterative sequence, ensuring the beam is exactly aligned with the optical axis. This method works best when using cage optics for the construction, since drop-in alignment targets can be placed anywhere along the beam path cage rods, and act as pre-set iris apertures. This alignment can be performed to ensure the pitch and catch sides of the system are in alignment with each other, both in translation and rotation (with all optics removed but irises or alignment targets in place). Once this initial alignment of the laser along the optical axis has taken place, other optics can be added.

Initial Lens Placement

The beam expander lens and field lenses can now be added to the system. Their initial placement can be estimated using the thin lens equation, although note that some adjustment will be required from these positions as other optics are added (and because the lenses are not infinitesimally thin). The focal point of the beam expander lens is placed at a distance away from the field lens such that the required distance from the field lens to the test section focus point is obtained. After adding the field lens, this distance can be easily verified with a tape measure. If the beams will pass through a window prior to focus (e.g., a wind tunnel window), it is helpful to have the window in place since its inclusion will alter the focus point of the beam. This is not always feasible since wind tunnels may not have spare windows; final alignment can always be performed after installation of the system at the wind tunnel, and having the beam expander lens on a micrometer adjustment translation stage is particularly helpful to make the small adjustments that will be necessary. The position of the catch-side assembly can now be placed relative to the beam focus, and the position at which the beam focuses after passing through the catch-side field lens should match the distance from the pitch side of the system (and can be verified with a tape measure). The second lens on the catch side of the system can be included now, to ensure the correct size of the beam on the photodiode. During the alignment, care should be taken to make sure none of the optics are twisted, as this can lead to non-Gaussian beams at the focus.

Use of Translation and Rotation Stages

In addition to the translation stage for the beam expander lens along the optical axis, it is helpful to have this lens mounted in a two-axis translation mount to allow for lens centering on the optical axis. As mentioned earlier, small shifts in the optics relative to the laser on the optical axis can have large implications later in the system, and having precise control over the beam expander position along three axes is helpful. If using the Wollaston prism for phase adjustment (discussed further below), this too should be mounted on a stage that can translate orthogonal to the optical axis, along the same direction as the splitting axis of the beams. If the orientation of the Wollaston beams are to be rotated to be sensitive to different directions in the flow, both Wollaston prisms should be placed in rotation mounts. Any wave plates and/or linear polarizers should also be placed in rotation mounts such that precise angles of these optics can be set. For example, the rotation of the pitch-side half-wave plate or linear polarizer needs to be precisely set to ensure equal splitting of power at the Wollaston prism. If the beams have different power levels, it will be difficult to achieve maximum destructive interference at the catch-side linear polarizer. The catch-side linear polarizer also requires fine rotation adjustment in order to place the voltage level at the position of the middle of the infinite interference fringe. Spherical lenses do not need to be placed in rotation stages, but if cylindrical lenses are being used (see Section II.C and Section IV.B), these should be placed in rotation mounts to enable adjustments of the beam and to ensure the beams do not change shape through the test section.

Infinite Fringe Polarization Adjustment

When nearly finished aligning the FLDI system, it may be noticed that the rotation of the final linear polarizer does

not bring the voltage measured by the photodiode down to near zero values. This can also be seen by removing the photodiode and allowing the beam to continue expanding to a sheet of paper, where rotation of the linear polarizer increases and decreases the intensity seen, but never reaches a true minimum. It can be helpful to shift the catch-side Wollaston prism along the optical axis in either direction to a finite fringe condition to see this effect. This indicates that the polarization of the light just upstream of the linear polarizer is not linearly polarized. It may be anticipated that in an ideal FLDI system, the beams split at the first Wollaston prism originate from the same beam, and are thus in phase with each other, albeit orthogonally polarized relative to each other. At the second Wollaston prism, they are made to be colinear, are still in phase, and when made to interfere with each other, will have a linear polarization just as they had prior to the first Wollaston splitting. In practice, two main things affect the phase between the two orthogonally polarized beams which induces ellipticity in the recombined and interfered beams. The first is the slightly different path of the beams through the other optics between the Wollaston prism. The second, and more influential contribution, is the phase difference between the beams traveling through the Wollaston prism. After the splitting of the beams at the structure interface in the prism, the beam is split into an ordinary ray (o-ray) and an extraordinary ray (e-ray). These rays have a different index of refraction, and thus a different speed in the second half of the prism, which leads to a phase difference between the two beams at its exit. The same phenomenon happens at the second Wollaston prism before the beams are made colinear at the structure interface in the prism.

With the source of the phase differences identified, multiple methods of adjusting the relative phase of the beams to bring them back to either 0 rad or π rad phase difference can be discussed. The first method is to adjust the Wollaston prism in a direction orthogonal to the optical axis of the system and parallel to the splitting plane. By adjusting the prism, the relative phase difference between the o-ray and the e-ray are changed, and by using a polarimeter (or by iteratively rotating a linear polarizer while adjusting the Wollaston prism), the Wollaston prism position for optimal phase delay can be found. This is the method used by Smeets, based on the statement in Section 1b of Ref. [7], where he mentions that the "*...optical path difference...consists of a constant value (given by the Wollaston prism positions).*" This method requires no additional optics, but is extremely sensitive to small movements of the prism. For example, if the prism is mounted in a typical optical post mounting system, the action of tightening the set screw after adjustment can shift the phase through one, if not many, full rotations. If using this method, it is suggested to use a precise linear translation stage to adjust the position, and thus phase delay of the two beams. This is likely the most common method of phase adjustment seen in the literature, and while most papers do not explicitly mention that this is how the phase is being adjusted, there are some that do [31–39]. Note also that if a Sanderson prism is used for the splitting prism that this also needs to be shifted for phase adjustment [40]. The second method of phase shifting is to use a Berek compensator, which is a variable retarder that can adjust the relative phase of the two beams by rotating the compensator with high precision [24–28, 41, 42]. A similar optic that can accomplish this task is a Soleil-Babinet compensator [43]. The last option for adjusting the phase of the two beams is to use a quarter-wave plate [28, 44–54]. By rotating the quarter-wave plate, the relative phase of the two beams can be shifted and brought back to an equivalent linear polarization. The rotation provides precise control over the phase shift, and while the cost is less expensive than the Berek compensator, it still requires an additional optic in comparison to the Wollaston shifting method.

Analyzer for Beam Interference

Just before the signal is incident on a photodiode (or camera, etc.), the polarization of the colinear orthogonal beams must be made to interfere with each other (see: Fresnel-Arago Laws). This is accomplished using an "analyzer", which in practice is typically a linear polarizer, a polarizing beamsplitter [24–29], or a polarizing prism [46, 49]. The majority of systems use a linear polarizer as the analyzer, and so these references are not included here. The benefit of using a polarizing beamsplitter or another polarizing prism is that complementary interference signals can be acquired on two detectors (or a balanced detector) to reduce the influence of laser noise, for example. Care must be taken to achieve the correct phase delay of the two beams before these optics. Retarders (such as half-wave plates and quarter-wave plates) cannot be used to make the beams interfere, since they only adjust the phase of the beams relative to each other depending on their orientation. The relative beam phase adjustments ensure that when the analyzer is rotated, the interference can be placed at the middle of the infinite fringe, maximizing sensitivity and maintaining linearity of the signal in response to a phase offset due to the flow disturbances.

Data Acquisition System

The photodiodes used in the system should be sufficiently sensitive at the laser's wavelength, typically measured as the responsivity in units of A/W. Silicon photodiodes are generally used since they are highly sensitive in the visible

wavelength range, have high bandwidths, do not require cooling (like some infrared detectors), and are inexpensive (even for amplified detectors). Connecting the photodiodes to the oscilloscope for digitization is typically done using BNC or SMA cables, with the resistance of the cable matching that of the scope to avoid ringing. Using shielded cables can mitigate interference from electrical noise during testing. To maximize the bandwidth of the photodiode, the termination load resistance should be as low as possible while still providing sufficient signal-to-noise. A termination of 50Ω is typically the minimum and can be used without issues given the laser power is sufficient. If higher termination values are required to increase the signal, and the scope only has 50Ω or "High-Z" termination, then a variable resistance feed-through terminator can be used to adjust to an intermediate value. DC-coupling is typically used for digitization, since it doesn't attenuate the low frequency signal. However, it also shifts the signal up to a DC level that is dictated by the voltage at the middle of the infinite fringe, meaning the smaller AC level of the fluctuations will have lower vertical resolution on the scope (measured in V per division). Sometimes, both AC and DC coupled signals are acquired on separate channels to that the low frequency DC component can be measured on the DC-coupled channel, while the higher frequency AC signal can be measured on the AC-coupled channel with high vertical resolution. However, two acquisition channels are needed instead of one, which is simple for a few measurement points, but becomes prohibitive with many measurement points. The record length of the acquisition depends on a number of factors, including the facility where the measurements are taking place (laboratory, wind tunnel, etc.), the type of wind tunnel facility (impulse, blow-down, etc.), the duration of the flow of interest, the number of acquisition channels, the sampling rate, the amount of data storage, the desired frequency resolution, noise reduction, and more. Ideal settings for the experiment are typically identified on a case-by-case basis. Further description of the FLDI data analysis procedure after digitization in the oscilloscope is given in Section III.

C. FLDI with Cylindrical Lenses

Typical FLDI systems use spherical lenses for all of the focusing optics. However, as noted by Smeets in Section 3b of Ref. [7], by using cylindrical lenses instead of spherical lenses, the beam can be focused in only one direction and not the other, resulting in averaging in one coordinate direction while retaining the tight beam focusing nature of the FLDI system in the other. While not suitable for every application due to the reduced focusing in one of the directions, the cylindrical focusing FLDI system is ideally suited for measurement over wide flat geometries, where the spherical focusing beams would otherwise be clipped by the surface, as shown in Fig. 9. For a spherical lens setup, the upper portion of the beam which is not clipped on one side will be clipped on the other side due to inversion of the light across the focal point. The cylindrical FLDI allows the measurement points to be located directly adjacent to the model surface, whereas the spherical system points would need to be located at some finite distance above the surface.

Houpt and Leonov used the cylindrical FLDI system to make measurements in a supersonic flat plate boundary layer of the University of Notre Dame SBR-50 wind tunnel wall; the use of cylindrical lenses was required to avoid clipping of the beam across the entire width of the test section [55–57]. This system collected the light from the elliptic laser line onto a single photodiode, and so the resulting measurement was averaged over the entire line. In order to make multi-point measurements along a line in the boundary layer of a flat plate, Weisberger *et al.* used an FLDI system with cylindrical optics and a linear array photodiode [47, 50]. This increased the spatial resolution of the system in the ellipse major axis direction, discretizing the linear measurement region into 16 separate measurement channels. This system was also operated as a two-line system such that convective velocities and disturbance evolution could be measured (discussed further in Section IV.B). A modified cylindrical/spherical FLDI system was used by Hopkins *et al.* to make measurements on a flat plate, but because it was not required to make a measurement directly adjacent to the surface, the elliptic beam was focused to a single tight spot at the beam focus, slightly off the surface [34, 38]. However, due to the combination of the cylindrical and spherical lenses, this beam spot was closer to the surface than an equivalent spherical FLDI system would be, and was able to achieve a tighter focus in both directions than the typical cylindrical lens FLDI system. Note, however, that a typical cylindrical lens FLDI system still uses spherical field lenses, and it is the expanding lenses that are cylindrical. Cylindrical lenses were used in combination with a diffractive optical element FLDI system (discussed further in Section IV.C) to make a simultaneous multi-line measurement across the width of a flat plate model, with the signal from each line captured on its own photodiode through the use of a fiber optic collection unit (discussed further in Section IV.G) [58] and also using a high-speed camera [59, 60].

The design of a cylindrical lens FLDI system will typically depend on the method of acquisition of the data, that is, whether the system will be operated as a single-point measurement or as a multi-point measurement. For single-point measurements, the method of acquisition is shown in Case A of Fig. 10, where the entire beam ellipse is incident on the single photodiode element. As mentioned previously, this method averages the signal over the entire beam, a

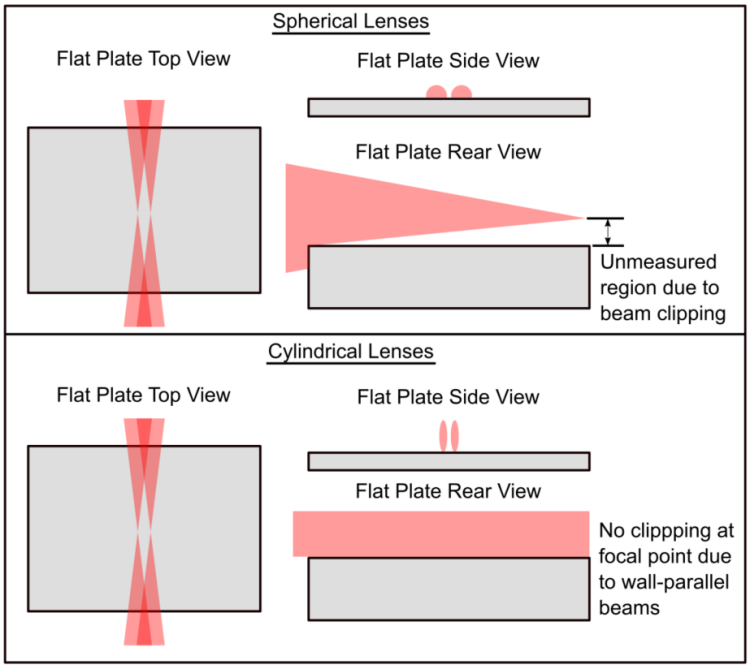

Fig. 9 Spherically focused FLDI beams are clipped on the edge of flat plate style geometries, which prevents near wall measurements. However, an FLDI setup that utilizes cylindrical lenses to focus only in one direction can probe closer to the surface in such scenarios.

significant increase over the spherical FLDI system at the beam focus. For example, the waist diameter of a spherical FLDI system at the beam focus can be on the order of a few microns. For the cylindrical FLDI system, the beam waist in the minor axis of the ellipse remains on the order of a few microns, but the major axis may be on the order of a few millimeters. This can make the cylindrical FLDI system less sensitive to smaller-scale fluctuations than its spherical FLDI counterpart. One method of decreasing the major axis probing region is to magnify the beam on the detector, such that the region of the beam measured by the detector is smaller than the entire beam major axis, as shown in Case B of Fig. 10. However, if only a single measurement point is desired, it is preferred to keep the major axis of the ellipse as small as possible across the test section.

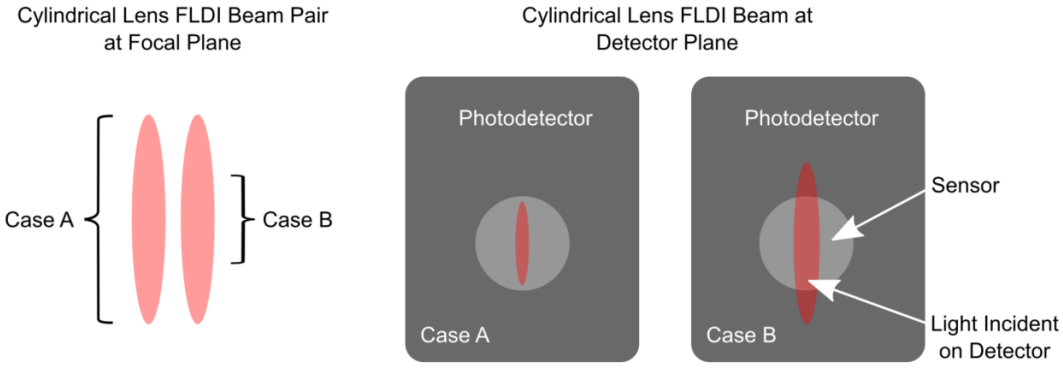

Fig. 10 A cylindrical lens FLDI setup with all light focused on detector, Case A, will have contributions from the entire beam, resulting in a spatial averaging along the major axis of the beam at the focal plane. If only a portion of the beam is used, Case B, the spatial averaging is limited.

When making a multi-point measurement using a cylindrical lens FLDI system, the choice of line size/length is different than a single-point measurement. In this case, a linear array photodiode is typically used, where the beam is

placed on the photodiode such that the major axis of the beam is measured by N photodiode elements in the linear array photodiode. Here, the spatial resolution of the measurement along the major axis of the beam is dictated by the length of the major axis at the beam focus, the magnification of the line on the linear array photodiode, and the size of each individual photodiode element in the array. The length of the major axis of the beam at the beam focus is typically adjusted using a pair of cylindrical lenses, one with a negative focal length and one with a positive focal length. There is then a balance required between probing a larger region of the flowfield (length of the beam major axis), while also probing smaller regions of the flow for each photodiode element of the array to maintain small-scale fluctuation sensitivity (magnification of beam, number and size of elements in photodiode array). Because the laser power is spread over multiple channels, the intensity of light measured by each element in the array will be lower than that measured by a single photodiode, and so this method generally requires a higher power laser to achieve a sufficient signal-to-noise ratio. Also note that because the beam ellipse retains a Gaussian profile along the major axis, the intensity will be higher at the center than at the edges, although this can be adjusted by using apodizing filters if it is necessary to achieve uniform illumination over all the channels. The final consideration for a multi-point measurement is that a spatial calibration is required to map the size/position of the linear array photodiode to the physical measurement location. This is generally accomplished using a precise knife-edge traversal through the beam focus while measuring the signal on the linear array, but other options exist, such as the method outlined in Camillo *et al.* [40].

D. Polarizing Prisms

The majority of papers describing FLDI systems use Wollaston prisms as the birefringent polarizing prism to split the laser beam into orthogonally polarized beams, dating back to its first implementation in Smeets' original papers. This prism is ideally suited for the task, as it takes an incoming beam orthogonal to the entrance face of the prism (along the optical axis of the system), and splits the beam into two orthogonally polarized beams, each diverging from the optical axis at half the total divergence angle of the prism. This divergence angle is a function of the laser wavelength, the material of the Wollaston prism, and the angle of the interface between the two prism halves of different optic axis orientation. A commonly-used splitting angle for the Wollaston prism is 2 arcmin, beginning with the paper by Parziale *et al.* [18]. This splitting angle provides a good balance between minimizing the spatial separation of the two focused beams while also providing enough separation to achieve high sensitivity to the fluctuations. While 2 arcmin seems to be the most ubiquitous splitting angle, other splitting angles have also been used, such as 0.5 arcmin [61], 1 arcmin [36, 62–64], 1.5 arcmin [58–60, 65–71], 4 arcmin [41, 42, 72–78], 5 arcmin [33, 79–87], 8 arcmin [35, 88, 89], 10 arcmin [53, 54], and more.

A downside of the Wollaston prism is that the splitting angle is fixed, and so if another angle is required, two more matching Wollaston prisms must be purchased, which can be expensive because most prisms are 2 inch (50.8 mm) square optics. An adjustable beam splitting optic was demonstrated by Sanderson in Ref. [90], whereby applying different levels of pressure to a four-point loading mechanism on a transparent piece of acrylic allowed for adjustment of the beam splitting angle. These prisms, typically called *Sanderson prisms*, work by the photoelastic, or piezooptic, effect, which occurs in transparent polymers. This prism is an attractive option for setups that require adjustment of the beam splitting angle to change the beam separation distance at the beam focus, and many subsequent systems have used them for this purpose. As with every option, this prism has some associated downsides. A high-precision adjustable loading mechanism is required to finely adjust the splitting angle, and two of these must be made, one for the pitch side and one for the catch side. The loading required to stress the acrylic for the larger clear apertures required for larger beam diameters (better off-focus rejection of signal) can be excessive, and the uniform splitting of the entire beam diameter at the prism may not be guaranteed. Finally, calibration is required to associate an applied force from the loading mechanism with a splitting angle, and this must be performed for both prisms such that they can be set to exactly the same value necessary for the colinearity of the recombined beams on the catch side. While not as common as the Wollaston prism, the Sanderson prism continues to be used as an adjustable beam splitting optic in FLDI systems [24, 25, 27, 40, 55–57, 75, 91–93].

While both the Wollaston and Sanderson prisms take as input a single input beam of appropriate polarization, and split this beam into two orthogonally polarized beams with certain angular deviation, another option exists for the splitting of the beams in an FLDI system. Marsh *et al.* use a combination of a polarizing beamsplitter, two mirrors, and a non-polarizing beamsplitter in a Mach-Zehnder configuration [94]. While this method is more complicated and time-consuming to set up initially, it can provide fine control of the beam splitting angle and beam phase. It also only requires optics that are able to be purchased off-the-shelf. Further details of this setup can be found in Section IV.D.

III. FLDI Theory and System Analysis

This section discusses the basic theory of FLDI operation, that is, that laser beams of variable diameter interrogate the medium of interest (typically gas) in a differential manner. Index of refraction gradients along the beam separation axis (e.g., x-axis in Fig. 2 $\partial n/\partial x$) create an optical path difference and thus a phase difference ($\Delta\phi$) between the beams. The orthogonally-polarized beams are made to interfere at a polarizer and then measured by a photodiode (PD), where the changing phase differences between the two beams cause fluctuations in the intensity of the light. The incident light on the PD generates an electrical current and is finally converted to voltage, V, and then digitized by an oscilloscope. On the relationship between FLDI signals and flow properties, Smeets [6] wrote "From the [voltage] signals received, primarily qualitative information could be achieved, e.g., on the frequency spectra of the turbulent fluctuations near the focal point. The deduction of quantitative data on the level of local density fluctuations is only possible by means of assumptions and approximations. The accuracy of the results is, therefore, only moderate (for further details, see [95])." Smeet's self-reference, [95], has not yet been publicly translated to English. Despite Smeet's warning, considerable effort has been made in roughly the past decade towards improving our understanding and interpretation of the FLDI signal. This section summarizes these efforts, with further details included in Section VI.

A. Relation Between Voltage and Phase Difference

The relation between voltage and phase difference was first described by Smeets and George [7] (Section 1.b) and is discussed by many others [18, 24, 96, 97]. The intensity of light (I_{PD}) incident on the photodiode is a function of the phase difference as follows:

$$I_{\mathrm{PD}} = 2I_{\mathrm{b}}[1 + \cos(\Delta\phi)] \tag{4}$$

where (I_{b}) is the intensity of a single beam. In practice, perfect interference contrast is unlikely, resulting in a constant intensity, I_{min}, superimposed on the phase-dependent intensity. It is also helpful to introduce a constant phase shift, $\Delta\phi_0$, which accounts for phase delays caused by optical components such as the prisms or phase-compensators. Equation 4 is now re-written as:

$$I_{\mathrm{PD}} = 2I_{\mathrm{b}}[1 + \cos(\Delta\phi + \Delta\phi_0)] + I_{\mathrm{min}} \tag{5}$$

In order to maximize sensitivity and avoid phase ambiguity, it is best practice to adjust $\Delta\phi_0$ (e.g., by translating one Wollaston prism along the beam separation axis or using a retarder) such that the signal is placed at the linear portion the interference fringe. The cosine term can then be changed to a sine term and Eq. 5 rewritten as:

$$I_{\mathrm{PD}} = \frac{1}{2}\left[I_{\mathrm{max}} + I_{\mathrm{min}} + (I_{\mathrm{max}} - I_{\mathrm{min}})\sin(\Delta\phi)\right] \tag{6}$$

where $I_{\mathrm{max}} = 4I_{\mathrm{b}} + I_{\mathrm{min}}$. The light is converted to current by the PD and then voltage by the PD's circuit such that the measured voltage can be expressed as:

$$V = \frac{1}{2}\left[V_{\mathrm{max}} + V_{\mathrm{min}} + (V_{\mathrm{max}} - V_{\mathrm{min}})\sin(\Delta\phi)\right] * H_{\mathrm{PD}} \tag{7}$$

where H_{PD} is a transfer function which accounts for signal attenuation caused by the response time of the PD. H_{PD} is affected by PD size, amplifier gain, terminating resistance, and more. Beam size and incident power on the photodiode have also been shown to have a significant impact on the PD's spectral response [44]. Increasing any of these parameters will decrease the cut-off frequency at which H_{PD} rolls-off from unity, reducing the bandwidth of the measurement. This represents a trade-off, because large PDs aid alignment and robustness to vibrations, and increasing gain and terminating resistance can improve signal to noise. These effects, which were investigated by Fulghum [24] but have received little attention since, are a good subject for future investigations especially when bandwidths > 1 MHz are desired.

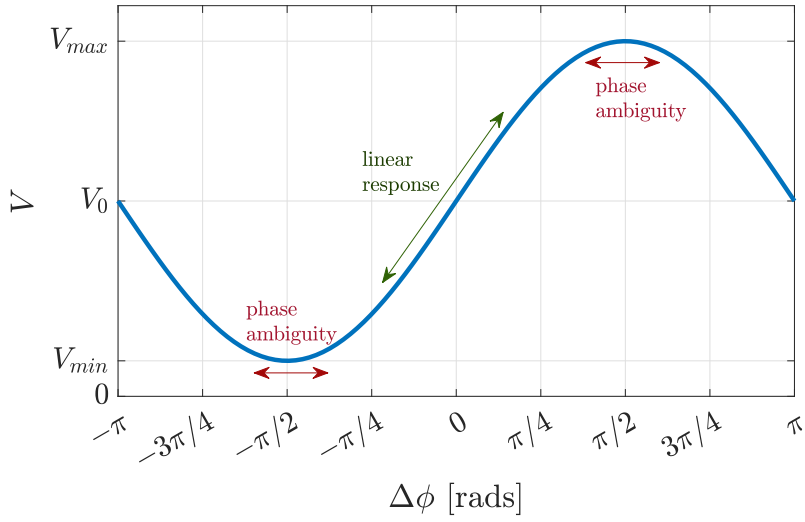

Fig. 11 Relationship between voltage and phase difference for a simple LDI or FLDI instrument.

Equation 7 is plotted in Fig. 11 (ignoring the effects of H_{PD}), which illustrates the voltage at the middle of a fringe, $V_0 = (V_{\text{max}} + V_{\text{min}})/2$. This sinusoidal relationship should be well characterized prior to each run by translating one Wollaston prism along the beam separation axis (or by rotation of a retarder) and taking several voltage measurements. A high quality interferometer will produce a large ratio of maximum to minimum voltages, say $V_{\text{max}}/V_{\text{min}} > 20$. If this is achieved, the voltage-phase relationship can be approximated as:

$$V = V_0 + V_0 \sin(\Delta\phi) * H_{\text{PD}} \tag{8}$$

Because the voltage is typically converted to phase difference in the analysis, Eq. 8 be rearranged:

$$\Delta\phi = \frac{\sin^{-1}\left(\frac{V}{V_0} - 1\right)}{H_{\text{PD}}} \tag{9}$$

Finally, if the PD's response is measured or assumed to be unity over the bandwidth of interest and if the fluctuations of interest are small enough, say $\text{RMS}(V) < V_0/4$, then Eq. 9 can be approximated as:

$$\Delta\phi \approx \frac{V}{V_0} - 1 \tag{10}$$

B. Relation Between Phase Difference and Refractive Index

The most widely used fundamental equation relating phase difference to refractive index is described below: For two beams traversing paths s_1 and s_2 respectively, the phase difference at the detector face ($s = D$) associated with the refractive index field $n(\mathbf{x})$ is given by

$$\Delta\phi(t) = \frac{2\pi}{\lambda_0} \iint_D I_0 \left[\int_S^D n(\mathbf{x}_1, t) ds_1 - \int_S^D n(\mathbf{x}_2, t) ds_2 \right] d\xi d\eta \tag{11}$$

where λ_0 is the laser wavelength, S is the location of the light source, $\mathbf{x}_i(s_i) = (x_i, y_i, z_i)$, and $I_0(\xi, \eta)$ is the intensity on the detector face when there is no phase difference between the two beams. ξ and η are coordinates which map the detector surface. Equation 11 describes a general interferometer via ray tracing and is taken from Schmidt and Shepherd [96] (in a form published by Lawson [97]), who derived it from Section 7.2 of Born and Wolf [98]. Alternative approaches to modeling this relationship are presented by Smeets [95], Fulghum [24], and Hameed and Parziale [99], though all approaches use an equation with similar form to Eq. 11. A common simplification includes modeling the beam intensity distribution with a Gaussian function and polar coordinates such that

$$I_0(r,\theta) = \frac{2}{\pi w^2}\exp\left(-\frac{2r^2}{w^2}\right) \tag{12}$$

where w is the Gaussian beam radius parameter [100]. A second common simplification is that the paths of complimentary, parallel rays in the interferometer can be parameterized by the z-axis and written as

$$\mathbf{x}_1(z) = \left(x + \frac{\Delta x_1}{2}, y, z\right) \tag{13}$$

$$\mathbf{x}_2(z) = \left(x - \frac{\Delta x_1}{2}, y, z\right) \tag{14}$$

Thus, the path integrals can be re-written as integrals along the z-axis.

Equation 11 can be solved for the exact phase change provided a complete, well-resolved solution for $n(\mathbf{x}, t)$ is available; this is the subject of computational FLDI, discussed in Section VI. However, there is no way to solve Eq. 11 in the other direction, that is, for $n(\mathbf{x}, t)$ from $\Delta\phi(t)$. This is because infinitely many refractive index fields can result in the same measured phase difference (non-uniqueness). Thus, mathematical models using simplifying assumptions of the flow field are used to invert Eq. 11. A comprehensive two-part review of this process was recently published by Lawson and Austin [101, 102], and readers are encouraged to refer to these and other works by Lawson for a more comprehensive review of FLDI theory.

Typically, an equation of the following form is desired:

$$\Delta\phi(t) = n(t) * H \tag{15}$$

where $n(t)$ is the 'local' refractive index at the instrument's focus, and H is a transfer function with units of radians which describes the ways in which the refractive index field is processed and modulated by the instrument to produce the measured signal. If the fluid is homogeneous, refractive index can be easily converted to density using the Gladstone-Dale relation [103]. H is derived from both the instrument model (Eqs. 11 through 14) and the flow field model. The most common flow-field model contains a superposition of sinusoidal waves [102], which has been used to approximate acoustic waves [104, 105], instability waves [96], and turbulent flows [24, 75, 99, 106, 107]. Modeling of shock waves and blast waves has also been demonstrated [48, 93, 108]. Most of the references above contain derivations of transfer functions, where each function differs based on FLDI application, flow model, and chosen physical quantity of interest. However, two terms are common in nearly all works: the transfer functions due to beam separation,

$$H_{\Delta x} = \sin\left(\frac{k_x \Delta x}{2}\right) \tag{16}$$

and due to beam radius,

$$H_w = \exp\left(-\frac{k_x^2 w^2}{8}\right) \tag{17}$$

where k_x is the wavenumber component aligned with x-axis and w is the local beam radius parameter. For Gaussian beams, the radius varies along the optical (z) axis according to

$$w(z)^2 = w_0^2\left[1 + \left(\frac{\lambda_0 z}{\pi w_0^2}\right)^2\right] \tag{18}$$

where w_0 is the beam radius at the focus ($z = 0$) [100]. A smaller value of w_0, which is proportional to the f-number of the system, means the radial divergence angle of the beams,

$$\theta_d = \frac{\lambda_0}{\pi w_0} \tag{19}$$

is larger and the depth of focus is shorter. The divergence angle is easier to measure than w_0 (e.g., see Section 3.5 of [75]), and it is more directly related to the spatial filtering along the optical axis [109]. Combining Eqs. 16 through 19 yields the following expression:

$$H_z = \sin\left(\frac{k_x \Delta x}{2}\right) \exp\left(-\frac{\theta_d^2 k_x^2 z^2}{8}\right) \exp\left(-\frac{k_x^2 w_0^2}{8}\right) \tag{20}$$

The FLDI signal is proportional to the integral of refractive index fluctuations, n', multiplied by H_z such that

$$\Delta\phi \propto \int n'(z) H_z dz \tag{21}$$

Typically the beam radius at the focus is significantly smaller than the scales of interest (i.e., $w_0 k_x << 1$), and the final term in Eq. 20 can be ignored. Thus, the FLDI's sensitivity is essentially described by two parameters:

1) Δx: the beam's separation
2) θ_d: the beam's divergence angle

The effects of these parameters on the measured signal are reviewed by Smeets and George [7], Fulghum [24], Ceruzzi and Cadou [75], Schmidt and Shepherd [96], Lawson [97], Benitez *et al.* [109], and others referenced in this section. Key conclusions are summarized below:

- The FLDI sensitivity is maximized for disturbances at the focus and with a wavelength of twice the beam separation (a wavenumber of $k_x = \pi/\Delta x$). Sensitivity uniformly falls off for disturbances both smaller and larger than $k_x = \pi/\Delta x$, similar to a bandpass filtering effect. This explains the LDI/FLDI systems' insensitivity to large wavelength mechanical/structural/facility vibrations.
- Sensitivity falls off as $|z|$ increases. The rate of roll-off increases with wavenumber and divergence angle.
- Spatial filtering away from the instrument's focus is achieved through a combination of these effects. Small disturbances are averaged by the large beam diameters while large disturbances are uniformly filtered because they produce weaker gradients than small disturbances for a fixed amplitude. The combined effects could be referred to as "common mode" rejection.

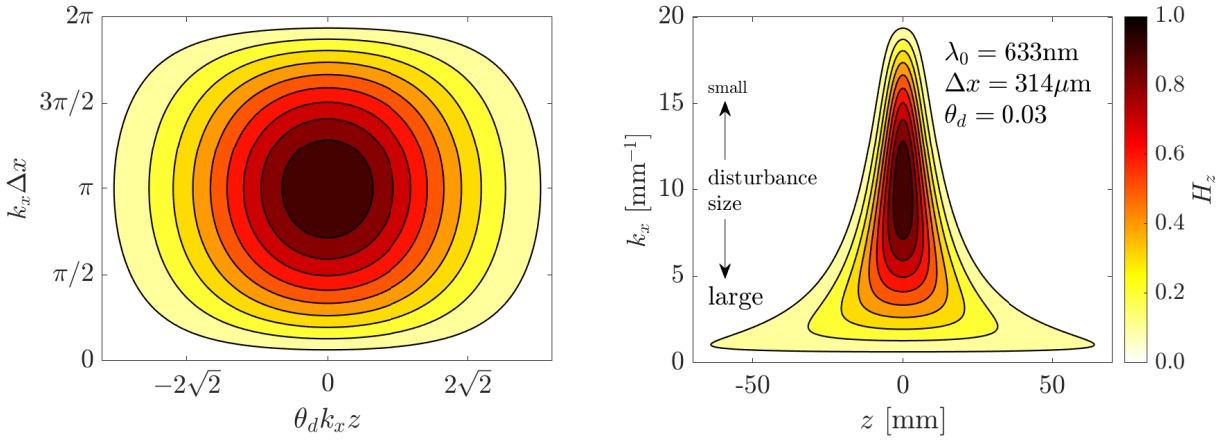

(a) Non-dimensional response, valid for $w_0 k_x < 1$. **(b) Dimensional response for a typical FLDI set-up**

Fig. 12 FLDI sensitivity to flow-parallel sinusoidal waves.

The magnitude of the combined overall transfer function, $|H_z|$ is plotted in Fig. 12 versus both wavenumber and optical axis to illustrate the way in which an FLDI spatially filters flow-parallel, uncorrelated sinusoidal disturbances to produce the measured signal. Equation 20 is a simplified expression for FLDI sensitivity, and more complicated effects arise when accounting for the following:

- Disturbances with arbitrary wavefront orientations (Hameed and Parziale [99], Lawson and Austin [101])
- Disturbance amplitude (Fulghum [24], Hameed and Parziale [99]) and velocity variation along the optical axis (Ceruzzi and Cadou [75], Ceruzzi [110])

- Coherent wavefronts and the effects of wavefront phase along the optical axis, which has not yet been addressed by transfer functions, but has in computational FLDI [106, 111, 112]

These effects require assumptions about the nature of the interrogated flow field and may lead to improved accuracy at the cost of complexity and computational time. At present, for most applications in high speed wind tunnels, the large uncertainties in the flow field lead to prohibitively large uncertainties in the quantitative interpretation of FLDI signals. Thus, Smeet's warning still rings true.

C. Spatial Resolution

The measurement volume of the FLDI instrument can be defined with dimensions X_{SR}, Y_{SR}, and Z_{SR}, which describe the instrument's spatial resolution along the x, y, and z axis, respectively. At the focus, $X_{SR} = \Delta x$ (the beam separation), and $Y_{SR} = 2w_0$, (the beam diameter). Further away from the focus both X_{SR} and Y_{SR} are approximately equal to the local beam diameter which can be modeled with Eq. 18 and is easily measured with a beam profiler camera. The optical axis spatial resolution Z_{SR}, also called the depth of focus, is more difficult to describe. Approaches for estimating, modeling, and conceptualizing Z_{SR} are reviewed in this subsection.

Smeets and George did not attempt to quantify the FLDI depth of focus in the reports which are translated into English (although the untranslated reports may provide more insight into their thoughts on the matter [4, 95]). Parziale [19] proposed a simple empirical method for determining Z_{SR}, by translating a small jet along the optical axis and measuring the response. Figure 3 shows a diagram of the experiment and the results. The distance from the focus at which the root-mean-squared (RMS) of the signal fell to $1/e$ of its peak, $z_{1/e}$, was taken to be the half-width of the "integration length":

$$Z_{SR} = 2z_{1/e} \tag{22}$$

This approach works well if the flow field of interest is composed of similar structures and scales to those in the region of the jet which was interrogated by the FLDI. However, the measured length does not represent a universal spatial resolution for the instrument because the sensitivity is a function of the disturbance scale, as illustrated by Eq. 20. Recent experimental [74, 75, 104, 110] and computational [109] investigations have shed more light on the optical axis sensitivity.

Figure 14, which contains data from Ceruzzi *et al.* [74], illustrates how the optical axis decay of the signal RMS can vary with disturbance scale. Figure 14a shows signal decay for a jet at two streamwise positions, $x/d = 5$ and 45, based on the experimental set-up shown schematically in Fig. 13. When the FLDI (with radial divergence angle $\theta_d = 0.029$) is near the jet's nozzle ($x/d = 5$), the response decays rapidly with z, reaches zero approximately 150 mm from the focus, and the $1/e$ length is roughly 37 mm. In contrast, when the jet is further away ($x/d = 45$) the decay is slower, does not reach zero by 200 mm, and the $1/e$ length is roughly doubled. The differences arise because the region of the jet which is interrogated by the FLDI is wider and contains larger scales as x/d increases. Figure 14b shows results from a similar experiment, using an FLDI setup with a smaller divergence angle ($\theta_d = 0.014$), which reduces the influence of flow width. The jet is replaced by a 64 mm square test section with Mach 3 air flow. The orange triangles represent measurements of the 'empty' tunnel, and the RMS signal is primarily produced by sidewall turbulent boundary layers which are 10 mm thick [72]. The purple stars, which represent measurements downstream of a "disturbance generator" (19 mm tall ramp), decay slower, are far from zero at $z = 400$ mm and result in a 56% longer $1/e$ value compared to the measurements of the empty tunnel. The primary reason is the larger, more coherent disturbances in the flow downstream of the ramp. Figure 14 also illustrates the large variation in $1/e$ length with divergence angle, from as small as 37 mm for $\theta_d = 0.029$ to as large as 237 mm for $\theta_d = 0.014$.

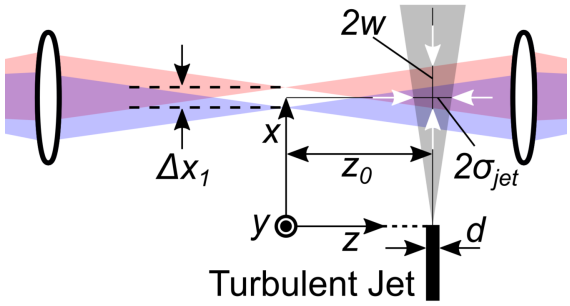

Fig. 13 Schematic of turbulent jet experiment to investigate optical axis sensitivity.

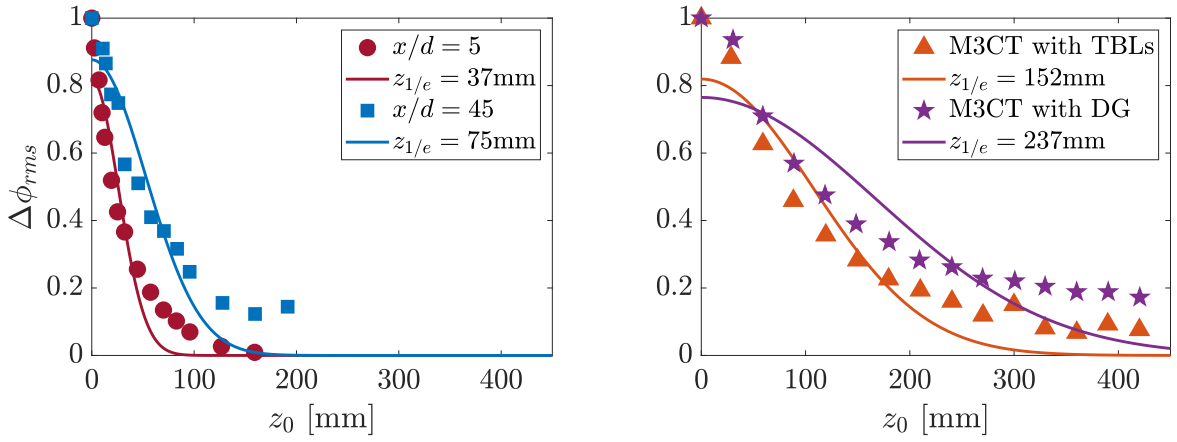

(a) Response to 3 mm diameter turbulent jet, $\theta_d = 0.029$ **(b) Response to 64 mm square test section of M3CT, $\theta_d = 0.014$**

Fig. 14 FLDI RMS signal response along the optical axis, adapted from Ceruzzi *et al.* [74]. M3CT: Mach 3 calibration tunnel, TBLs: turbulent boundary layers, DG: disturbance generator.

The transfer function, Eq. 17, is a more versatile method for modeling the sensitivity, and thus spatial resolution, along the z-axis because it accounts for the effects of disturbance scale and divergence angle. Lawson *et al.* validated this approach (see Section 4.2 in Ref. [104]), showing that the response to acoustic waves of varying frequency, and thus varying wavenumber, collapses under the transform of Eq. 17. More recently, Ceruzzi and Cadou [75], Ceruzzi [110] showed that the broadband spectra of a turbulent jet collapsed under the transform of Eq. 17 provided the jet's disturbance and velocity profile are modeled accurately. These experiments suggest that the spatial resolution can be estimated directly by setting $H_w(Z_{\mathrm{SR}}/2) = 1/e$ and solving for Z_{SR}. For flow-parallel uncorrelated sinusoidal waves the resulting equation is

$$Z_{\mathrm{SR}} = \frac{2\sqrt{2}\lambda_x}{\pi\theta_d} \tag{23}$$

where λ_x, the disturbance wavelength in the x-direction, is related to the wavenumber by

$$\lambda_x = \frac{2\pi}{k_x} \tag{24}$$

Figure 15 shows how the spatial resolution increases linearly with disturbance wavelength and divergence angle. The divergence angle is not reported in most literature to-date, however it can be computed from w_0, which is occasionally reported, using Eq. 19. Most FLDI set-ups have divergence angles between 0.015 [74] and 0.040 [113]. The upper limit is constrained by the lack of availability and prohibitive cost of high-quality prisms and low-f-number lenses with apertures > 100 mm. For disturbances smaller than 2 mm, a spatial resolution smaller than 50 mm is achievable, provided the FLDI beams have a sufficiently large divergence angle. For disturbances larger than 5 mm, the spatial

resolution will likely exceed 100 mm. Experimenters can use Eq. 23 or Fig. 15 as a guide for determining whether their set-up will be able to adequately resolve the scales of interest.

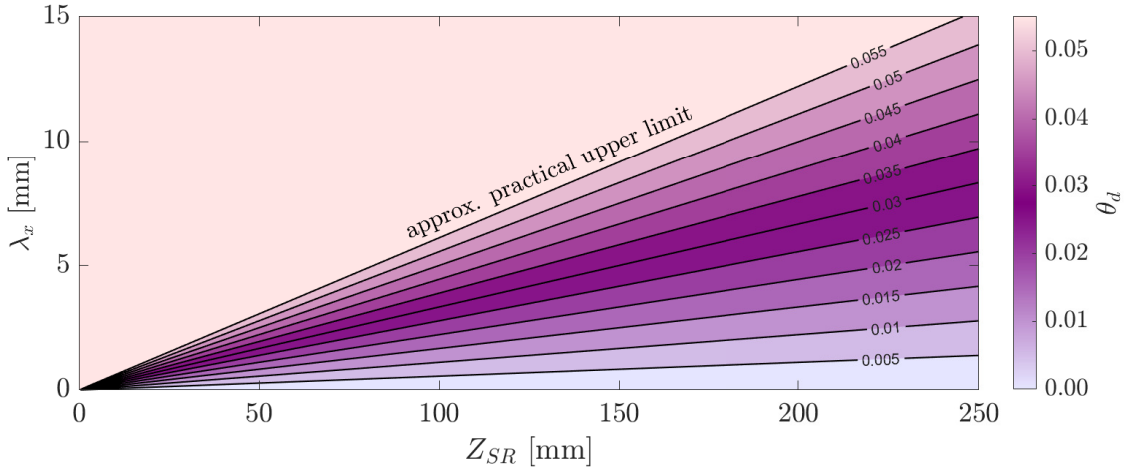

Fig. 15 Relationship between spatial resolution (Z_{SR}), wavelength (λ_x), and divergence angle (θ_d) for uncorrelated, flow-parallel disturbances.

One limitation of Eq. 23 is it does not account for situations where disturbances far from the focus have significantly larger amplitudes than those at the focus. The most prevalent example of this situation is the measurement of freestream disturbances in wind tunnels where sidewall shear and boundary layers are typically > 10 times stronger than the disturbances of interest. In this situation, the FLDI signal will be significantly corrupted by large scales away from the focus. This effect was discussed and modeled by Fulghum [24] (see Section 3.10.2), and validated experimentally by Birch *et al.* (see Fig. 8 in [27]). Modern discussions and modeling of these effects are provided by Gillespie et al. [35], Ceruzzi [110], and Benitez *et al.* [106]. The key takeaway is that FLDI can only accurately resolve the amplitude of small scale, high frequency disturbances in the freestream (unless the shear / boundary layers are shrouded as in Birch *et al.* [27]). A method for determining the cut-off frequency between resolved and unresolved signal is presented in Section 2.3.1 of [110]. For freestream disturbances in hypersonic wind tunnels, a conservative estimate for this cut-off is 200 kHz [27, 35, 106, 110], however, comparison with Pitot spectra from Lawson *et al.* [105] suggests the cut-off could be as low as 10 kHz in some cases.

Another limitation of Eq. 23 is that it does not account for the relationship between disturbance phases along the optical axis. If we assume that disturbances near the focus are correlated and in-phase with one another while disturbances up-beam of the focus are uncorrelated with those down-beam of the focus, it is reasonable to expect the signal to noise and the effective spatial resolution will improve. Computational studies are shedding more light on this phenomena [112]. Thus, Eq. 23 may be thought of as a conservative estimate of optical axis spatial resolution.

D. Experimental Validation of Theory

Schmidt and Shepherd performed a simple static experiment to validate the theory for quantifying the response of an FLDI to optical index gradients [96]. A rectangular argon jet with an aspect ratio of 16.5 was constructed and simulated using OpenFOAM. A schlieren image taken along the long axis of the jet is shown in Fig. 16a. The flow rate of the argon was low enough that the jet was steady and laminar, and reversed direction due to gravity at a certain height above the exit plane. The jet was approximately two-dimensional along the majority of the axis. The FLDI beams were aligned with a vertical offset (in the x-direction) along the interface between the argon and the ambient air as shown in the figure, with the focus of the FLDI positioned at the center of the jet. A pseudo-schlieren image shown in Fig. 16b demonstrates qualitative agreement with the experiment, and the index of refraction was computed numerically from the simulation.

Portions of the jet were covered with tape to produce different lengths over which the FLDI would integrate, and these lengths were not necessarily centered with respect to the position of the FLDI focus. The response of the FLDI was measured in the experiment and compared to simulations using the CFD data and a ray tracing model. The results

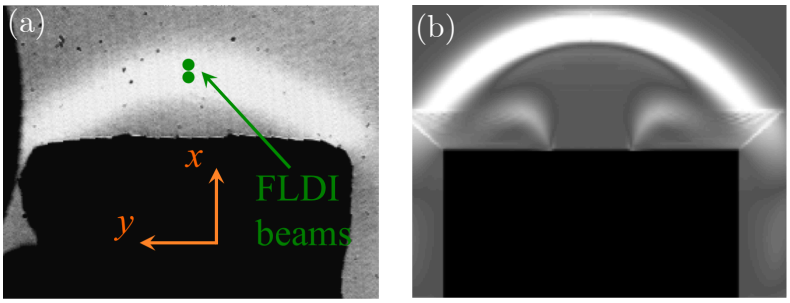

Fig. 16 (a) Schlieren image of the argon jet in the $x-y$ plane. The top of the jet is about 15 mm from the chamber exit and is observed to be uniform across the jet cross-section, temporally stable, and laminar. (b) Pseudo-schlieren image of the argon jet showing the vertical gradient in density for comparison with the experiment. Reproduced from [96].

are shown in Fig. 17, and demonstrate good agreement compared with the ideal line. These experiments demonstrated the validity of Eq. 11 for modeling the response to a static (or steady) flow.

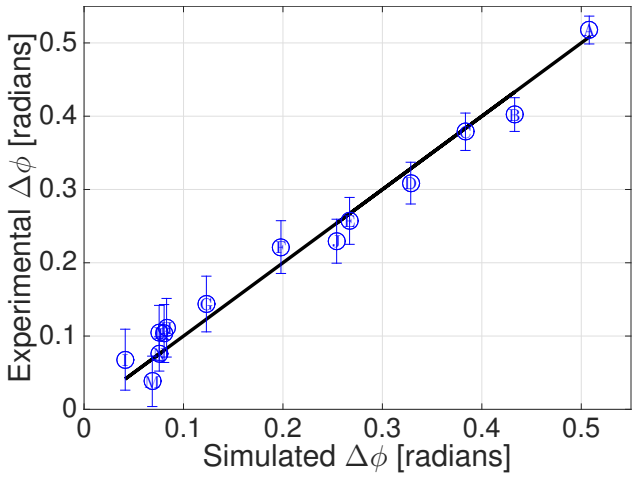

Fig. 17 Experimental versus numerical data for the argon jet experiments performed by Schmidt and Shepherd [96]. Letters on the markers refer to specific configurations detailed in Table 2 of [96].

Fulghum [24] used a turbulent jet to measure fluctuation spectra with hot-wire anemometry and FLDI. To accurately determine the spectral content of the jet, he estimated a transfer function for both techniques to compensate for any diagnostic-based amplitude dampening. The transfer functions were computed by analyzing the signal response to a square-wave input. By plotting the power spectral densities obtained by deconvolving the turbulent jet signal from the diagnostic transfer function, Fulghum found that both the hot wire and FLDI spectra had roll-offs near the expected $-5/3$ slope. These experiments demonstrated the utility of transfer functions for recovering accurate spectral slopes.

Lawson *et al.* [104] used a steady, laminar jet and an unsteady ultrasonic acoustic beam to characterize the static and dynamic response of an FLDI. For the steady jet, agreement between modeling, FLDI measurement, and an independent Mach-Zehnder interferometer further validated the approach of Schmidt and Shepherd [96]. For the unsteady acoustic beam, emphasis was placed on the FLDI's optical (z) axis response. Figure 18 shows the results where measured amplitudes collapse under the transform described by Eq. 17. This provided experimental evidence that transfer functions could accurately model the instrument's spatial resolution.

Lawson and Austin [108] also used an expansion tunnel start-up shock to demonstrate good agreement between measurements and simulations using a combination of unsteady CFD combined with the full ray-tracing approach (Eq. 11). These results, discussed further in Section VI, provide some validation for the ray tracing approach of Schmidt and Shepherd [96] for complex, dynamic flows where analytical transfer functions are not practical.

Ceruzzi *et al.* [74, 75, 110] used a round turbulent jet to investigate the response to a complex turbulent flow. They

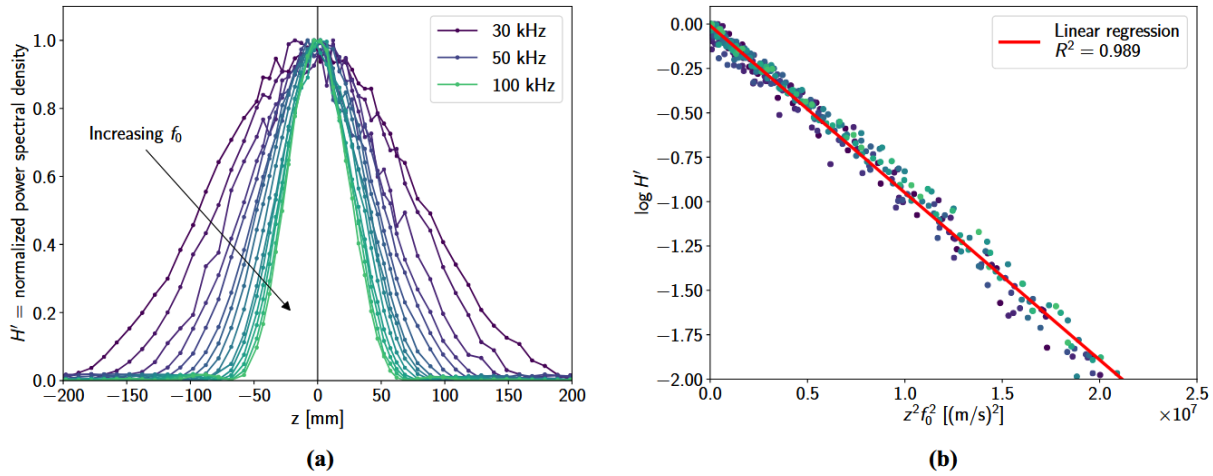

Fig. 18 Results of the ultrasonic beam experiments from Lawson *et al.* [104]. (a) Drop-off in FLDI response moving away from the location of the foci at z = 0. (b) Same data as (a), but plotted using the variables suggested by the analytical transfer function model. Frequencies f_0 range from 30–100 kHz in 5 kHz increments.

varied both the beam separation, Δx, and the position of the jet along the optical axis, z_0 (see Fig. 13). The results, re-plotted in Fig. 19, demonstrate that the measured spectra collapse under the transform of Eq. 20 combined with an accurate model of the jet's density and velocity profile. The collapse validates the simple transfer functions as useful for understanding the instrument in complex turbulent flows. The inclusion of the jet's density profile was proposed by Fulghum [24] and was also used by Hameed and Parziale [99], who demonstrated the benefit of this approach over an approach which assumes a uniform profile. The benefit of modeling the jet's velocity profile is demonstrated in Section 3 of [110].

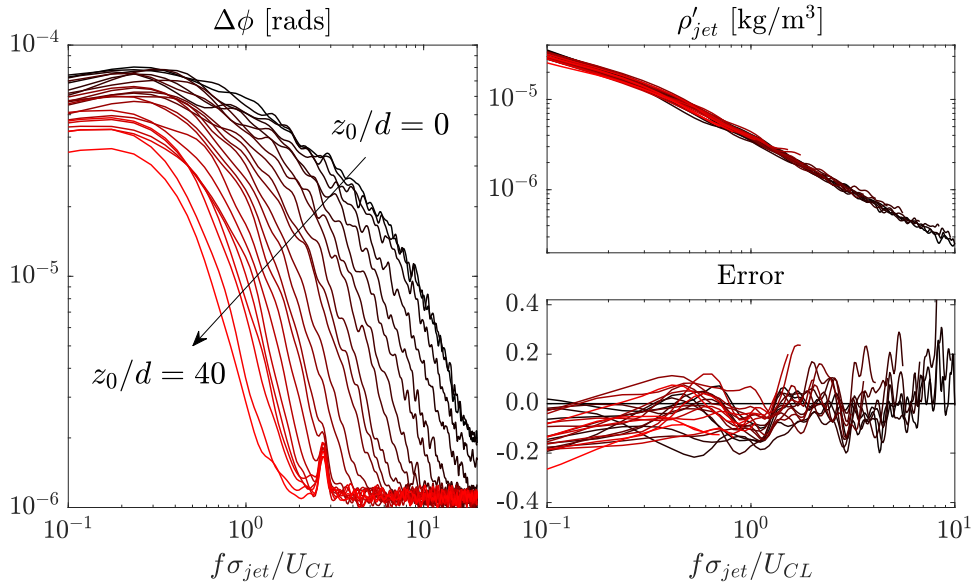

Fig. 19 Optical axis spectral response to a turbulent jet, d = 3 mm, x/d = 25. ρ'_{jet} is obtained by dividing $\Delta\phi$ by the transfer function described by Eqs. 20 and 21. Data re-plotted from Ceruzzi and Cadou [75].

Recently, Lawson *et al.* [105] has demonstrated agreement between Pitot probe and FLDI measurements, re-plotted in Fig. 20, when the spectra are transformed by the proper transfer functions. These experiments demonstrate the ability to recover spectra which agree in both magnitude and slope with an established measurement technique, representing a

major step forward in our ability to obtain accurate, quantitative measurements from FLDI. However, the authors caution that the bandwidths of the two techniques do not overlap and thus the agreement is not entirely conclusive. There is still a need for validation experiments which compare FLDI to other measurements with high-frequency bandwidths such as PCB piezoelectric pressure transducers and small, fast-response hot-wires.

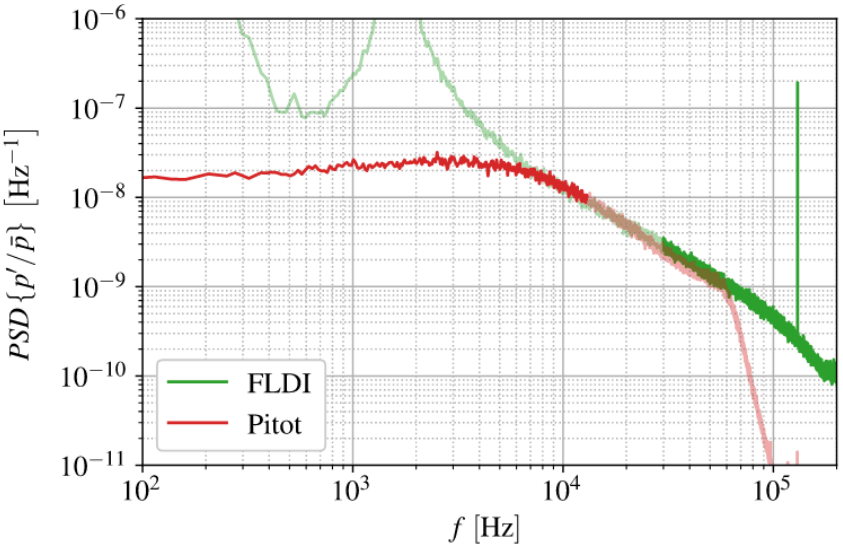

Fig. 20 Comparison of converted FLDI and pitot spectra of freestream disturbances in VKF Wind Tunnel D Run 183, M_∞ = 5, from Lawson *et al.* [105].

E. Signal Interpretation and Post-Processing Guide

The following is a short guide to interpreting and post-processing the FLDI signal.

1. Prior to the experiment

1) Set up the FLDI with a known laser wavelength, λ_0. Measure the beam separation, Δx, and the divergence angle, θ_d using a beam profiling camera. See Sections 3.4 and 3.5 of [75] for example.
2) The size of the measurement volume can be estimated as described in Section III.C. Ensure that scales of interest will be adequately resolved.
3) Characterize the photodiode's high-frequency response, H_{PD}, using a pulsed light source.

2. Prior to each test/run/shot

1) Characterize voltage phase curve by translating the Wollaston prim along the beam separation axis, or by using a phase retarder. Ensure the interferometer signal is near the middle of the fringe, V_0, during the most important test time.

3. Post-test

1) Convert voltage to phase difference using Eq. 9 or Eq. 10 to remove effects of laser power and photodiode circuit.
2) The 'local' refractive index gradient is proportional to the phase difference:

$$\frac{\partial n}{\partial x} \approx \frac{\lambda_0}{2\pi \Delta x Z_{\mathrm{SR}}} \Delta\phi \tag{25}$$

Qualitative comparisons to schlieren can be made. Be wary of the large uncertainty and scale dependence of Z_{SR}.

3) If the x-axis is aligned with the flow direction then the local refractive index is proportional to the integral of the phase difference with respect to time:

$$n(t) - n(0) \approx \frac{\lambda_0}{2\pi\Delta x Z_{\mathrm{SR}}} \int_0^t u_c \Delta\phi(\tau) d\tau \tag{26}$$

where u_c, the disturbance velocity, can be modeled or measured with multi-point FLDI, for example. The integral can be performed numerically. In practice this integral is easily corrupted by low frequency oscillations from laser power, stray light, or disturbances far from the focus.

4) If the flow is homogeneous, the local density can be found:

$$\rho(t) - \rho(0) \approx \frac{\lambda_0}{2\pi\Delta x Z_{\mathrm{SR}} K} \int_0^t u_c \Delta\phi(\tau) d\tau \tag{27}$$

where K is the Gladstone-Dale constant.

5) If interested in frequency spectra, fluctuations should be modeled and a transfer function, H, should be found and applied to the phase difference spectra. For example:

$$\mathcal{F}[\rho'] \approx \frac{\mathcal{F}[\Delta\phi](f)}{H(k)} \tag{28}$$

where $\mathcal{F}[]$ is the Fourier transform. The transfer function can be found by solving Eq. 11 analytically, numerically, or a combination of both and the result will contain a series of constants and unit conversions which make the sides of the equation equal in magnitude. A conversion between spatial and temporal frequencies is required:

$$k = \frac{2\pi f}{u_c} \tag{29}$$

Low frequency spectra will likely be corrupted, making measurements of overall turbulence intensity impossible in most situations. High frequency spectra will be free from noise, represent local fluctuations, and will be accurate in magnitude given the appropriate transfer function is applied. The cut-off frequency, f_c, can be determined using modeling and transfer functions. See Section 2.3.1 of [110] for example. Turbulence intensity is best found by restricting the signal to frequencies above this cut-off:

$$\frac{\rho'}{\bar{\rho}} \approx \frac{\Delta\phi}{\bar{\rho} H} \quad \forall f > f_c \tag{30}$$

IV. Multi-Point FLDI Techniques

This section discusses several methods used to create multiple FLDI beam pairs to enable measurements at several locations simultaneously. Such capability is highly valuable in hypersonic impulse facilities such as shock tunnels and Ludwieg tubes, where translation of the model or setup is not feasible. Furthermore, having simultaneous measurements at two or more positions enables signal correlation analysis, which is typically used in FLDI measurements to extract a convective velocity of disturbances or waves [42, 44, 114, 115]. An accurate convective velocity is critical for the conversion between spatial and temporal scales required in signal interpretation as discussed previously in Section III.E. The key assumptions made for the velocity calculation are (1) that disturbances do not significantly change as they convect from one measurement location to the next, and (2) that disturbances convect primarily in the direction between the measurement locations. These assumptions are reasonable if the measurement location spacing is small compared to the velocity gradients in the flow and if the spacing is oriented with the flow direction. The measurement often represents an acoustic wave velocity because of the application (hypersonic freestream and boundary layer flow) and high sensitivity to such waves. This can complicate the velocity measurement if acoustic waves are propagating orthogonal to the flow. Otherwise, if turbulence intensities are low and mean shear is negligible ($kU >> \frac{dU}{dy}$ [116]), it is reasonable to assume the convection velocity is equal to the bulk flow velocity (Taylor's frozen turbulence hypothesis [117]).

A. Additional Birefringent Prisms

The use of a Koester prism for two-point measurements was demonstrated by Smeets and George in 1971 (see Fig. 3 in Ref. [1]), and was initially used as a method to reduce the influence of vibrations on the measurements by providing a shielded second beam path for mean signal subtraction [1, 5]. The reason for using a Koester prism is that the split beams are made to converge such that they come to a focus in the Wollaston prism that is used to split each beam into two orthogonally polarized beams. This ensures that the two measurement beams (Koester beams) traverse the test section parallel to each other. After initially using a microscope slide to split the incident laser beam into two measurement beams using total internal reflection [114], Jewell *et al*. replaced the microscope slide with a Koester prism following the design of Smeets and George to make two-point measurements [115].

The difficulty with using a Koester prism for the beam splitting is that the laser must be incident at an angle relative to the optical axis. If the orientation of the two beams does not need to be changed after the initial setup, this does not pose a problem, but if the orientation of the beams is to be rotated about the optical axis, the laser and Koester prism must be fixed together to a rotation stage, complicating the setup. Weisberger *et al.* and Bathel *et al.* instead used a Nomarski prism for the beam splitting, which allows the laser to remain aligned with the optical axis, and where rotation of the beams requires only rotation of the Nomarski prism itself about the optical axis [44, 45]. This prism is used extensively in differential interference contrast (DIC) microscopy, where the overlapping of the two beams must occur outside of the prism (a modified Wollaston prism, where the optic axis of one of the prism halves has been rotated) [118]. By ensuring this overlap of the two beams occurs at the Wollaston prism, and thus at the focus of the field lens, the beams can be made to run parallel as they traverse the test section. This parallel beam propagation is important for unbiased velocity measurements, as discussed in Section IV.H. The Nomarski prism has found use in two-point FLDI measurements [44, 45, 119] and in two-line measurements using cylindrical optics [47, 48, 50].

As mentioned earlier, the Koester prism usage by Smeets and George was primarily used to obtain a second reference beam for vibration reduction of the primary beam's signal. However, in these early documents, multi-point systems (up to 8 simultaneous measurement points) were assembled, and used instead a set of Wollaston prisms to provide the initial beam splitting [1, 7]. The number of Wollaston prisms used was dictated by the number of measurement points desired. For example, for a two-point system one additional Wollaston prism was added on the pitch side, while for a four point system, two additional Wollaston prisms were added on the pitch side. The figure on page 18 of Ref. [1] shows a system with 8 pairs of laser beams. Three Wollaston prisms are used to split the initial beam into the 8 measurement beams, and the fourth Wollaston prism provides the typical splitting for each of the 8 beams. On the catch side, only the typical single Wollaston prism (matched to the pitch-side typical Wollaston prism) is used to make the orthogonal polarization beams in each of the 8 measurement beams colinear before interference at the filter and measurement at individual photodiodes. Each of the Wollaston prisms for the multi-beam system has a quarter-wave plate before it, used to convert the linear polarization of the two exiting beams from the previous Wollaston prism to circular polarization such that they are equally split into their further components at the next Wollaston prism. To ensure the multiple beams traverse the test section parallel to each other, another lens is required before the field lens and typical Wollaston prism to focus the multiple beams down into the Wollaston prism. The method of using multiple Wollaston prisms to create multi-point FLDI measurements has been used extensively [1, 7, 35, 40, 42, 61, 62, 66, 68–73, 75, 79, 80, 83, 88, 89, 92, 120, 121], with some of these using a separate additional optic to split the beam into further points [66, 68, 69, 120]. Note, however, that not every usage includes the additional lens needed to ensure parallel beams through the test section, and so the beams will instead be angled between the field lenses. If not using the beams for velocity measurements, this configuration can be acceptable, but when convective velocities are being measuring, the most accurate implementations will include an additional focusing optic.

While the main polarizing prisms used for splitting into multi-beam systems were described above (Koester, Nomarski, Wollaston), other polarizing prisms could in theory be used [122], although the focusing of the output beams into the Wollaston prism for parallel beam traversal in the test section would need to be carefully considered. For example, Rochon and Sénarmont prisms split an input beam into two orthogonal polarization beams, with one beam continuing parallel to the optical axis with the other beam angled slightly. A beam displacer (e.g., a calcite beam displacer) could be used, where one beam continues along the optical axis while the other beam is displaced a fixed distance, but remains parallel to the optical axis. A variable beam displacer can be used, where the separation distance between the two parallel beams can be changed [123]. Another method of achieving an adjustable offset of parallel beams is shown in Ref. [92], where a non-polarizing beamsplitter and a mirror are used to split the first beam into two beams, and then reflect the second beam parallel to the first. For all these options, the additional lens mentioned in the previous paragraph would still be required to focus these beams into the Wollaston prism to ensure parallel traversal of

the beams across the test section.

B. Cylindrical Optics Line FLDI

As mentioned in Section II.C, the use of cylindrical optics in an FLDI system was outlined by Smeets [7]. The elongated ellipse (called a *line* hereafter) that forms at the beam focus can be measured not by a single photodiode (as is sometimes done with cylindrical optics, see Section II.C), but with a linear array photodiode. This effectively enables a multi-point measurement from a single beam, where the spatial resolution is limited by the dimensions of the linear array photodiode pixel size and the magnification of the laser line on the photodiode array [47, 48, 50, 51].

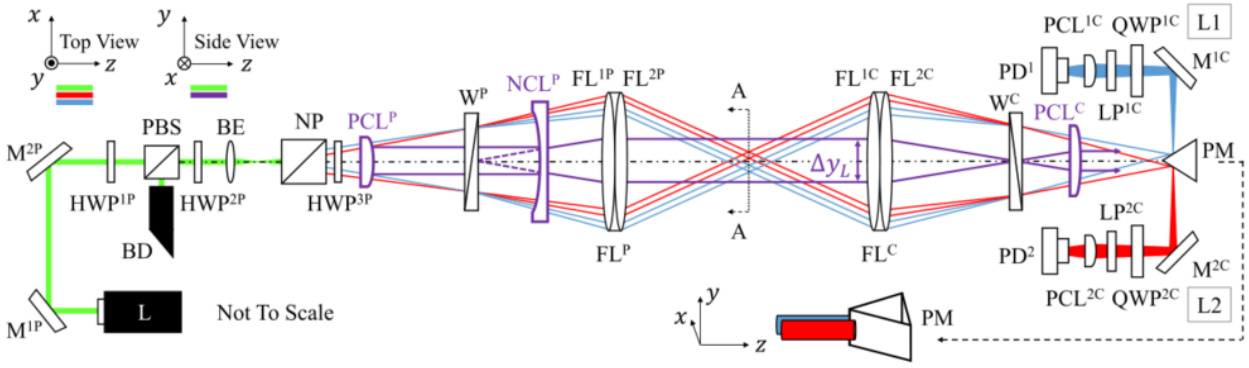

Fig. 21 Schematic of a two-line FLDI system used for multi-point sampling of a flowfield [47]. The cylindrical optics allow for measurement along a line, and a Nomarski prism is used to make a two-line measurement. Used with permission from NASA.

A schematic of a two-line FLDI system using cylindrical optics is shown in Fig. 21. A positive cylindrical lens (PCL^P) and a negative cylindrical lens (NCL^P) are used to expand the line to the correct size for passage through the test section. The PCL^P is positioned one focal length away from the focal point of the beam expander (BE) in order to collimate the beam in one direction. The NCL^P is positioned one focal length away from the Wollaston prism (W^P) such that the expanding line is collimated through the test section (since the W^P is located at the focal point of the field lens (FL^P). To make measurements at two closely spaced lines, a Nomarski prism was added, which overlaps the two lines at the W^P, ensuring parallel propagation of the two lines through the test section. The lens choices on the pitch side of the system (left side of the schematic) dictate the physical size of the laser line in the flowfield, while the lenses on the catch side (right side of the schematic) dictate the resolution of the measurement along the laser line.

Example results from two flow cases using the line FLDI system are shown in Fig. 22. In Fig. 22a, 16 channels of a linear array photodiode made measurements of a shock wave from a spark generated via laser-induced breakdown, where the sequential registration of the shock wave's signal is visible from channel 1 to 16, and where the reflected shock wave from the table below the measurement registers as signal in the reverse direction in the inset. In Fig. 22b, the utility of a line measurement was demonstrated when making measurements of second mode disturbances in the boundary layer of a flat plate. Here, the plate covers the bottom channels (14, 16) and channels 2 through 12 measure flow fluctuations through the boundary layer. A second mode wavepacket was observed as outlined in the dashed black line, and the line measurement was able to determine that the region of highest intensity fluctuation is some finite distance above the surface of the plate.

High resolution measurements along a line are possible with this system, but the increase in measurement points requires and increase in acquisition channels. No off-the-shelf linear array photodiode system was ready to use for the system described above, and so custom fabrication was required. A simple reverse biased circuit can be used in some instances [47, 48, 50], but for optimization of the acquired signals based on the laser power, optic transmission attenuation, beam splitting, and oscilloscope specifications, a custom solution may be required [51]. The cost of multi-channel oscilloscope modules with high bandwidth and simultaneous sampling is on the order of many thousands of dollars, and so systems with higher acquisition channels can balloon in cost. Because it is the data acquisition system (oscilloscope) that has the increased cost, not the linear array photodiode and associated amplifier boards, this is a limitation for any multi-channel measurement system. Alignment of the line FLDI system requires greater care than a

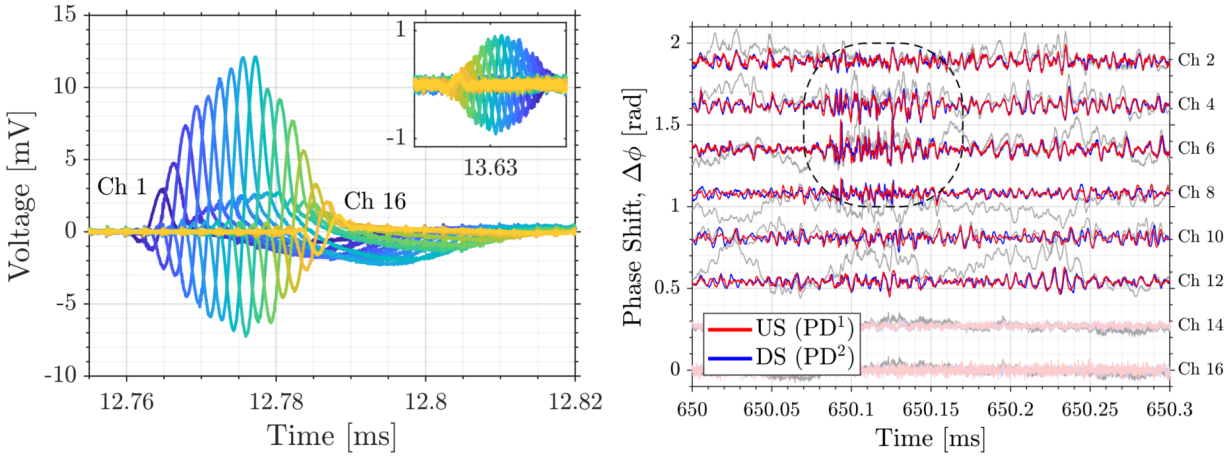

(a) **(b)**

Fig. 22 (a) Response of 16 channels to a traveling shock along major axis of beam. (b) Flat plate boundary layer wall-normal measurement with second mode wave packet outlined in dashed black, with upstream (US) and downstream (DS) lines identified. Used with permission from NASA.

single-point or two-point measurement, because the length of the line at the beam focus is determined by the cylindrical lenses on the pitch side, decisions about this line length must be made during the system assembly process. The spatial resolution along the minor axis of the beam is on the same order as a normal FLDI system (Gaussian beam waist), but along the major axis of the line, the spatial resolution is dictated mainly by the linear array photodiode pixel size. There are many options for off-the-shelf linear array photodiodes with different pixel sizes and number of channels, but these must be incorporated into the design early in the system design.

C. Diffractive Optical Elements for Linear Array FLDI

Diffractive optical elements (DOEs) are optical components that operate based on principles of diffraction rather than refraction, and they offer unique beam shaping and splitting capabilities. Gragston *et al.* [33] introduced the use of diffractive optics with FLDI systems for efficient beam splitting, examples of which are shown in Fig. 23, where images were taken with a beam profiler camera at the focus point of the FLDI system. A single 6×1 DOE was used to obtain the pattern in Fig. 23(a), while two of these 6×1 DOEs were used for the patterns in Fig. 23(b) and 23(c). In Fig. 23(b), the two DOEs were rotated 90° relative to one another to produce a square 6×6 grid of points, while in Fig. 23(c), the DOEs were rotated to an angle less than 90° relative to one another to change the orientation of both the 6×6 grid, and also the Wollaston-separated beams at each grid point. These images show the versatility in the generation of arrays of grid points using DOEs.

The 6×1 DOE of Fig. 23(a) was used to measure the screech tone in a Mach 1.5 jet [33, 81]. This DOE was designed with a separation angle of 0.71° for a design wavelength of 633 nm, and the grid was aligned horizontally, with measurement points extending from the center of the vertically-oriented jet near the nozzle out exit out to the edge of the jet. Both high-speed photodiodes and a high-speed camera were used to make measurements, with resulting spectra for all six measurement points shown in Figs. 24b and 24a, respectively. Note that due to the sampling rate/frame rate differences between the two measurements, the frequency bounds on the x-axis are different, and due to the changing intensity of the screech tone measurement, the y-axis limits also change between plots. Point 1 is located at the centerline of the jet, with incrementing numbers increasing in radial distance from the jet center out to the jet edge. For all measurement points, the screech tone at 17 kHz was identified, both in the camera data and the photodiode data, and beams near the outer edge of the jet measured higher amplitudes of the screech tone, as expected.

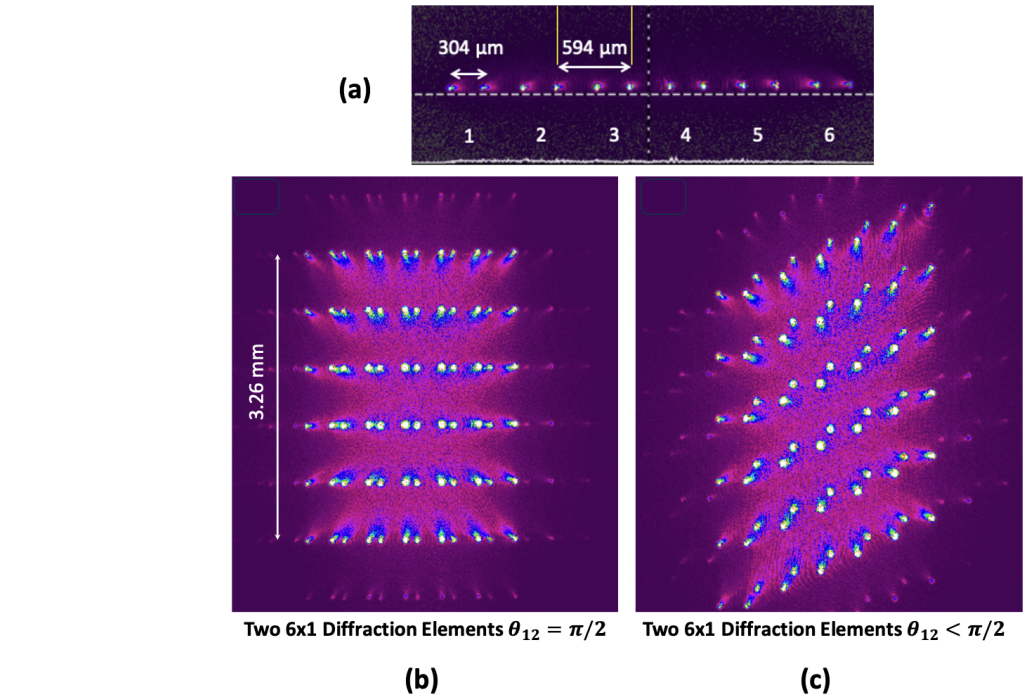

Fig. 23 Example arrays of FLDI beam pairs created using diffractive optics [81]. (a) A linear distribution of six beam pairs from a single diffractive optic (6 × 1). (b) A two-dimensional array of FLDI beam pairs and (c) a parallelogram arrangement created by two diffractive optics. Used with permission from author.

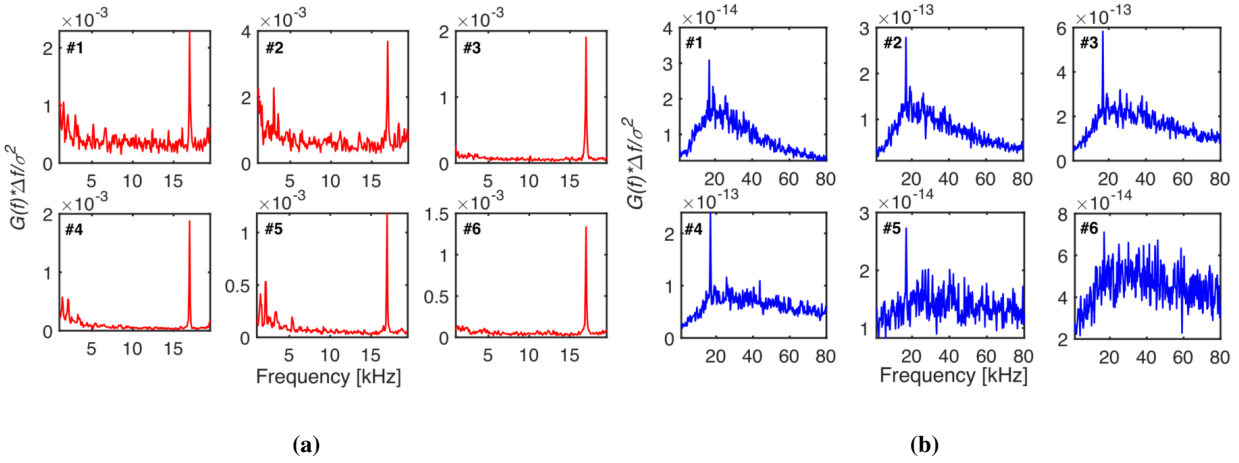

Fig. 24 Mach 1.5 jet screech frequencies measured at six points using the (a) high-speed camera based measurement method and the (b) fiber-optic-coupled photodiode measurement method. Used with permission from author.

When purchasing a DOE, the number of points, the divergence angle of the split beams, and the working wavelength all need to be specified. Using the DOE with an off-design wavelength laser causes the beams to split unevenly in power, and produces a zeroth-order diffraction beam at the center of the grid, which generally has higher power than the other diffracted first-order points (and thus reduces the power available to the other beams). Though DOEs can cost as much as a Wollaston prism, they can be designed for any distribution of points and can also be used together with additional Wollaston prisms or other DOEs to increase the number of measurement points, and the overall footprint in multi-point

setups can be reduced compared to the classic multiple-Wollaston prism approach. Finally, because the beams have a fixed splitting angle, ensuring the beams are captured on their respective photodiodes on the catch side of the FLDI instrument requires care, and several methods are discussed in Section IV.G.

D. Microlens Array

Another method of producing an array of measurement points is by using a microlens array (MLA), such as those that have been widely used in Shack-Hartmann wavefront sensors and for plenoptic imaging. These MLAs typically have short focal lengths, and can be used as the initial expansion optic if allowed to focus and then diverge. Marsh *et al.* used an MLA-based FLDI system to make measurements of an under-expanded jet [94]. While both DOEs and MLAs can generate a grid of points from a single optic, the DOEs operate using diffraction and split the single input beam into a diverging grid of beams, while the MLA uses refraction at each of the microlenses to create the individual beam points. The manufacturer of the DOE specifies a suggested input beam diameter for optimum operation, while the MLA typically requires an input beam with large enough diameter to cover the entire grid of the microlenses. This may require expansion and subsequent collimation of the laser beam before it is incident on the MLA.

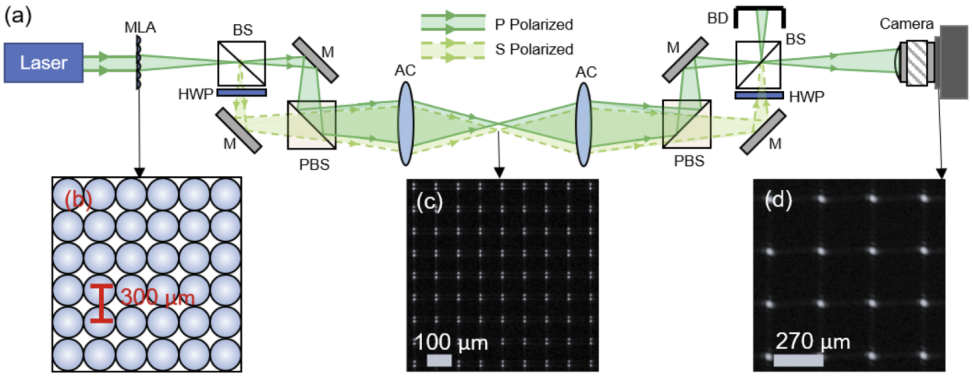

Fig. 25 (a) The FLDI setup developed by Marsh *et al.* [94] utilizes a microlens array to create multiple FLDI points. Detailed images show (b) a schematic of the microlens array, (c) the FLDI beams at the focal plane, and (d) the beams at the detection plane as view by a camera. The red text in (b) shows a lens spacing of 400 μm. Used with permission from Optica.

A schematic of the MLA-FLDI system used by Marsh *et al.* is shown in Fig. 25. After expansion and collimation of the laser beam (not shown in the schematic), the beam passed through a 33×33 MLA. A polarizing Mach-Zehnder configuration was then used to split the beams into their orthogonal components, instead of the typical Wollaston prism splitting method (see further information in Section VII.D). Using the Mach-Zehnder configuration allowed for precise adjustable beam separation control, in contrast to the fixed splitting when using a Wollaston prism (although note that adjustable splitting is also possible with the Sanderson prism). The mirrors (M) are used to adjust the offset and position of the projected beams. On the catch side of the system, a similar configuration is used to make the beam colinear, again with precise adjustments enabled by the mirrors. This adjustment is the equivalent of ensuring the catch-side Wollaston is in the correct location along the optical axis to make the beams colinear. A comparison of a schlieren image of the under-expanded jet and the MLA-FLDI system shows a good comparison of the jet structure (not pictured here, see [94]). While the MLA-FLDI results in an image of the jet at a much lower resolution than the schlieren camera (limited to the resolution of 33×33 MLA), the turbulence information can be directly obtained with high sensitivity. Measurements of a jet with a screech frequency at 14.1 kHz were also performed, further demonstrating the system's ability to resolve frequency structures at measurement points in the grid.

While a Mach-Zehnder configuration was used above, the MLA can also be incorporated into a traditional FLDI setup by replacing the expansion lens with the MLA and adjusting the spacing of the subsequent optics appropriately. Off-the-shelf MLAs typically cost a few hundred dollars, and can be used over wide range of wavelengths (hundreds of nm). These MLAs can be placed in rotation mounts so that the beam grid can be rotated about the optical axis. If using the Mach-Zehnder configuration for the beam splitting, greater care must be taken when adjusting the rotation of the splitting (equivalent to the rotation of the pitch and catch Wollaston prisms in a conventional FLDI system). For

higher density beam grids, a higher power laser will generally be required to ensure sufficient intensity of the light in each beam. With the increase in beam grid points when using an MLA, acquisition with individual photodiodes is not feasible, and a high-speed camera is required, as shown in Ref. [94]. The dual-DOE method of creating points allows for skewed grids by rotating the DOEs relative to one another, but MLA-based systems have a fixed grid shape defined by the MLA itself. Current camera technology limits the MLA-FLDI measurements to lower frequencies (frame rates) than would be attainable with photodiodes, and at higher frequencies (frame rates) the image resolution is decreased, sometimes drastically for the highest achievable imaging frame rate. A balance between beam intensity, imaging frame rate, spatial resolution, and pixels per beam point is required.

E. Spatial Light Modulator

While the previously described DOE and MLA methods of creating multiple beams are versatile in terms of the beam grid size and spacing (virtually any configuration of beam splitting, shape, size, and splitting angle can be attained with DOEs), these grids are fixed for each optic, and typically require new optics for changes to the grid number and shape (although spacing of the beams can be adjusted in the MLA system). A dynamic method of generating multiple beams uses a spatial light modulator (SLM), as demonstrated by Holladay and Zhang [78]. This initial demonstration shows the generation of a ring of laser grid points around a central point, with the Wollaston beam separation in the horizontal direction of approximately 105 μm, as shown in Fig. 26.

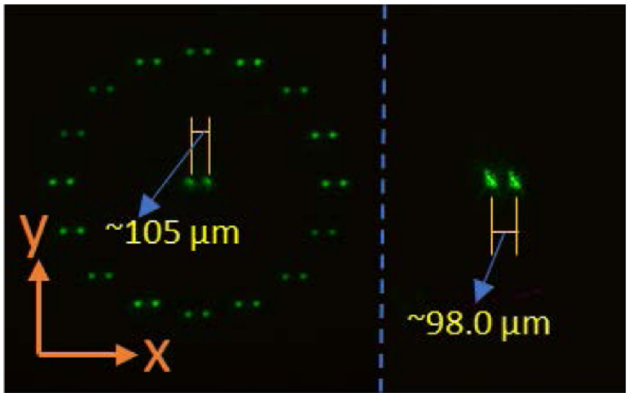

Fig. 26 FLDI beam array in the shape of a circular ring with a central point, demonstrating arbitrary beam array creation from the SLM [78]. Used with permission from Optica.

Testing was performed by Holladay and Zhang [78] with the SLM-FLDI system using a Mach 1.5 jet, with the beam array located in close proximity to the nozzle exit and the first expansion fan, and photodiodes were used for the data acquisition, although high-speed cameras can also be incorporated. Results from a single-point FLDI and the SLM-FLDI showed similar frequency peaks in the power spectral density plots, although the difference in the distribution of the energy over the frequency spectrum and the roll-off of the signals needs further investigation. The cost of a commercial off-the-shelf SLM is on the order of many thousands of dollars, but the flexibility of the beam configuration may be appropriate for certain applications where cost of this beam splitting optic is not prohibitive.

F. Scanning Point FLDI

The previous subsections have focused on systems that make measurements at multiple points simultaneously. If the duration of test time at a fixed condition is sufficient, a single point (or multi-point) FLDI system can be scanned to make measurements at different spatial positions. Smeets described a system where the points in the test section could be displaced in a parallel fashion by turning a small mirror, as described in Section 5a and shown in Fig. 19 of Ref. [7]. Another method of using a single-point system to make measurements at multiple points is by linking the pitch and catch systems together on a single breadboard, and moving the entire FLDI system to scan the focus point. This was used by Pandey *et al.* to translate the FLDI focus point in the streamwise direction while making measurements on a cone-slice-ramp geometry [124]. Gui *et al.* used a similar system, where adjustment of the FLDI system was made using a motorized linear stage to move the two-point measurement in steps of 0.025 mm to eight positions along the

surface of a 7° half-angle cone with distributed roughness along its surface [119]. Finally, Xu *et al.* independently mounted the pitch and catch sides of the FLDI system to three-dimensional translation stages, where both sides of the system could be moved synchronously, to make measurements of an ultrasonic standing wave in a water tank [125].

G. Multi-Point Data Acquisition

Depending on the number of measurements points, data acquisition systems can range from simple to quite complex. For roughly two to four measurement points, it is simple to add a second/third/fourth photodiode and acquisition channel(s) [35, 40, 44, 45, 61, 62, 70, 72, 73, 75, 79, 80, 83, 88, 89, 114, 115, 119, 121]. Because the photodiode elements cannot be located directly next to each other due to the typical photodiode housing/electronics, methods of providing enough separation of the beams include using a lens to angle the beams away from each other, using a prism mirror to reflect the beams away from each other, and simply letting the beams continue to diverge until they are separated enough. For greater than four measurement points, using individual photodiodes is still possible, but likely requires additional optics to separate the beams from one another.

For many of the multi-point FLDI systems that use DOEs, six measurement points are arranged in 6×1 line, and instead of arranging the photodiode units next to each other and using an assortment of lenses and mirrors to direct the beams onto their respective sensing element, smaller-footprint fiber optic cables with associated collimation optics were used to collect the light, and the other end was connected directly to the individual photodiodes located some convenient distance away [33, 58, 65, 67, 81, 82, 84–86, 126]. For some measurements, twelve total points are arranged in a 6×2 array, and two of the 6-channel fiber arrays were used side-by-side [66, 68]. Note, however, that the fibers lead to signal loss due to inefficiencies and vibrations near wind tunnels, which can cause the beams to vary in position while focusing into the fiber core, leading to large, low-frequency signal oscillations. To mitigate this problem, Davenport *et al.* took OEM-packaged photodetectors and separated the photodiode from the amplifier board [69]. The photodiodes were then arranged on a circuit board similar to the mounting strategy of the fiber collimators of the previous designs. Wires were then used to connect the photodiode pins back to the amplifier boards, which were located a convenient distance away, eliminating the need for precise fiber-coupling. This method of separating an OEM photodetector has been used recently by other authors [113, 120].

For multi-point cylindrical lens FLDI systems, the number of measurement points is dictated by the number of channels of the linear array photodiode, with current systems using either 16 channels [47, 48, 50] or 35 channels [51, 127]. A detailed guide for the design of the photodiode circuit board, amplifier circuit boards, and data acquisition system with software interface is given in Weisberger *et al.* [51]. With the increasing number of individual photodiode elements in the linear array, more acquisition channels are needed for the oscilloscope. The 35 channel system uses five 8-channel scope modules to acquire and digitize the data, and while the increased spatial resolution at high sampling rates is desired, the cost associated with the data acquisition itself can become prohibitive. Note that this increased cost is solely due to the number of acquisition channels required; the cost of the linear array photodiode and electronics required to build the amplifier circuit are on roughly the same order as purchasing pre-made photodetectors. Thus, the prohibitive cost is linked only to the higher number of channels of data acquired, which remains a limiting factor for any method of increasing the number of measurement data points.

A final option that has been explored is to use high-speed cameras for multi-point acquisition. High-speed camera acquisition has found use particularly with DOE-based FLDI systems [33, 59, 60, 77, 81, 109, 128], microlens array based FLDI systems [94], and spatial light modulator FLDI systems [78] due to their larger separation between individual beams as compared with the cylindrical lens based FLDI systems. This beam separation allows for isolation of individual beams on the camera sensor and in images during post-processing. Cameras allow for high spatial resolution measurements at the expense of sampling rate; there is a trade-off required between number of pixels in the images and the framing rate of the camera. Furthermore, cameras tend to have limited bit-depth, which can reduce sensitivity to small changes in intensity.

H. Parallel Beam Propagation

If a multi-point FLDI system is assembled to make convective velocity measurements, care must be exercised to ensure the multiple points propagate parallel through the test section. A schematic of both a parallel and non-parallel two-point FLDI system are shown in Fig. 27, where only the pitch side of the system up to the focus plane is visible. In the top schematic, a parallel beam propagation system is depicted. The beam expander (BE) first focuses the laser

beam and then expands it, and the first Wollaston prism (W^1) is used to split the beam into two separate measurement beams. A lens (L) then focuses the two beams (red, blue) down to a focus inside the second Wollaston prism (W^2), where W^2 splits each of the two measurement beams into the closely spaced orthogonal polarization beams (depicted with appropriately colored solid lines), as they pass through to the field lens (FL). Because W^2 is located at the focal point of FL, the two measurement beams propagate parallel to one another through the test section, and the orthogonally polarized beams within each multi-point beam also propagate parallel to each other.

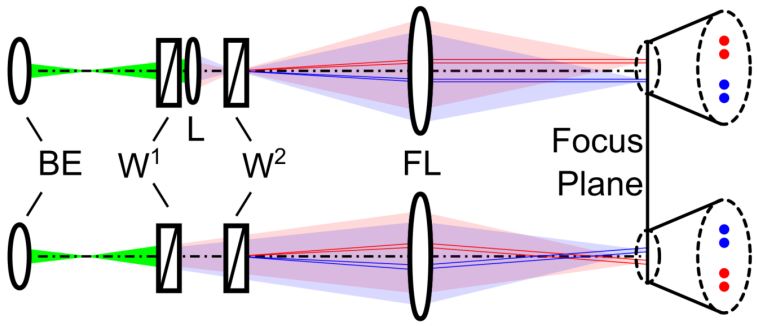

Fig. 27 Two-point beam propagation using a (top) parallel beam arrangement and a (bottom) non-parallel beam arrangement.

In contrast, the bottom schematic in Fig. 27 depicts a non-parallel multi-point FLDI arrangement, where the only difference from the top schematic is that the lens (L) has been removed. Here, the focusing and expanding beam from the BE is split into the two measurement beams (red and blue regions) at W^1, and continue expanding towards W^2, where each measurement beam is split into its orthogonal polarization components. Because the W^2 is located at the focal point of the FL, the orthogonal polarization components (colored lines) traverse the test section parallel to each other, but because the splitting point of the two measurement beams occurred at a distance farther from the focal point of the FL, the beams do not run parallel through the test section, and are instead angled with respect to each other and the flow. This can impart a bias in the convective velocity measurement since the offset between the two measurement beams changes, and which is a critical component of the velocity calculation (i.e., the dx in $v = dx/dt$). If the FLDI operated as an ideal point measurement exactly at the focus plane, this would not be an issue, but because the sensitivity region depends on the FLDI system's optics and the flow that is being measured, it can be difficult to account for this bias in the beam spacing.

There are several options for ensuring parallel beam propagation through the multi-point FLDI system, some of which were outlined in Section IV.A. The first is through the use of a either a Koester prism or a Nomarski prism, since these cross the split beams outside of the prism, and can be made to cross at the Wollaston prism (W^2 in Fig. 27). Because the laser beam must be coupled into the Koester prism at an angle, this option is more complicated to use than the Nomarski prism, which allows the incident laser to be aligned with the optical axis of the FLDI system [44, 45, 119]. The Nomarski prism has also been used with cylindrical lenses to make multi-point measurements, since the cylindrical lenses only affect the focusing in one direction [47, 48, 50]. The operation of the Koester and Nomarski prisms can be thought of as a single optic that achieves the same result at using a Wollaston prism followed by a focusing lens (as shown in the top schematic of Fig. 27). The diverging beams from the exit of the Wollaston prism are focused by a positive lens such that the focus point coincides with the last Wollaston prism, a method which has also been used to ensure parallel beams across the test section [40, 92]. Note that the focusing lens method can also be used with systems that employ a DOE to split the incident beam into a 1D or 2D grid of beams, as mentioned in Gragston *et al.* [33].

V. Applications of FLDI for Flow Measurements

In this section, a few examples of FLDI use in measuring various flow fields are presented to provide context to the overall capability of the instrument, including laminar and turbulent jets (Section V.A), transitional and turbulent boundary layers (Section V.B), wind tunnel freestream fluctuations (Section V.C), and reacting, high-temperature flows (Section V.D).

A. Jets

Laminar jets have been used to help characterize FLDI performance. Schmidt and Shepherd [96] developed a ray tracing method for studying FLDI (see Section III), which they validated with a laminar argon jet. Running both an experiment and a simulation with FLDI, they compared the measured and computed beam phase change ($\Delta\phi$) values and found excellent agreement. Lawson *et al.* [104] also used a laminar jet to compare experimental and computational FLDI performance. A helium jet was used, with experimental measurements made simultaneously by both an FLDI system and a Mach-Zehnder interferometer, and where simulations of the generated flow field were used to understand the spatial characteristics of FLDI to validate the computational model.

Narrow-diameter turbulent jets have been a canonical flow in the FLDI literature. They have primarily been used to probe the FLDI sensitivity region [19, 39, 49, 79]. These types of experiments have generally been designed similar to the description shown in Figs. 3 and 13. The FLDI response from the jet at each station along the optical axis is recorded, and the RMS of the response is plotted as a function of z (such as in Figs. 3 and 14). Turbulent jets provide a generic dynamic broadband input for the FLDI, and the resulting function of FLDI response at each z position provides a simplified understanding of how well the FLDI suppresses signals away from its foci.

In addition, turbulent jets have been used to provide a well-documented flowfield for FLDI calibration [24, 74, 75, 99]. With well-defined descriptions of their density fields in the literature, researchers were able to convert the directly-measured beam phase change values to dimensional or normalized density fluctuations.

There have been a few cases of turbulent jets being used to test other aspects of FLDI. In 2017, Ceruzzi and Cadou [41] used a turbulent jet to compare the difference in responses between LDI and FLDI. Jewell *et al.* [115] used a jet as an generic flowfield for two-point FLDI convective velocity estimation. At the same time, Ceruzzi and Cadou [42] also used a jet for two-point FLDI. Jets that produce a screech tone have also been used as a test case for new configurations of FLDI [83, 94].

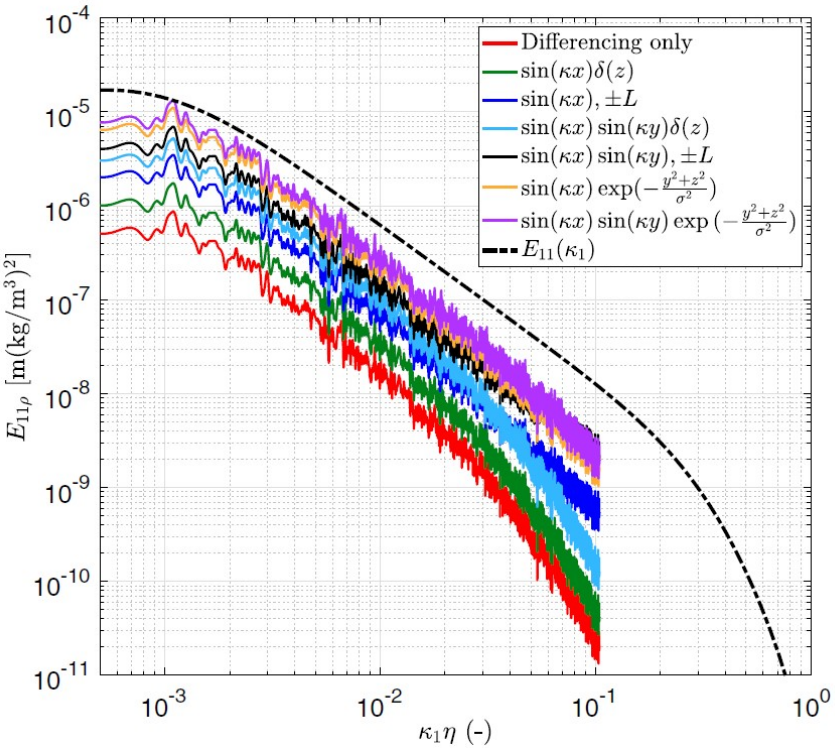

Fig. 28 Results from Hameed and Parziale [99] showing one-dimensional energy spectra of the density fluctuations for an experiment performed with a round turbulent jet, corrected by transfer functions for disturbance fields as labeled.

B. Transitional and Turbulent Boundary Layer Flows

FLDI is well-suited for measurements of transitional and turbulent boundary layers due to its high response rate and ability to resolve small-scale fluctuations. Turbulent boundary layers have characteristic frequencies that scale as $f_c \sim U_e/\delta$, and for high-speed flows U_e is $O(10^3$ m/s) with δ being $O(10^{-3}$ m). Thus, a MHz sampling rate or higher is desirable for studying these flow fields. Transitional boundary layers follow similar scaling relations, and much of the recent work with FLDI has been oriented around quantitatively measuring instabilities in transitioning hypersonic boundary layers [21, 44, 45, 50, 61, 65, 82, 109, 120, 126, 129, 130].

Parziale *et al.* [18] used FLDI to measure the second-mode instability on a 5° cone in the CalTech T5 shock tunnel, which revived interest in FLDI for studying high-speed transitional boundary layers. An example of the measurement and comparison of results to linear stability calculations from that work is provided in Fig. 6. The measurements showed that the second-mode instability, a dominant instability mechanism in hypersonic laminar boundary layers, can be measured with FLDI. Since then, FLDI has been used reliably to measure the second-mode instability [44, 45, 50, 82, 126, 129, 130] in a number of flows with various wall temperature conditions and total enthalpies.

Figure 29 shows work by Siddiqui *et al.* [120], which explored how FLDI measurements in two transitional flows correlated to surface heat transfer information, another common means used to study transitional flows. The results show that even in non-second-mode dominated transition, FLDI can provide quantitative information about the flow conditions. Specifically, it shows that the increase in density fluctuation amplitudes detected by FLDI was consistent with a simultaneous increase in surface heat transfer during transition. Several authors [65, 126, 129, 131] have also shown that FLDI is capable of resolving wall temperature effects on boundary layer transition as well.

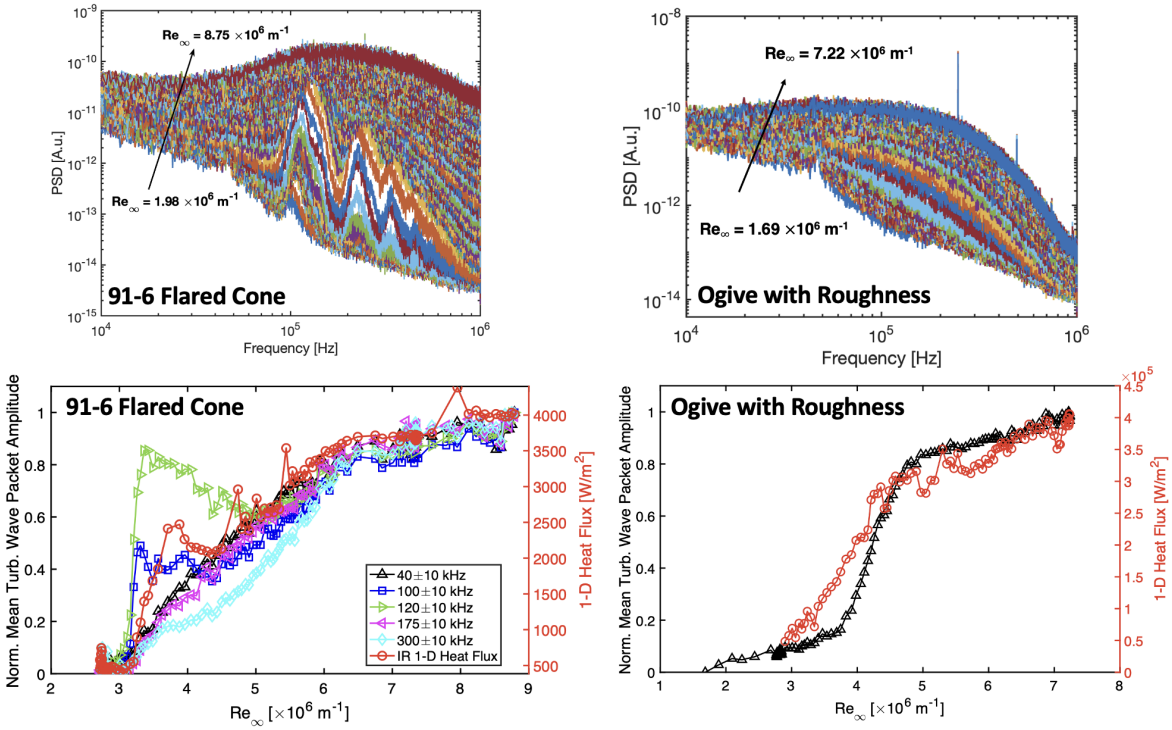

Fig. 29 Results from Siddiqui *et al.* [120] showing power spectra from FLDI in a transitional boundary layer and how the mean amplitude of density fluctuations in different frequency bands evolves in comparison to 1D heat flux determined from IR thermography. Used with permission from the authors.

While surface pressure sensors can provide information about instabilities associated with high-speed boundary layer transition, such sensors are limited to measurements at the surface, whereas FLDI is capable of probing off-body positions. This was used by Benitez [132] to observe and study instabilities in the shear layer at different wall-normal heights near a compression surface. The results, shown in Fig. 30, demonstrate the utility of off-body measurements for

understanding flow dynamics. This type of measurement has also been shown to reveal fluctuations in both the shear and shock layers using LA-FLDI for a cone-flare configuration [128].

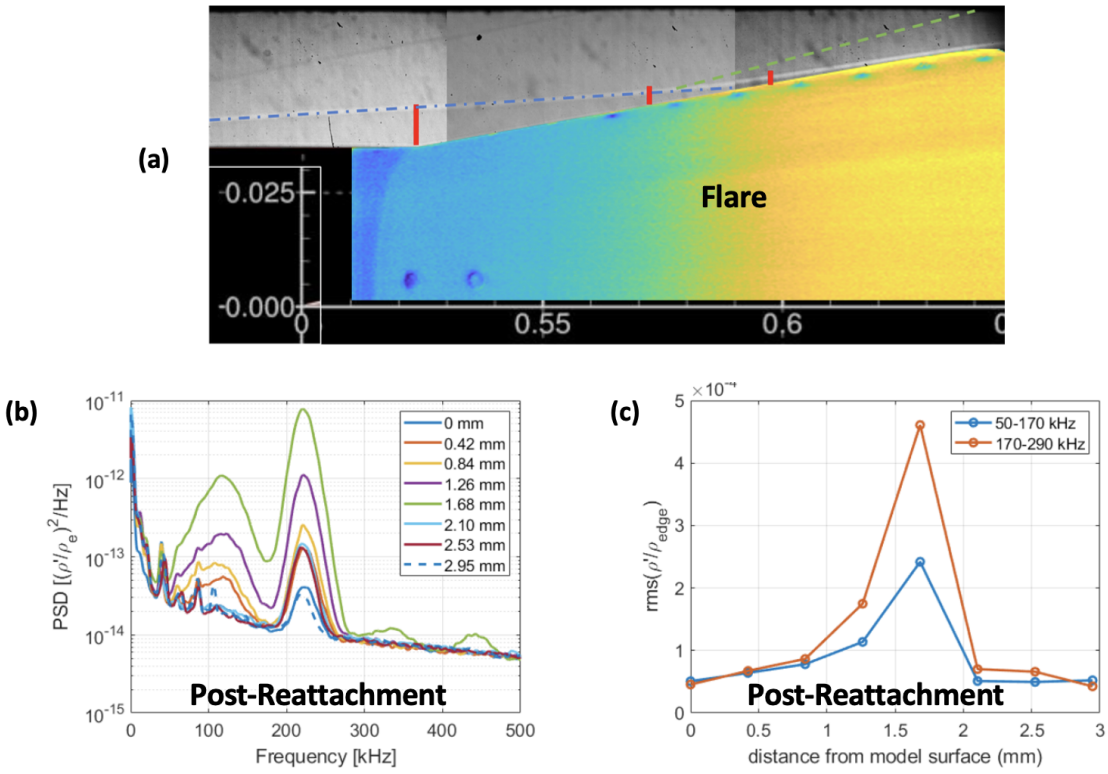

Fig. 30 Results from Benitez [132] showing fluctuation spectra and RMS magnitudes from FLDI measurements at different wall normal positions in the reattached boundary layer on a cone-cylinder-flare geometry in Mach 6 flow. Used with permission from Benitez.

FLDI has also been applied for measurements of compressible turbulent boundary layers [34, 59, 68, 72, 92], with spectra similar to those shown in Fig. 29 providing details about fluctuation content. In such flows, measurements of disturbance convective velocity are also quite common. Figure 31 shows results from Ceruzzi *et al.* [72] comparing a Mach 2.7 turbulent boundary layer convective velocity profile from two-point FLDI measurements with other measurement techniques and calculations.

C. Wind Tunnel Freestream Turbulence

FLDI is a good candidate for characterizing freestream turbulence or "tunnel noise" because it is sensitive enough to detect the relatively weak fluctuations (typically $p'/p_\infty < 0.05$) and it has the ability to spatially filter the relatively stronger shear and boundary layers near the sidewalls and windows of the facility. As discussed in the introduction, Parziale *et al.* [20] were the first to demonstrate these measurements in Caltech's T5 facility, where Fig. 4 shows a sample of the spectra measured. Not long after, Fulghum [24] and Settles and Fulghum [133] characterized freestream turbulence in Penn State's supersonic tunnel as well as in Arnold Engineering Development Complex Hypervelocity Wind Tunnel 9 (AEDC T9). They introduced methods for simulating the FLDI's response and suggested that the low-wavenumber spectra would be contaminated by signals from sidewall boundary layers. Birch *et al.* [27] demonstrated this low-wavenumber contamination experimentally by using shrouds to shield the beams from the sidewall turbulence in University of Southern Queensland's Mach 6 facility (TUSQ). Spectra measured with and without the shrouds were in agreement only for $k > 10^3$ m^{-1}, and $f > 200$ kHz. Lawson and Austin [134] investigated the effects of gas composition and sound speed on freestream disturbances in Caltech's Hypervelocity Expansion Tube (HET), testing the acoustic theories of Paull and Stalker. Ceruzzi *et al.* [73] used a two-point FLDI to measure both spectra and

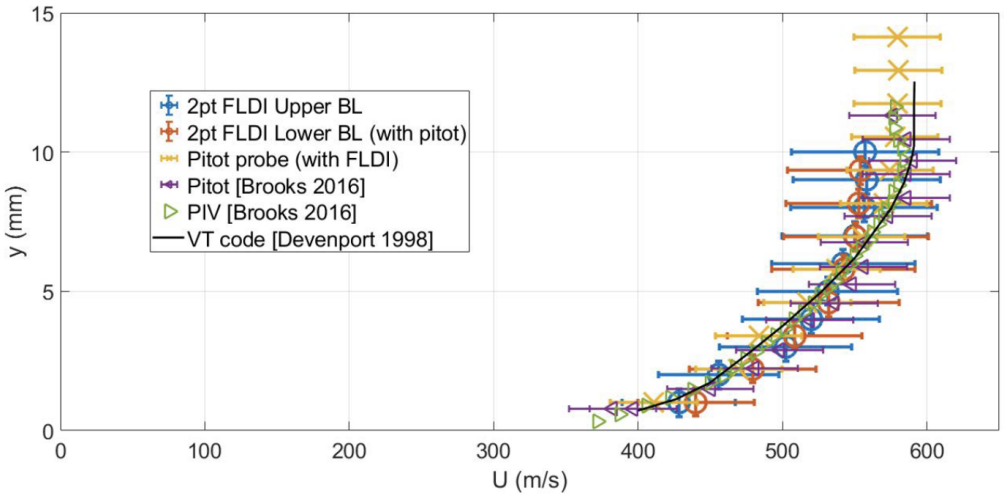

Fig. 31 A plot of a Mach 2.7 turbulent boundary layer velocity profile obtained from FLDI by Ceruzzi *et al.* [72] with comparison to various other methods and computations. Used with permission from Ceruzzi.

disturbance velocity in the freestream of AEDC T9's new Mach 18 nozzle. Gillespie *et al.* [35] took this set-up a step further by employing a three-point FLDI to measure correlations along streamlines and Mach lines simultaneously in the freestream of University of Maryland's HyperTERP reflected shock tunnel.

The sensitivity and spatial resolution to freestream turbulence was investigated computationally by Benitez *et al.* [106]. Ceruzzi [110] suggested an updated method for modeling and predicting the useful bandwidth of freestream measurements, an extension of the methods first suggested by Fulghum [24]. A consequence of the bandwidth restriction is that FLDI cannot directly measure a full spectrum for computing the overall percentage "tunnel noise", and some other measurement or modeling is required to capture the low frequency spectra. This was demonstrated by Lawson *et al.* [105] who combined FLDI with pitot probe measurements to reproduce the full freestream spectrum in VFK wind tunnel D - a selection of these spectra are re-plotted in Fig. 32. The plotted spectra have been transformed from the raw data using transfer functions which account for the inclination angle of freestream acoustic waves. Accurately predicting inclinations angles is important because the sensitivity of the transfer functions to inclination angle is large [135]. Recently, Ceruzzi *et al.* [113] demonstrated a possible method for directly measuring these inclination angles using multi-point FLDI in University of Oxford's High Density Tunnel (HDT); a schematic of the multi-point arrangement and a snapshot of the results are shown in Fig. 33, with comparison to historical hot-wire measurements [136] and computational studies [137] of acoustic waves radiating from flat plates.

D. Reacting, High-Temperature Flows

FLDI is an appealing technique for reacting flows because it is completely non-intrusive, thus it can easily be employed in harsh, high temperature environments provided suitable optical axis. One challenge is the risk of phase ambiguity which can complicate signal interpretation; phase ambiguity arises when large refractive index gradients cause the interferometer to exceed one interference fringe (see Fig. 11). As Smeets and George [7] point out, this can easily be avoided with the choice of beam separation (Δx). Thus, it is good practice to design an FLDI with sufficiently small beam separation for reacting flows. As always, it is good practice to conduct some modeling of the expected signal using the theories discussed in Section III (and references within) prior to designing and constructing a new FLDI set-up.

FLDI's speed and spatial resolution make it particularly appealing for applications in small scramjet combustors. Despite this, only two examples are published to date. Ananthapadmanaban *et al.* [107] used FLDI to characterize "noise" spectra in a scramjet combustor in the T4 Stalker tube at the University of Queensland, and Ceruzzi *et al.* [138] used two-point FLDI to characterize velocity profiles in a vitiated-heated scramjet combustor in the University of Maryland's (UMD) propulsion research lab. Figure 34 shows a photo of the set-up at UMD. Notably, the entire set-up including laser, custom Wollaston prisms, and high-speed data acquisition system cost less than $10k (USD 2023) which illustrates the relative accessibility of FLDI compared to more expensive laser diagnostics. The measured velocity

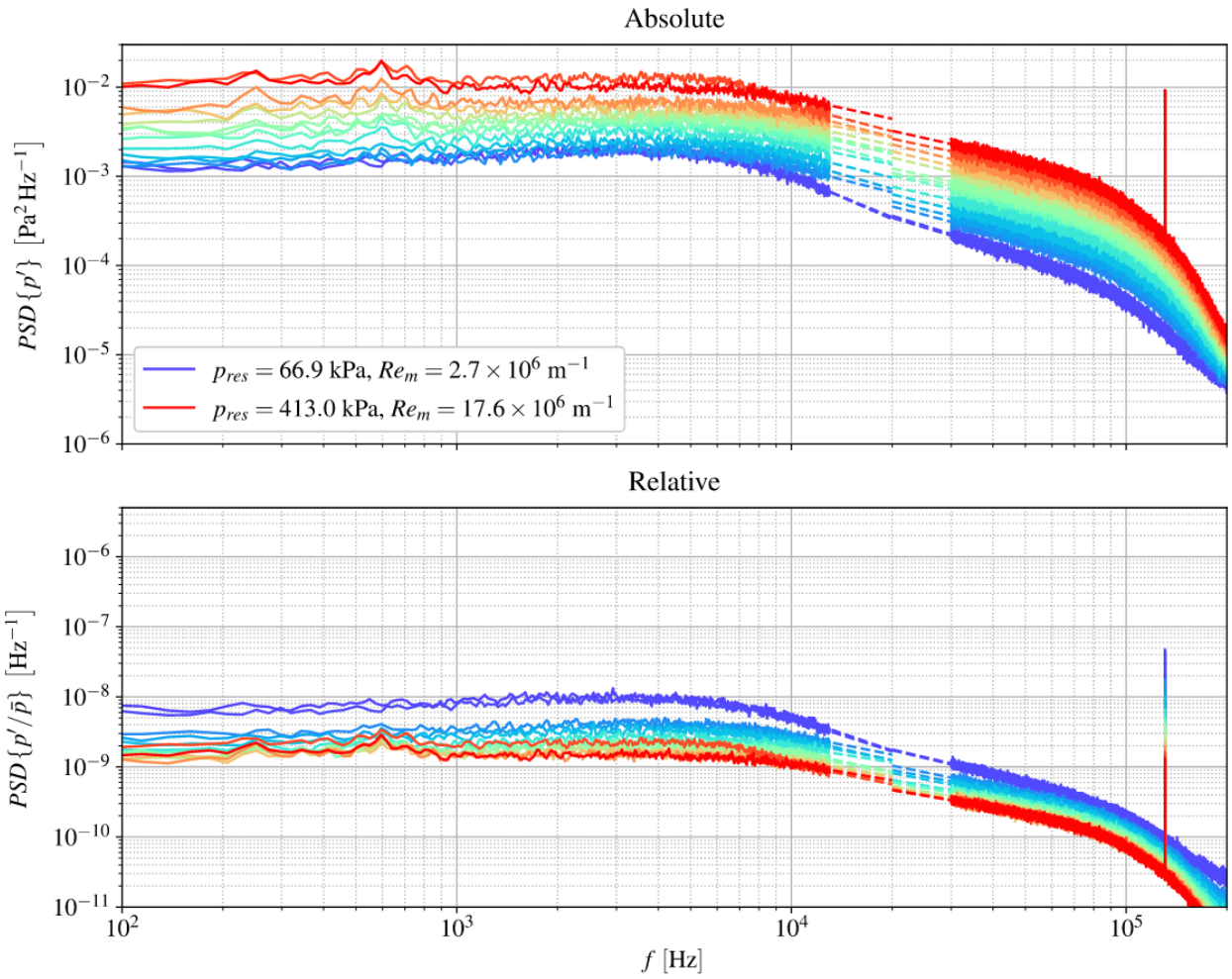

Fig. 32 Comparison of converted FLDI (> 30 kHz) and pitot (< 15 kHz) spectra for all conditions within VKF Wind Tunnel D Run 186: M_∞ = 4. Dashed lines indicate power-law extrapolations beyond the useful bandwidth of each instrument, from Lawson *et al.* [105].

profiles are plotted in Fig. 35. Ceruzzi *et al.* [138] employed a form of high-pass filtering to estimate the velocities for disturbances with wavenumbers greater than 13 m^{-1}. These velocities are in good agreement with "deduced velocities" estimated via other methods, which provides some validation of the usefulness of FLDI in these types of reacting flows.

Another example of FLDI applied to a high-temperature flow with thermochemistry is from Dean *et al.* [87], who investigated turbulent spectra pre- and post-normal-shock in the Hypervelocity Expansion Tunnel (HXT) at Texas A&M University. The setup is an example of how a combined schlieren-FLDI configuration (set-up shown in Fig. 43 and discussed further in Section VII.A) can be used to locate the FLDI probe with respect to an important flow feature (e.g., the shock). As the authors note, FLDI signals are sensitive to both density and chemical composition which hampers the ability to deduce density-based turbulence intensities in reacting and high-temperature flows.

VI. Computational and Quantitative FLDI

Computational models of LDI and FLDI have been implemented to improve understanding of these diagnostics since the late 2010s. In the mid 2010s, Bisek and Brown [139] numerically replicated LDI measurements taken of the corner flow of a rectangular Mach 2.2 flow. The first example of FLDI modeling was made in 2013 by Parziale [19], who averaged and scaled computed eigenfunctions of the hypersonic second-mode instability about an axisymmetric model taking into account the spatial averaging from the FLDI beams. A more detailed computational FLDI model was

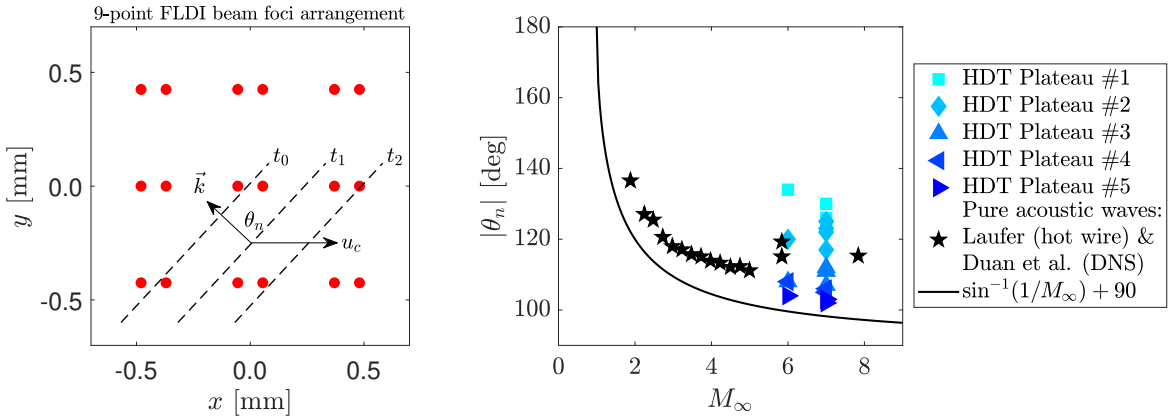

Fig. 33 Freestream wave inclination angles in the University of Oxford's High Density Tunnel (HDT) measured using cross-correlation between multi-point FLDI probes, from Ceruzzi *et al.* [113]. The flat-plate data from Laufer [136] and Duan *et al.* [137] have been adjusted by 7 degrees to account for the inclination angle of the nozzle where the waves in the HDT test section are expected to originate

developed when Fulghum [24] utilized transfer functions to analyze the sensitivity of the technique. Settles and Fulghum [25] later used this methodology to conduct a parameter study to determine the effect of different FLDI characteristics (such as beam separation or field lens focal length) on the overall performance of the FLDI. An even more sophisticated model of FLDI was developed by Schmidt and Shepherd [96] around the same time. They used a ray tracing method that traversed a predetermined density field to yield a computed FLDI measurement. This method agreed well with laminar jet experiments as well as analytical transfer function solutions given the same sinusoidal flow field. It was later extended independently by Bathel *et al.* [48], Lawson and Austin [108], Benitez *et al.* [106], and Camillo and Wagner [93] to use CFD-computed flow fields in the simulations. Since then, several additional numerical FLDI studies have been conducted to better comprehend the benefits and limitations of the diagnostic [92, 111, 112].

A. Ray Tracing Model

Schmidt and Shepherd [96] developed the first optics-based model of FLDI performance, which was tested against analytic solutions (the transfer functions) as well as experiments (the validation experiments are discussed in Section III.D). The computational FLDI model utilized a ray tracing methodology to estimate the FLDI signal at the photodiode. The comprehensive numerical implementation details can be found in several works [96, 97, 111]. The total phase shift induced by a specific refractive index field, expressed in Eq. 11, can be reformulated and simplified to:

$$\Delta\phi = \frac{2K\pi}{\lambda_0} \int_z \left[\iint_D \Big(\rho(x + \Delta x/2, y, z) - \rho(x - \Delta x/2, y, z) \Big) I_0(r, \theta) dr d\theta \right] dz \tag{31}$$

This equation can be computationally solved for any given density field, $\rho(\vec{x})$. In cases of time-dependent density fields, the equation can be iterated for each time step to obtain a time-resolved phase shift series, $\Delta\phi(t)$. Equation 31 forms the foundation for a majority of computational FLDI techniques discussed in the literature.

The FLDI beams are generally discretized across both the profile plane and the optical axis. Each beam profile is defined by hundreds to thousands of points, usually split evenly in angle and clustered around the centroid in radius (see Fig. 36). Each of the two beams of the FLDI has the same grid along their own path through the flow, so that the density difference is found for each point along the grid. These differences are integrated per Eq. 31 to determine the computed FLDI signal.

B. Transfer Functions

Transfer functions, which are useful for validation of computational studies, are derived from the ray tracing model, i.e., from Eq. 11 or Eq. 31. As discussed in Section III.B, there are two key aspects of an FLDI that distinguish it from

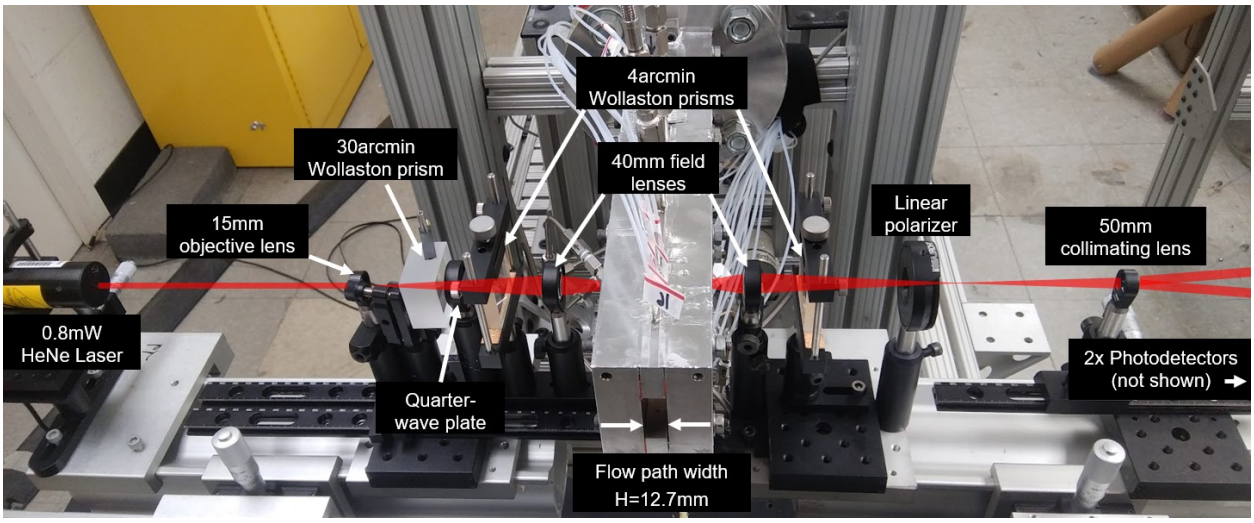

Fig. 34 Photo of two-point FLDI probing a scramjet combustor at UMD's propulsion research lab [138].

an idealized, infinitesimally thin line measurement system: the finite separation between the two beams and the finite dimensions of the beam profiles [75, 96, 99, 101, 111]. These two features can be isolated to look at the effect of each independently when deriving a transfer function for an FLDI system. The definitions for the beam separation and profile effects for a 2D sinusoidal signal centered at the foci propagating in the x direction with uniform magnitude along the optical axis are found by evaluating the integral in Eq. 21, where $n'(z) = 1$ from $-L_z$ to $+L_z$ and zero elsewhere. The magnitude of the resulting transfer functions are:

$$H_{\Delta x} = \left| \sin\left(\frac{\pi \Delta x}{\lambda_x}\right) \right| \tag{32}$$

$$H_w = \frac{w_0 \lambda_x \sqrt{2\pi}}{2 L_z \lambda_0} \exp\left(-\frac{w_0^2 \pi^2}{2\lambda_x^2}\right) \mathrm{erf}\left(\frac{L_z \lambda_0 \sqrt{2}}{2 w_0 \lambda_x}\right) \tag{33}$$

where λ_x is the wavelength of the disturbance, λ_0 is the wavelength of the laser, and L_z is the half-width (along the optical axis) of the sinusoidal signal. To convert to frequency-space from wavelength-space, the convective velocity (u_c) can be used to transform the disturbance wavelength to signal frequency ($f = u_c/\lambda_x$). These equations have been derived by various methods in previously-published literature [24, 73, 96, 99, 101]. In addition to these two equations, some FLDI sensitivity studies have gone further by introducing a transfer function for the flow field as well, such as when a narrow-diameter turbulent jet is probed [75]. Others have extended these functions by moving to higher-dimensional sinusoidal signals with arbitrary orientations [99, 101].

To capture the effects of both aspects of the non-ideal FLDI, the transfer functions can be multiplied, as in Eq. 34.

$$H = H_{\Delta x} H_w \tag{34}$$

The contribution from each transfer function and the overall transfer function, H, are displayed in Figure 37. From this plot, it can be seen that the finite spacing between the beams, the effect of which is captured by $H_{\Delta x}$, leads to both a low-frequency roll-off as well as narrow-band signal drops at discrete frequencies. The wavelengths of these local minima are defined by Eq. 35, while the local maxima are defined by Eq. 36.

$$\underset{\lambda_s}{\mathrm{argmin}}\, H_{\Delta x} = \left\{ \frac{\Delta x}{n} : n \in \mathbb{Z}^+ \right\} \tag{35}$$

$$\underset{\lambda_s}{\mathrm{argmax}}\, H_{\Delta x} = \left\{ \frac{2\Delta x}{2n-1} : n \in \mathbb{Z}^+ \right\} \tag{36}$$

These outcomes are logical, when imagining two points along a sinusoidal curve, as is the case here given the sinusoidal signal assumption. The finite beam profile size, with effects captured by H_w, leads to a roll-off of the higher

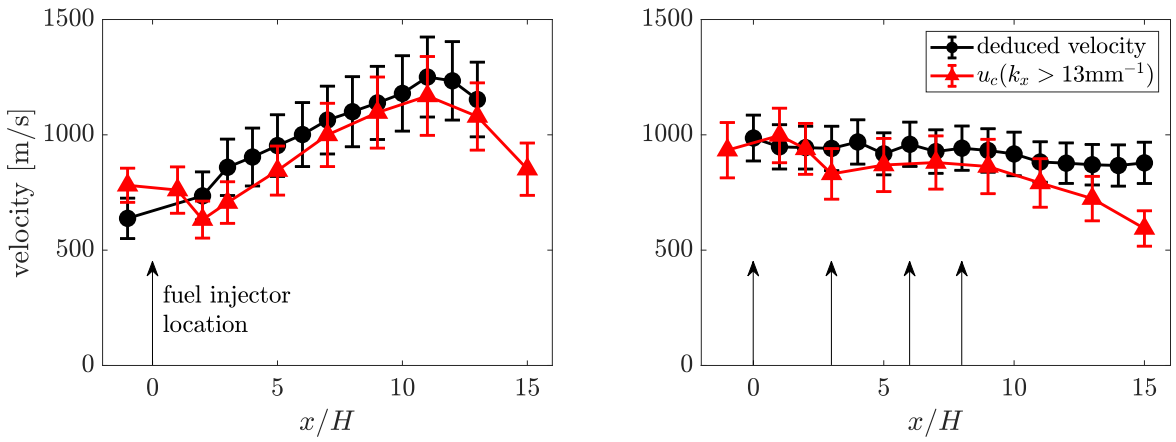

(a) Single Injection **(b) Distributed Injection**

Fig. 35 Two-point FLDI axial velocity profiles, u_c, in a scramjet combustor [138]. "Deduced velocity" is found from a combination of pressure measurements, chemiluminescence, and quasi-1D flow analysis.

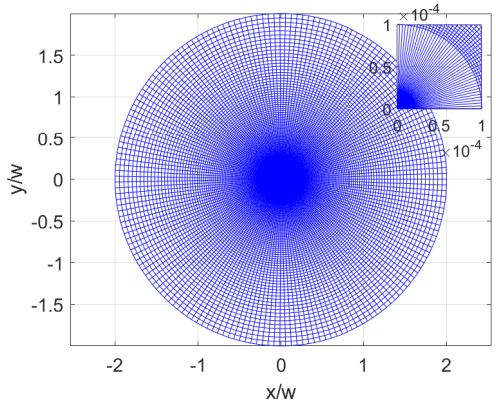

Fig. 36 Example polar coordinate FLDI beam profile grid with 180 azimuthally-distributed points and 363 radially-distributed points. Used with permission from Benitez.

frequencies. This property essentially acts as a low-pass filter. By combining both effects, signal suppression can be seen at both lower and higher frequencies, along with signal drop-outs at submultiples of the beam spacing. In practice, experimenters should chose a sufficiently small beam spacing such that these signal drop-outs are not encountered in their bandwidth of interest. Evidence of these drop-outs is seen in Fig. 16 of Maszkiewicz *et al.* [89], for example.

Note that there is a discrepancy of definitions of $H_{\Delta x}$ between different references. Fulghum [24], Schmidt and Shepherd [96], and Hameed and Parziale [99] utilize a sinc() function for this term, while Ceruzzi *et al.* [73, 101, 111] and Benitez *et al.* [112] use a sin() function. This difference is not an error between sources but instead a difference in definitions. It stems from the former authors defining the transfer function as $H = \frac{\max|\frac{\Delta\Phi}{\Delta x}|}{\frac{d\Phi}{dx}x=0}$, which is a ratio between *derivatives*, and the latter authors who use the transfer functions to *"un-do" the differentiation* performed by the instrument in order to recover a scalar quantity. By converting from a derivative using the derivative property of the Fourier transform ($\mathcal{F}\left\{\frac{\partial f}{\partial x}\right\} = ik\mathcal{F}\{f\}$), an extra k is introduced, resulting in the sinc() function. Lawson and Austin [102] provide further details on the equivalency between the various transfer function methods.

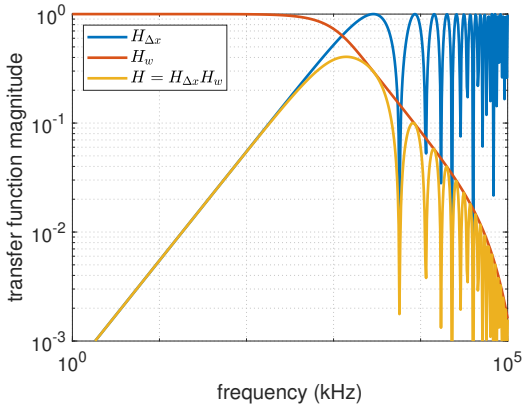

Fig. 37 Example FLDI transfer functions with $\Delta x = 150$ μm, $w_0 = 5$ μm, $\lambda_0 = 633$ nm, and $u_c = 860$ m/s. Used with permission from Benitez.

C. Computational FLDI Applications

Without underlying assumptions of the base flow field, the optical model allows for FLDI simulations of more complex and realistic situations. Independent computational FLDI models have been coded by different researchers and applied to a variety of flow fields to better understand the parameters affecting the performance of the diagnostic.

Schmidt and Shepherd [96] developed the first optics-based FLDI model and applied it to analytic approximations of several different flow fields. Sinusoidal waves of different spans were compared to analytical transfer functions to determine how well the optics-based simulation captured the FLDI effects of finite beam separation and beam width. They found excellent agreement between the transfer function response and the output of the higher-fidelity simulation. A laminar jet, and a second (Mack) mode wave packet were also tested. The second-mode instability is a common hypersonic boundary-layer instability for slender geometries at 0° angle of attack. It has peak frequencies generally in hundreds of kHz, but can extend up to the MHz range. FLDI is one of a small subset of measurement techniques that can capture such high frequencies. Utilizing their ray tracing FLDI computational methodology, Schmidt and Shepherd found that it was possible to obtain quantitative measurements from FLDI of density change between the two beams, by carefully selecting a scaling factor that acts as an integration length and avoiding wavenumbers where the signal is filtered.

Schmidt and Shepherd's method of using only analytical flow fields was extended by Bathel *et al.* [48] and Lawson and Austin [108] to use CFD or experimental flow field data. Bathel *et al.* compared two-point and line FLDI measurements of an expanding shock wave from a laser-induced spark breakdown with the ray tracing FLDI method, which used CFD simulations of the flow field. Lawson and Austin [108] utilized a computational FLDI model to study the diagnostic response to a complex shock-dominated flow [108]. They applied the ray tracing FLDI method to an analytically-defined shock flow, producing quantitative results that agreed well with experiments. They then extended their validation study to look at the FLDI response to multiple shock reflections, utilizing a coupled CFD code to simulate this more-complex flow. Their results, re-produced in Fig. 38, showed the benefit of using higher-fidelity data (via CFD or experiments) to quantify FLDI with the optics-based code.

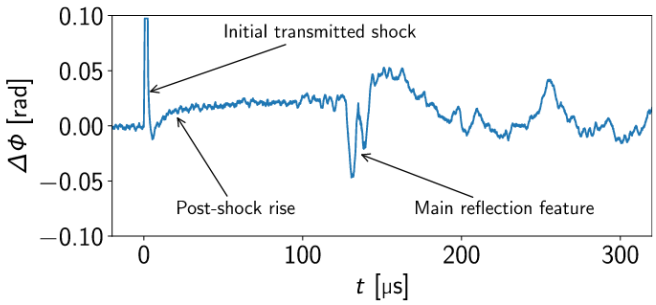

(a) Experimental FLDI signal.

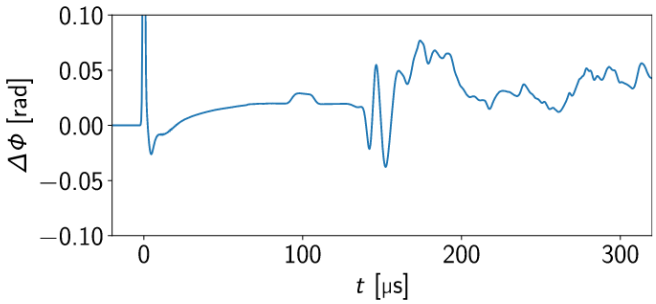

(b) Simulated FLDI signal.

Fig. 38 Comparison between experimental data and a coupled AMROC/FLDI simulation of the shock reflection flow-field in HET, from Lawson and Austin [108]. Used with permission from IOP Publishing Ltd.

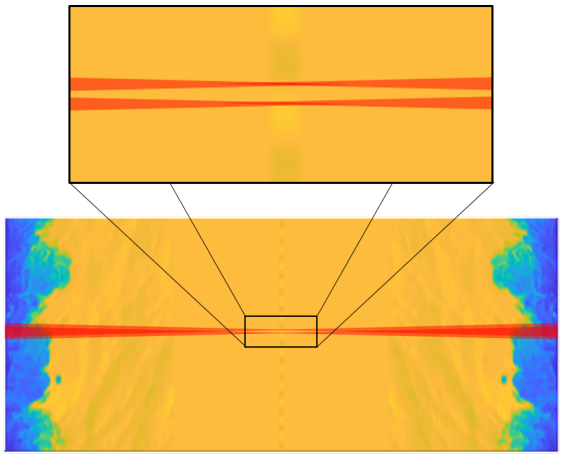

Fig. 39 Computational setup for estimating the effects of hypersonic turbulent boundary layers along a wind tunnel on a centerline measurement. Used with permission from Benitez.

Benitez *et al.* [106] simulated an FLDI response to a high-fidelity tunnel-wall turbulent boundary layer (Fig. 40) to understand how well the diagnostic suppresses such signals away from a signal of interest. By running a ray tracing FLDI simulation through a flow field that included the DNS-created turbulent tunnel-wall boundary layers separated by the diameter of the actual tunnel, they found that the FLDI-simulated freestream measurement comes to roughly 4 to 5 times the true freestream fluctuations, although this variation was not as pronounced at higher frequencies. Benitez *et al*.

also added a small (0.05%-5% of the mean density) sinusoidal signal along the tunnel centerline position; this signal was successfully measured over the noise of the boundary layers in most cases (which have an RMS of 12% of the mean density). Therefore, while FLDI does not completely suppress tunnel-wall boundary-layer signals, it suppresses them enough to allow for clear measurements of centerline signals to be made.

Camillo and Wagner [93] computed FLDI responses to circular symmetry flow fields for the purpose of reconstructing pressure waveforms. They conducted a parametric study of a weak blast wave emanating from an electric spark plug, studying both experimental and computational FLDI responses with differing beam separation distances and probe locations relative to the wave source. Provided that the beam separation is kept below 20% of the flowfield characteristic length, peak pressure values can be accurately measured (within 10% of predicted values).

Lawson *et al.* [104] and Benitez *et al.* [111] used laminar and turbulent jets, respectively, to help understand how FLDI parameters impacted the sensitivity of the diagnostic. Lawson *et al.* [104] conducted both a thorough experiment probing the FLDI sensitivity region with a laminar jet as well as simulating the results using the experimental data to generate an index of refraction field to input to the FLDI simulation. Benitez *et al.* [111] utilized an LES turbulent jet to probe a simulated FLDI and compared the response to a prior experiment [49]. They confirmed findings that the FLDI response varied with signal wavelength, with a wavelength of two times the beam separation maximizing the measurement amplitude. However, they showed the frequency, when independent of wavelength, had no impact on the FLDI response as long as it remained below the photodetector low-pass filter cutoff. For FLDI parameters, a smaller beam spacing and larger beam profile diameter away from the foci tended to contribute to a shorter FLDI sensitivity length.

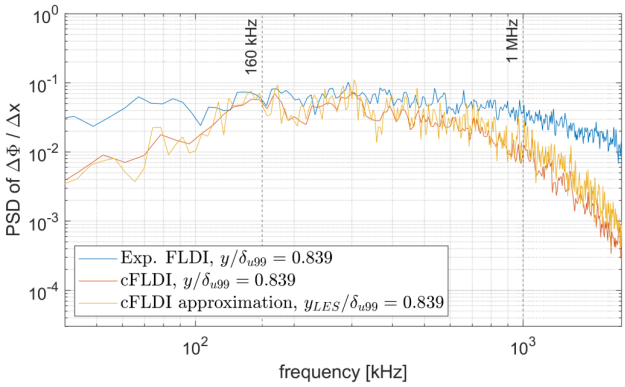

Fig. 40 PSDs comparing computed FLDI signal with experimental data for a hypersonic turbulent boundary layer. Used with permission from author.

Camillo *et al.* [92] conducted a thorough numerical FLDI analysis of a hypersonic turbulent boundary layer along a cone and provided excellent comparisons to experimental data. They took experimental boundary-layer measurements and conducted a high-fidelity DNS of a 7° half-angle cone at $M_\infty = 7.4$ and $Re_\infty = 4.2 \times 10^6$ m^{-1}. By simulating the FLDI signal through the DNS results, they were able to show excellent agreement between the experimental and computational density fluctuations for frequencies between 160 kHz and 1 MHz.

Benitez *et al.* [112] also computed FLDI responses to a turbulent hypersonic boundary layer along a cone (a Mach 8 7° cone previously used in an experiment at Sandia HWT-8). This work focused on understanding the effects of small-scale structures on FLDI performance; smaller flow structures were found to significantly impact FLDI signal roll-off and RMS amplitudes. This work also included a parametric study that showed that circular, Gaussian beams with smaller widths improve performance, and beam-splitting direction could be used to help measure turbulence isotropy scales. Additionally, a direct comparison between ray tracing FLDI codes independently developed in Camillo and Wagner [93] and Benitez *et al.* [106] were compared with excellent agreement despite differences in grids and pre-processing.

Computational studies on DNS of individual hypersonic boundary-layer waves have also been conducted for the oblique first-mode instability [140] and the planar second-mode instability [141]. For oblique waves, it was found that the FLDI measurement underestimated the true density fluctuation amplitudes at the foci, while for planar waves it overestimated them. These small but detailed DNS density fields were also used to better understand the effect of modifications in experimental setups [140] and compare the different quantitative methods of converting beam phase

change to density fluctuations [141]. The second-mode flow field was also computationally probed with a two-point FLDI setup, allowing for analysis of how accurate the diagnostic is at measuring convection velocity of a disturbance.

VII. Specialized FLDI Configurations

A number of specialized FLDI setups that provide some enhanced capability or integrate additional diagnostics have been developed. These include integrating simultaneous schlieren imaging capabilities (Section VII.A), modifying beams for propagation through curved windows (Section VII.B), utilizing multiple laser wavelengths to distribute beams along the beam axis (Section VII.C), using a Mach-Zehnder interferometer either as a separate validation or as an integral part of the FLDI system (Section VII.D), using a tunable laser diode to measure gas absorption in addition to the interference signal (Section VII.E), and other miscellaneous configurations (Section VII.F).

A. Combined FLDI and Schlieren Imaging

Flow field visualization through the use of schlieren imaging has been a ubiquitous test technique, used at nearly every wind tunnel facility that possesses the required optical access. Although methods of increasing the spatial resolution of the FLDI technique have been ongoing (see Section IV), it remains a low spatial resolution measurement compared with schlieren imaging, and many test campaigns utilize both FLDI and schlieren measurements to supplement each other. It is difficult to accommodate both measurements at the same time for the same flow of interest, due to the physical footprint of both systems. Bathel *et al.* demonstrated an approach to integrate conventional schlieren imaging into an FLDI system, shown schematically in Fig. 41a [28]. This setup uses dichroic mirrors to couple the schlieren pulsed LED light onto the FLDI optical axis, and utilizes the existing field lenses of the FLDI system to collimate and refocus the light, akin to a typical lens-based conventional schlieren system. Counter-propagation of the light from the FLDI and schlieren systems ensured the highest quality data and images, unaffected by the other measurement technique. A similar colinear technique that couples a self-aligned focusing schlieren (SAFS) system into the FLDI instrument was demonstrated by Weisberger and Bathel [52], shown schematically in Fig. 41b, where the SAFS system light travels in both directions along the optical axis. Multiple experiments in Ref. [52] were performed to ensure that the addition of the dichroic mirrors had no influence on the FLDI signal, that the angle of the dichroic mirrors had no influence on the FLDI signal, that the direction of the SAFS coupling into the FLDI system had no influence on the FLDI signal, and that the placement of the dichroic mirrors relative to the Wollaston prisms had no influence on either system. By using a focusing schlieren system instead of a conventional schlieren system, the two measurements can be accurately compared, since both exhibit a filtering effect of flow structures away from the intended plane of focus.

The conventional schlieren and FLDI system from Fig. 41a was used to make measurements of the flow around a pitot probe in a Mach 6 wind tunnel, an image of which can be seen in Fig. 42a, where the FLDI measurement point is identified near the center of the field-of-view. A large intensity spike in the FLDI voltage data was determined to be from a particle impact on the pitot probe face that disturbed the bow shock, a flow feature that would otherwise not have been able to be identified without the combined imaging capability. An image of the acoustic radiation field from a compressed air jet using the FLDI/SAFS system of Fig. 41b is shown in Fig. 42b, with the FLDI measurement point shown schematically in red. Using a spectral processing analysis, the dominant acoustic frequency of the jet could be compared between the FLDI and SAFS.

A configuration similar to Ref. [28] was used in Refs. [80, 91, 142], where the dichroic mirrors were placed between the field lens and Wollaston prism, and the light propagation for both FLDI and schlieren systems was in the same direction. This allowed a small portion of the FLDI light to be incident on the schlieren image for precise placement, but care must be taken not to burn the camera sensor with the laser light, and also to avoid having the schlieren light incident on the FLDI photodiodes, especially if using intense pulsed light. Options for mitigating this effect include optical filtering in front of the photodiodes and timing the FLDI and schlieren acquisition in offset periods. Identifying the position of the FLDI beams in Ref. [28] was accomplished after a run, where a diffuse target was placed at the FLDI beam focus and imaged by the schlieren camera. Further details of the differences between these system can be found in Ref. [52].

An alternative approach to combined FLDI and schlieren imaging appears in the work by Dean *et al.* [87], which is illustrated schematically and with pictures in Fig. 43a. The FLDI was arranged in a Z-type configuration like the mirror-based schlieren setup, and dichroic mirrors were used to couple the FLDI light into and out of the schlieren beam path, enabling simultaneous FLDI measurements and schlieren imaging of the same region. This approach, coupling

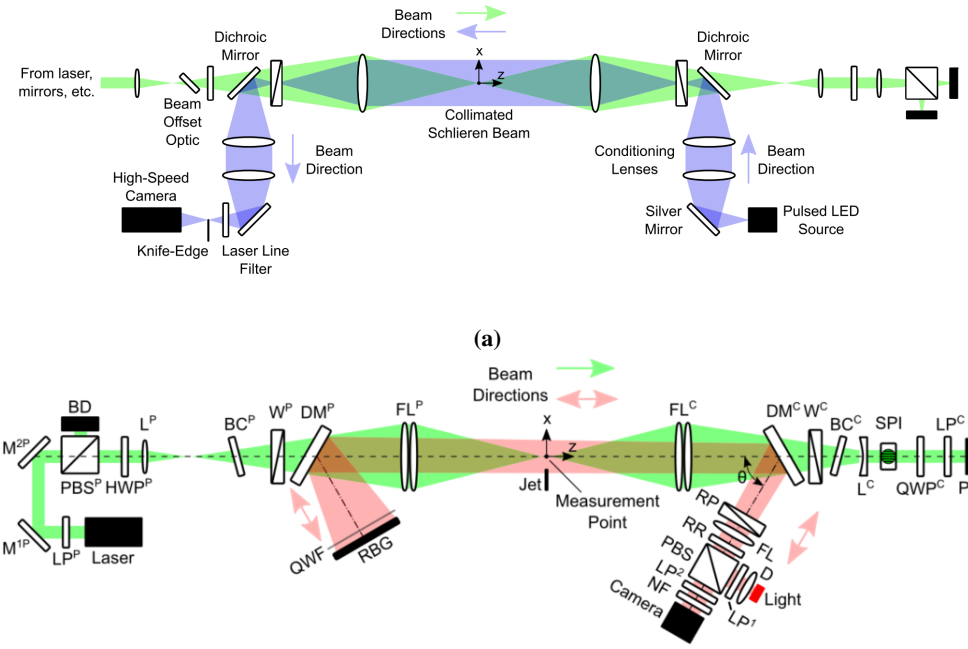

Fig. 41 Schematics of the (a) colinear FLDI and conventional schlieren from Bathel *et al.* [28], and the (b) colinear FLDI and self-aligned focusing schlieren from Weisberger and Bathel [52]. Used with permission from NASA.

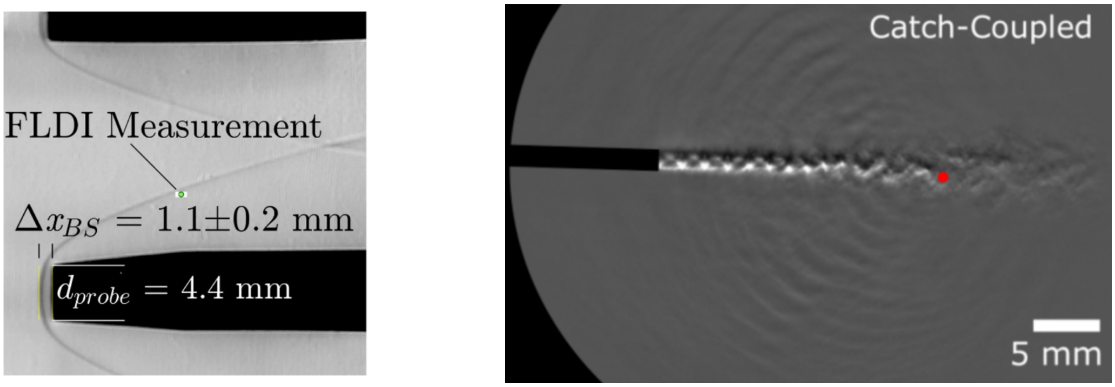

(a) **(b)**

Fig. 42 (a) An image from Bathel *et al.* [28] showing a conventional schlieren image acquired through the FLDI system lenses per the setup in Fig. 41a. The image was taken in Mach 6 flow conditions in a NASA facility. (b) Image from Weisberger and Bathel [52] of self-aligned focusing schlieren image of a compressed air jet with FLDI measurement point identified with red dot. Used with permission from NASA.

the FLDI system onto the optical axis of the schlieren system instead of the other way around, allows the typical large schlieren mirrors to be used to obtain a larger field-of-view than would be obtained using FLDI lenses, which are generally only a few inches in diameter. In a later form of the same experiment, Dean *et al.* [87] arranged the FLDI light source to allow for viewing of the points on the schlieren imaging camera, as shown in Fig. 43b. The viewing of the points could be controlled by adding or removing an appropriate optical filter in front of the camera, with imaging of the FLDI points done prior to the run and added via image combination in post-processing.

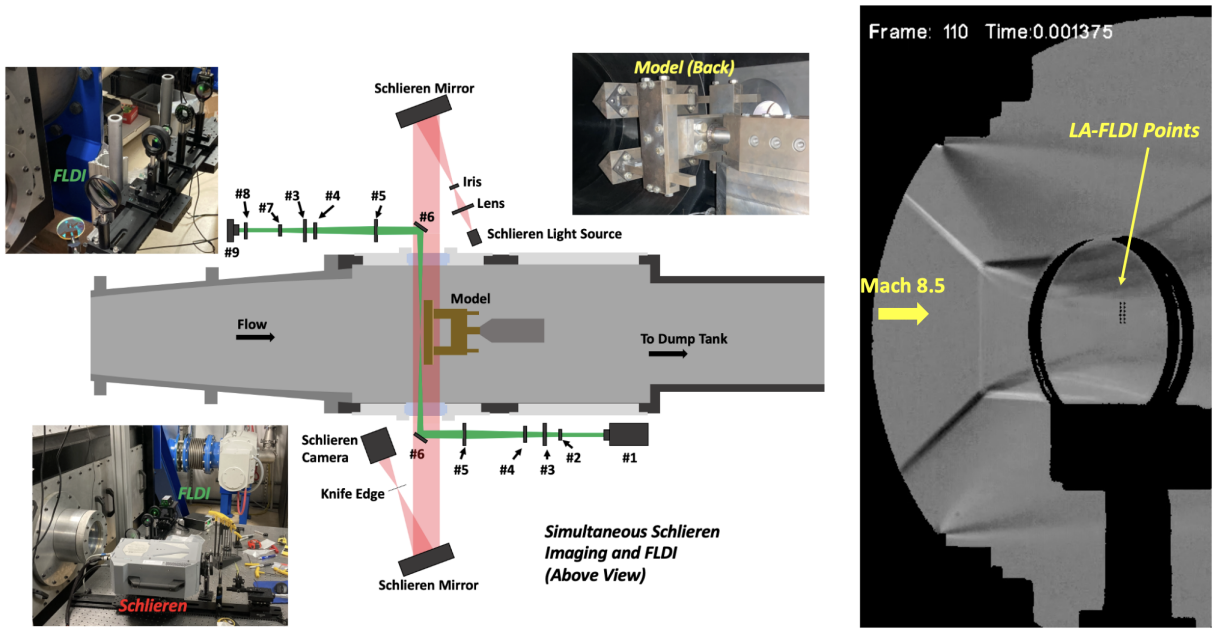

(a) **(b)**

Fig. 43 (a) An illustration from Dean *et al.* [87] showing a Z-type setup of FLDI and mirror-based schlieren imaging, using conventional schlieren mirrors rather than FLDI lenses. (b) An image taken by Dean *et al.* [87] in later experiments showing several FLDI beams in a schlieren image, which appear as dark spots due to post-processing. Used with permission from author.

B. FLDI through Curved Windows

Most wind tunnel facilities have flat, schlieren-grade windows to provide optical access to the test section. These windows pose little problem for the typical FLDI system aside from shifting the beam focus farther from the field lens depending on the thickness of the window, which can be accounted for in the system alignment. Smeets noted that not every facility would have parallel windows, with some test chambers having inclined windows (as shown in Fig. 5 of Ref. [6]). As long as this inclined windows are flat, they too pose minimal problems for FLDI systems. However, some axisymmetric wind tunnels have matched contoured windows that allow for optical access for non-intrusive measurement techniques. These contoured windows act similar to lenses and can present significant difficulty in utilization of FLDI for flow measurements. This problem was first discussed and addressed by Benitez *et al.* [49] when attempting to apply FLDI to the Boeing/AFOSR Mach-6 Quiet Tunnel (BAM6QT) at Purdue University, with the contoured windows presenting two effects that must be considered. First, the window's lensing effect can change the focal point of the FLDI system and degrade sensitivity and response from the intended probe region. Second, but related, is the lensing effect displacing the beam off the intended optical axis via the typical refractive properties of lenses, which is an effect that depends on the incident position of the beam on the window, and the relative curvature of the window faces. These two effects are summarized schematically in Fig. 44, where a Gaussian-profile beam is refracted with a reshaped profile after it passes through the lower portion of a contoured window.

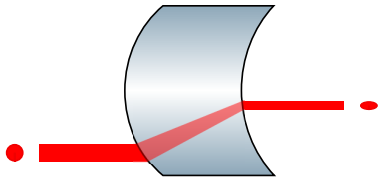

Fig. 44 Illustration of two effects a contoured window has on a circular beam. The beam is displaced in relative position and its profile is no longer Gaussian after passing through the contoured window, which acts like a cylindrical lens that transforms the circular beam into an elliptical beam.

To overcome these complications, a pair of cylindrical lenses, rather than a singular spherical lens, can be used as the field lens for the pitching side of the FLDI. Benitez *et al.* [49] implemented such a setup by utilizing the ray-tracing software Zemax™ to first simulate the beams as they traversed through the FLDI optics and the contoured window. Figure 45 shows a screenshot of the Zemax™ simulation setup, focused on the region near the pitch-side window. By digitally selecting different lenses and shifting their relative positions, they were able to create a configuration that focused the FLDI beams at the centerline of the tunnel with approximately circular foci. Since the windows were nearly cylindrical, shifting the horizontally-focused cylindrical lens (L2) in the vertical direction (h_1) resulted in a vertical shift of the foci by a different amount (h_2). This distance was calibrated at the FLDI installation to allow for a known vertical traversal of the beams to be made through the boundary layer of a model.

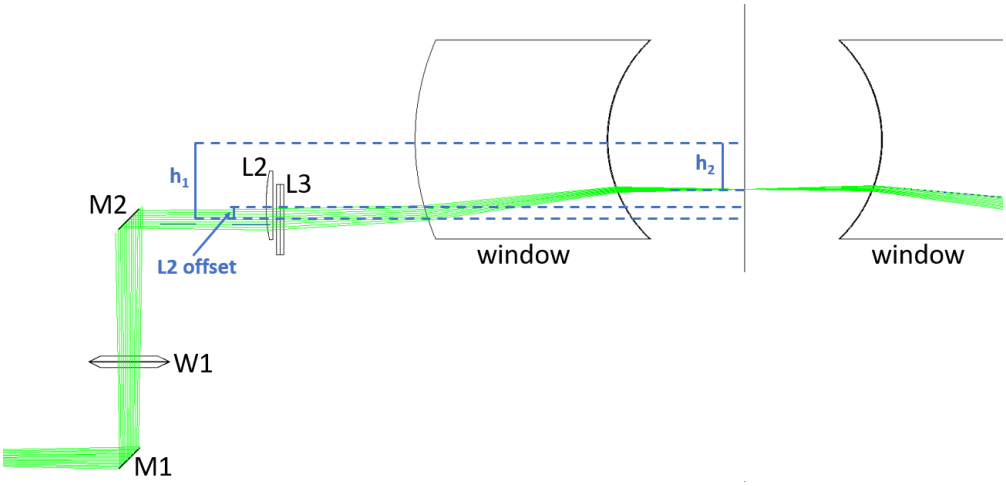

Fig. 45 Simulation of FLDI beams made in Zemax™ to design an optical setup compatible with contoured tunnel windows [49]. Used with permission from author.

Images of the FLDI beam foci are shown in Fig. 46, where the small diameter, tightly focused beams of the traditional FLDI system are shown in Fig. 46a, and the focused beams from the contoured window system are shown in Fig. 46b. While the quality of the beams is degraded from the traditional FLDI system, two separate beams are visible, and extensive testing of the system installed at the BAM6QT was performed and reported in Ref. [49]. Characterization testing included pure sine tone frequency measurements and sensitivity response to a jet traversing along the optical axis of the system, with comparisons to the traditional FLDI system. Measurements were then performed using a seven-degree straight cone model with a sharp nose tip, making measurements of second mode disturbances in both conventional-noise conditions and under quiet-flow conditions.

C. Chromatic FLDI

As discussed in Section IV, multi-point FLDI techniques enable additional measurements of dynamics through correlation analyses. In that discussion, the multi-point FLDI configurations resulted in beams that were distributed to different points in the same approximate focal plane, spaced equidistant between the pitch and catch sides of the FLDI

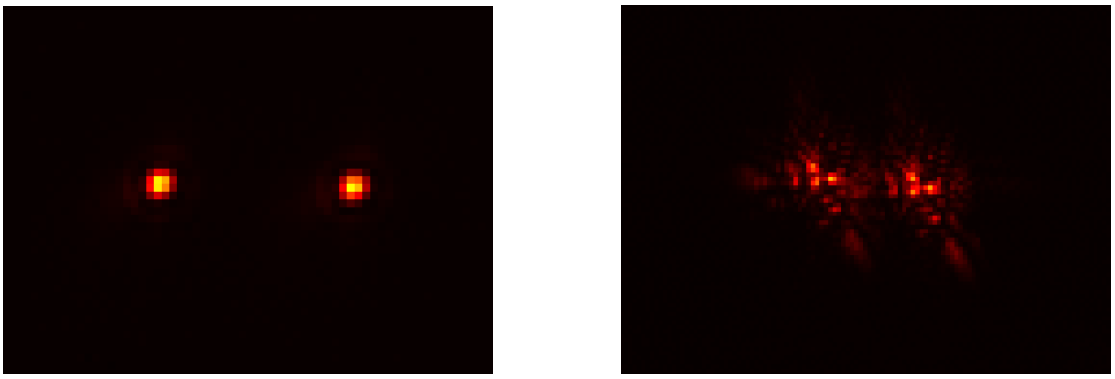

(a) (b)

Fig. 46 FLDI beam foci for the (a) traditional setup (without any windows) and (b) the BAM6QT setup (with the Plexiglas contoured windows). Used with permission from author.

system, at the same plane along the optical axis. In order to achieve spatial separation along the optical axis, Webber *et al.* [71] developed an FLDI system that uses two wavelengths of light and takes advantage of the different focusing distances of a lens that is not designed to be achromatic (with further testing performed in Ref. [70]). That is, for a simple lens, the wavelength dependence of the index of refraction $n(\lambda)$, the chromatic dispersion, results in a focal length that is wavelength-dependent. Using the lens maker's equation for thin lenses, the following equation that models this effect:

$$f(\lambda) = f_{\mathrm{D}} \frac{n_{\mathrm{D}} - 1}{n(\lambda) - 1} \tag{37}$$

This equation relates the focal length $f(\lambda)$ of a thin lens at wavelength λ to the design focal length f_{D} and index of refraction n_{D}. This equation can be used in matrix optics calculations to predict how one wavelength of light is focused compared to another.

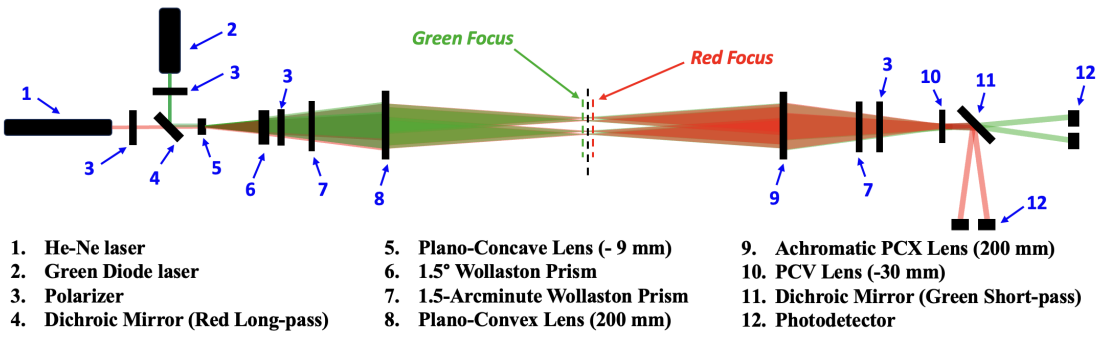

Fig. 47 The optical layout used by Webber *et al.* [71] for a multi-depth FLDI that produces additional points along the beam axis. Used with permission from Optica.

Based on Eq. 37 and using two laser beams of sufficiently different wavelength in the FLDI setup, Webber *et al.* [71] achieved focused beams at two different locations along the optical axis. A schematic of the chromatic FLDI system is shown in Fig. 47, where green (532 nm) and red (632 nm) lasers were used as the different wavelength sources. The two beams were made colinear on the optical axis by the use of a longpass dichroic mirror. A two-point system was constructed by including an additional larger splitting angle Wollaston prism ahead of the typical Wollaston prism (discussed in more detail in Section IV.A). Care must be taken when aligning the catch side of the system, because due to the different focusing points along the optical axis, the catch side field lens (9 in the schematic of Fig. 47) will focus the beams to different positions. This affects the overlapping of the beams at the catch side Wollaston prism. To

mitigate this effect, an achromatic lens was used for the catch side field lens in order to not further shift the focus of the two wavelengths.

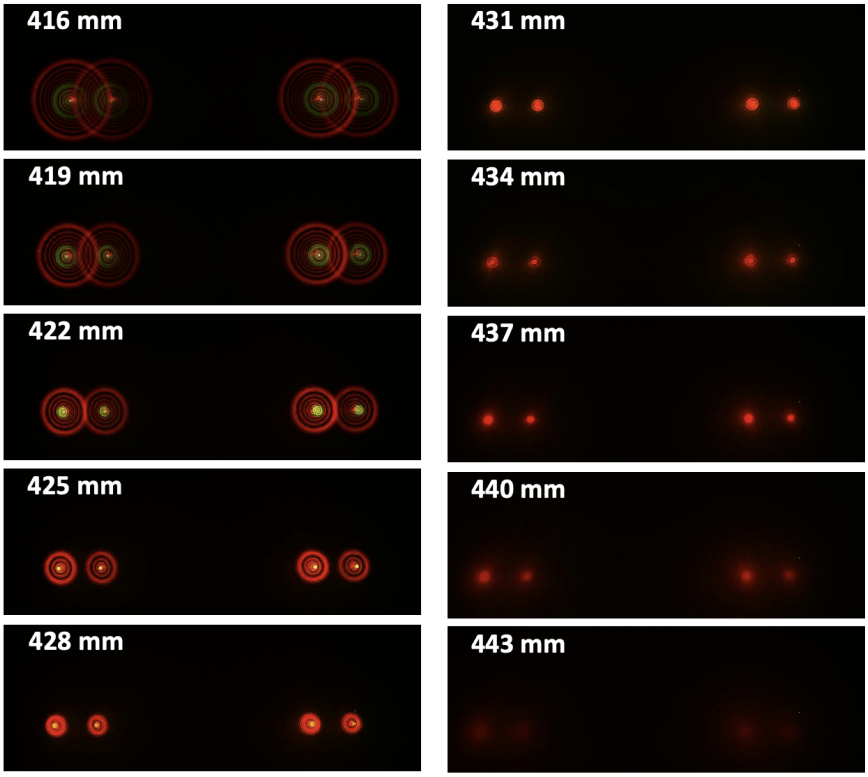

Fig. 48 Image montage showing multiple focal points along the optical axis, with lasers operating at 532 nm (green) and 632 nm (red) [71]. Used with permission from Optica.

Images of the dual wavelength beam focusing at different positions along the optical axis are shown in Fig. 48. At 416 mm, both beams are still focusing down, but have different diameters. As the distance along the optical axis increases, the green beams come to a focus first, and then a short distance later, the red beams come to a focus. The separation distance of the two focusing spots was measured to be approximately 8 ± 1.4 mm, close to the calculated expected value of 7.6 mm. Testing of the system demonstrated that both beams function as an FLDI instrument despite the slight asymmetry in the setup introduced by the focal points on either side of the most optimal location halfway between the field lenses. Demonstrations of the system included measurements in a turbulent jet and the measurement of the velocity of a sound wave produced from a laser-induced spark in air.

This variation of FLDI is still relatively new, but there are important aspects that should be considered. Webber *et al.* [71] point out that despite the spacing of the beams along the axis (approximately 8 mm in their work), the path integrated effects of the FLDI means that the beams will all have similar response to disturbances, except at higher frequencies. Hence, more separation is desirable (perhaps by using increasingly dissimilar wavelengths) or focusing the measurement on disturbances that have very high frequencies. It is also proposed, but not demonstrated, that the chromatic FLDI setup could in theory be used to determine if a disturbance was closer to one focal point or the other along the optical axis if the response of each beam was well-understood; this approach could open up avenues for examining spreading rates in transitional boundary layer flows. Finally, because the Wollaston prisms have slightly different properties at different wavelengths, the impact of these differences on the measurement can be further studied, and using achromatic Wollaston prism systems may be beneficial [143, 144].

D. Mach-Zehnder Configuration

Another common interferometric technique for aerodynamic measurements is a Mach-Zehnder interferometer, where the laser is split into two separate legs, with the beam in one leg passing through the test gas of interest before being recombined with the reference beam. The density changes are measured by finding the phase differences between the reference and measurement legs across the beam profile. Lawson *et al.* used a separate Mach-Zehnder interferometer positioned with its measurement leg orthogonal to the optical axis of an FLDI instrument to make measurements of a laminar jet, with good agreement between the two measurement systems [31, 104]. A non-focusing LDI system was supplemented with a Mach-Zehnder interferometer measurement in Maisto *et al.* [145].

To allow for fine control over the beam splitting angle of an FLDI, Marsh *et al.* implemented a Mach-Zehnder FLDI configuration [94]. This configuration, shown in Figure 25, takes the beam-splitting apparatus from the Mach-Zehnder interferometer and applies it to FLDI. It improves upon the Sanderson prism configurations by removing the uncertainty added from utilizing bending stresses to control the beam separation. This configuration also can be assembled completely using common commercially-available components. Instead of passing through a single birefringent prism, the light is first focused on a 50/50 beam splitting cube, which redirects two equally-intense beams to 45° mirrors located 90° from each other. One of the two beams is passed through a half-wave plate prior to its mirror, making it orthogonally-polarized relative to the other beam. The mirrors redirect the light to recombine at a polarizing beam splitting cube, which reflects one beam and transmits the other, sending both through the field lenses together. The overall beam separation at the FLDI foci is determined by path each beam of light follows prior to the polarizing beam-splitting cube, providing fine control. Further details about the use of this system are provided in Section IV.D.

E. Absorption Laser Differential Interferometry

FLDI measurements are used to make measurements of the small density fluctuations in a flow. Linking these fluctuation measurements to absolute values of density or pressure can done, but typically require assumptions about the flow and/or measurement system, or additional measurements to reduce the amount of unknowns (methods which are outlined earlier in this document). To obtain a direct measurement of the flow properties, such as temperature, pressure, species concentrations, and velocity, absorption spectroscopy can be used, which uses a tunable diode laser to scan through absorption features of a species of interest. Weisberger *et al.* combined an absorption spectroscopy system with an LDI system (A-LDI) to make simultaneous, colinear measurements of both mean flow properties and flow fluctuations [53, 54]. A tunable diode laser with a central wavelength of 760 nm was used in place of the normal fixed-wavelength laser in FLDI systems, which probes the A-band absorption features of molecular oxygen (O_2), making it particularly well-suited for wind tunnel environments that use compressed, dried air as the test gas. The absorption aspect of the system can be operated both as a direct absorption spectroscopy (DAS) measurement for strong absorption signals and wavelength modulation spectroscopy (WMS) for weaker absorption features. The LDI aspect of the system operates in the same manner as normal LDI system.

As with every system, there are benefits and drawbacks that must be taken into account when deciding whether to implement the technique. The decision to use O_2 as the probing species was dictated by the highest concentration test gas in the hypersonic facilities at NASA Langley Research Center. These facilities use dried, compressed air, meaning the typically stronger absorption features of H_2O could not be used, but the mole fraction of O_2 in the flow would always be constant for all tests. Using a visible wavelength tunable diode laser at 760 nm results in easier alignment, and many of the optics used in conventional FLDI system can also be used if their working wavelength range extends out to this wavelength. This includes the silicon photodiodes, which have an increased responsivity at 760 nm in contrast to either 532 nm or 633 nm, and which have high bandwidth and do not require cooling (thermoelectric cooling or cryogenic cooling) unlike many infrared detectors. However, the quarter-wave or half-wave retarders have narrow wavelength operating ranges, and different optics were required for this A-LDI setup to ensure the polarization orientation and phase adjustment through the system. The absorption of O_2 in the A-band is weak compared with absorption features of other species in the near- to mid-infrared, posing a problem for measurements in low density facilities and short path lengths. A multi-pass system may be needed to ensure sufficient absorption signal. While angling the line-of-sight of the laser provides a simple measurement of the flow velocity via the Doppler shift of the absorption features, sufficient optical access is required to be able to angle the beam (a larger angle results in a larger Doppler shift), unless mirrors can be placed inside the plenum of an open jet facility. While the only published works on this method have used a non-focusing LDI system, testing of an A-FLDI system is ongoing in the laboratory with promising results. Finally, it should be noted that a single line-of-sight absorption measurement remains a path-integrated measurement of the

flow, and even including the focusing nature of the FLDI instrument will not affect the path-integrated nature of the absorption system.

F. Miscellaneous Configurations

Depending on the imaging distances, the size (i.e., the length) of a conventional FLDI system can become large. The pitch and catch sides are placed on both sides of a wind tunnel test section, for example, and are aligned orthogonal to the tunnel axis (freestream direction) and windows. To avoid excessive lengths of the pitch and catch sides, mirrors are sometimes used to fold the beam path. For example, in Fig. 4a of Ref. [44], the laser is mounted above the main optical axis of the system, with two mirrors folding the beam path onto the main optical axis. This has the added benefit of providing a beam-centering adjustment when setting up the system. In Fig. 4b of Ref. [44], a right angle prism mirror and two extra mirrors are used to fold the catch-side beam path for each of the two measurement points. This allows the phase adjustment optic (quarter-wave plate), the linear polarizer, the focusing lens, and the photodiode to be positioned back along an axis towards the front of the catch board. The same style of catch-side beam path folding can be seen in Fig. 3 of Ref. [50]. Another example of a system that folds the catch-side beam path (this time by 90°) can be seen in Ref. [35, 88, 121]. Similarly, a dichroic mirror is used in the chromatic FLDI system of Refs. [70, 71] to fold one of the beam paths by 90°. If space is even more limited than the above cases, larger turning mirrors can be used to fold the beam paths by 90^o, located between the wind tunnel windows and the field lens. Pandey *et al.* folded both sides of the system in the same direction [124], while Kerth [29] and Dean *et al.* [87] folded both sides in different directions.

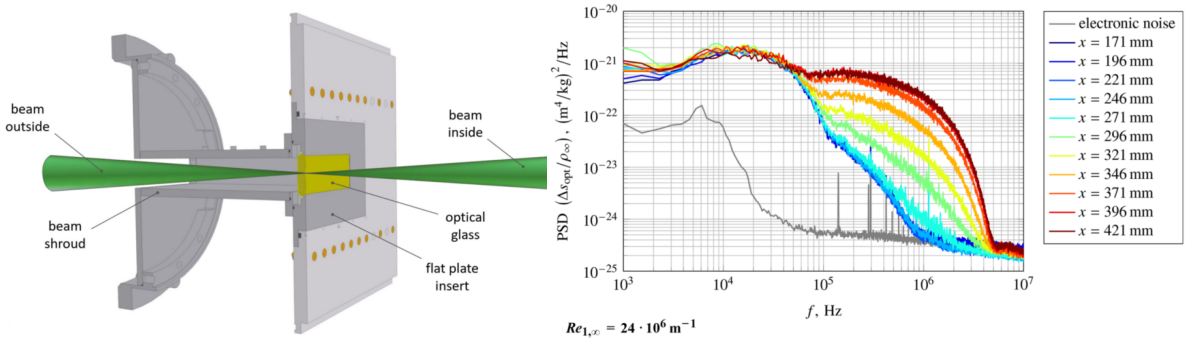

(a) **(b)**

Fig. 49 (a) Schematic of FLDI system projecting through the model sting from Lunte *et al.* [37, 39]. (b) Power spectral density plot for a single Reynolds number of streamwise measurement positions. Used with permission from author.

For all the configurations outlined previously, optical access through two windows on either side of the flowfield of interest is required. However, if optical access is limited, or if a measurement near the surface of a wide flat model is desired without using a cylindrical lens FLDI system, the beam can be projected out through the model itself, as was demonstrated by Maszkiewicz *et al.* [89] and Lunte *et al.* [37, 39]. A schematic of a projection system is shown in Fig. 49a, which shows the focusing beam traveling up through the model sting, coming to a focus just outside a transparent window in the model surface to make measurements in the boundary layer, and then continuing to expand out to the catch side of the system outside the tunnel. Fig. 49b shows resulting power spectral density estimates of the transitional boundary layer at various streamwise positions at a single Reynolds number, showing an increase in the broadband frequency spectrum with increasing distance downstream.

VIII. Perspective on Future Development and Applications

FLDI has become a powerful diagnostic tool for measuring small-scale fluctuations in high-speed flows, particularly in hypersonic and turbulent flow environments. While it has provided the capability for high-speed non-intrusive optical measurements, there remain opportunities for further advancements.

While FLDI already improves spatial resolution compared to traditional LDI by focusing the laser beam to a small point within the flow field, it would be beneficial to improve resolution along the optical axis. The current limitation lies in the fact that FLDI still integrates along the beams to an extent, although with signal amplitude decreasing as the distance from the focus increases. This limitation is particularly problematic in three-dimensional flow fields, such as shock layers, boundary layer interactions, and vortex dynamics, where spanwise fluctuations may not be resolvable. Increasing the beam diameters away from the foci improves this aspect, but more directed research can be conducted to further increase FLDI off-axis signal suppression.

A particular area of improvement that is still an open problem is in the realm of calibration techniques and quantifying measurement uncertainty. Accurate calibration would ensure that FLDI measurements are reproducible and comparable across different experimental setups, while robust uncertainty quantification gives researchers confidence in the reliability of the data.

Current calibration methods are generally based on theoretical models and empirical data, but these can suffer from inaccuracies due to system noise, optical misalignment, and even the three-dimensional properties of the flow. In particular, the spatial averaging across the beam profiles and along the optical axis can have a profound effect on the final signal amplitude. To address these challenges, several improvements can be made:

- **Use of Controlled Reference Flows**: Developing reference flows with well-characterized temperature, pressure, and density profiles would provide a more reliable basis for calibration. These controlled environments could help verify and recalibrate FLDI systems, ensuring accurate measurements across various experimental conditions. This work has been started by the various jet and acoustic emitter tests that have been conducted by FLDI experimentalists to help characterize the technique [75, 104].
- **FLDI Simulation with CFD**: Integrating FLDI simulations with computational fluid dynamics (CFD) data can help identify discrepancies between experimental data and theoretical models. This comparison can be used to refine calibration procedures and provide insight into sources of uncertainty, such as beam misalignment or optical aberrations. Several FLDI simulations have already been run to better understand the diagnostic performance across various flow fields [48, 92, 106, 140, 141], but there is more work to do.
- **Uncertainty Quantification Frameworks**: Establishing a formal uncertainty quantification framework for FLDI is essential for understanding the precision of the measurements. By accounting for sources of error such as signal noise and calibration drift, and using statistical methods like Monte Carlo simulations, researchers can better assess the reliability and confidence intervals of FLDI data.

With these improvements, FLDI can become a more reliable tool for high-precision flow measurements, enabling more reproducible and accurate experimental results.

While FLDI is highly effective at measuring density fluctuations and has been combined with some other techniques, integrating it with additional diagnostics could provide a more complete picture of the flow dynamics. Combining FLDI with other optical methods can provide simultaneous measurements of additional flow properties, such as temperature, pressure, velocity, and turbulence intensity, offering a more comprehensive analysis of complex flow fields. This work has already begun, for example by Weisberger *et al.*'s combination of FLDI with schlieren and spectroscopy [52, 54], but additional applications are possible. For example, combining FLDI with techniques such as laser-induced fluorescence (LIF) or Rayleigh scattering would allow for the simultaneous measurement of both density and temperature fluctuations in the flow. This integration would provide a more complete thermodynamic and dynamic characterization of the flow, essential for understanding the interaction between temperature and density disturbances in high-speed flows.

There are a few areas of application where FLDI is particularly well-suited and currently under-utilized:

- **Receptivity**: This subject was explored in the very early applications of LDI by Salyer *et al.* [16, 17] but has received little attention since then. A combination of the setup from Dean *et al.* [87] and the methods from Ceruzzi *et al.* [113] could be used to investigate the transfer functions of inclined acoustic waves across shocks - this could improve our understanding of how freestream disturbances are modulated by a vehicle's bow shock.
- **Reacting and High-Temperature Flows**: As discussed in Section V.D, there are very few applications of FLDI in reacting flows. The technique could be used as a diagnostic for feedback control in a scramjet, similar to the use of emission spectroscopy by Elkowitz *et al.* [146]. Applications in detonation engine experiments and in studies of ablation, pyrolysis, and plasma jets are possibilities as well.

FLDI is a powerful diagnostic tool that has proven invaluable for measuring high-speed fluctuations in hypersonic flows. However, to fully realize its potential, further advancements can be made in several key areas. Enhancing spatial

resolution, improving calibration and uncertainty quantification, and integrating FLDI with complementary diagnostic techniques will greatly expand its capabilities. These improvements will enable FLDI to provide more accurate, reliable, and comprehensive measurements in high-precision aerodynamic studies, particularly in the challenging environments of hypersonic flows and turbulent boundary layers.

Acknowledgments

The authors wish to acknowledge the many researchers who have worked to develop FLDI and apply it for understanding various fluid dynamic phenomena. We encourage readers to use this document as a resource to help locate those works and cite them for proper recognition when appropriate. Trade names and trademarks are used in this report for identification only. Their usage does not constitute an official endorsement, either expressed or implied, by the National Aeronautics and Space Administration.

References

[1] Smeets, G., and George, A., "Gas-Dynamic Investigations in a Shock Tube using a Highly Sensitive Interferometer," Tech. Rep. 14/71, Institut Franco-Allemand de Recherches de Saint-Louis, 1971. Translation by Andreas R. Goetz, Purdue University, 1996, corrected by G. Smeets.

[2] Seiler, F., and Srulijes, J., "In memoriam of Prof. Dr. rer. nat. Herbert Oertel (1918–2014)," *Shock Waves*, Vol. 26, 2016, pp. 333–336. https://doi.org/10.1007/s00193-016-0642-3.

[3] Oertel, H., "A Differential Interferometer for Measurements in the Hypersonic Shock Tube," Tech. Rep. 17/61, Institute Franco-Allemand de Recherches de Saint-Louis, 1961. Original title: Ein Differentialinterferometer für Messungen im Hyperschallstossrohr.

[4] Smeets, G., "Laser-Interferometer with Large, Focussed Light Bundles for Local Measurements," Tech. Rep. 11/73, Institute Franco-Allemand de Recherches de Saint-Louis, 1973. Original title: Laser-Interferometer mit grossen, fokussierten Lichtbündeln für lokale Messungen.

[5] Smeets, G., "Laser Interferometer for High Sensitivity Measurements on Transient Phase Objects," *IEEE Transactions on Aerospace and Electronic Systems*, Vol. AES-8, No. 2, 1972, pp. 186–190. https://doi.org/10.1109/TAES.1972.309488.

[6] Smeets, G., "Flow Diagnostics by Laser Interferometry," *IEEE Transactions on Aerospace and Electronic Systems*, Vol. AES-13, No. 2, 1977, pp. 82–90. https://doi.org/10.1109/TAES.1977.308441.

[7] Smeets, G., and George, A., "Laser-Differential Interferometer Applications in Gas Dynamics," Tech. Rep. 28/73, Institut Franco-Allemand de Recherches de Saint-Louis, 1973. Translation by Andreas R. Goetz, Purdue University, 1996, corrected by G. Smeets.

[8] Morkovin, M. V., "Critical Evaluation of Transition from Laminar to Turbulent Shear Layers with Emphasis on Hypersonically Traveling Bodies," Tech. Rep. AFFDL-TR-68-149, Research Institute for Advanced Studies, Martin Marietta Corporation, Mar. 1969.

[9] Reshotko, E., "Boundary-Layer Stability and Transition," *Annual Review of Fluid Mechanics*, Vol. 8, 1976, pp. 311–349. https://doi.org/10.1146/annurev.fl.08.010176.001523.

[10] Fedorov, A. V., and Khokhlov, A. P., "Prehistory of Instability in a Hypersonic Boundary Layer," *Theoretical and Computational Fluid Dynamics*, Vol. 14, 2001, pp. 359–375. https://doi.org/10.1007/s001620100038.

[11] Schneider, S. P., "Effects of High-Speed Tunnel Noise on Laminar-Turbulent Transition," *Journal of Spacecraft and Rockets*, Vol. 38, No. 3, 2001, pp. 323–333. https://doi.org/10.2514/2.3705.

[12] Reshotko, E., "Transition Issues at Hypersonic Speeds," *44th AIAA Aerospace Sciences Meeting and Exhibit*, American Institute of Aeronautics and Astronautics, 2006. https://doi.org/10.2514/6.2006-707.

[13] Fedorov, A., "Transition and Stability of High-Speed Boundary Layers," *Annual Review of Fluid Mechanics*, Vol. 43, 2011, pp. 79–95. https://doi.org/10.1146/annurev-fluid-122109-160750.

[14] Azzazy, M., Modarress, D., and Trolinger, J. D., "Feasibility Study of Optical Boundary Layer Transition Detection Method," NASA Contractor Report NASA-CR-178109, NASA Langley Research Center, Hampton, VA, 1986. URL https://ntrs.nasa.gov/api/citations/19860018903/downloads/19860018903.pdf.

[15] O'Hare, J. E., "A Nonperturbing Boundary-Layer Transition Detector," *High Speed Photography, Videography, and Photonics III*, Vol. Proc. SPIE 0569, 1986. https://doi.org/10.1117/12.949864.

[16] Salyer, T. R., Randall, L. A., Collicott, S. H., and Schneider, S. P., "Use of Laser Differential Interferometry to Study Receptivity on a Hemispherical Nose at Mach 4," *36th AIAA Aerospace Sciences Meeting and Exhibit*, American Institute of Aeronautics and Astronautics, 1998. https://doi.org/10.2514/6.1998-238.

[17] Salyer, T. R., Collicott, S. H., and Schneider, S. P., "Feedback Stabilized Laser Differential Interferometry for Supersonic Blunt Body Receptivity Experiments," *38th Aerospace Sciences Meeting and Exhibit*, American Institute of Aeronautics and Astronautics, 2000. https://doi.org/10.2514/6.2000-416.

[18] Parziale, N. J., Shepherd, J. E., and Hornung, H. G., "Differential Interferometric Measurement of Instability in a Hypervelocity Boundary Layer," *AIAA Journal*, Vol. 51, No. 3, 2013, pp. 750–753. https://doi.org/10.2514/1.J052013.

[19] Parziale, N. J., "Slender-Body Hypervelocity Boundary-Layer Instability," Ph.D. Dissertation, California Institute of Technology, 2013. https://doi.org/10.7907/KZJ1-Y009.

[20] Parziale, N. J., Shepherd, J. E., and Hornung, H. G., "Free-stream density perturbations in a reflected-shock tunnel," *Experiments in Fluids*, Vol. 55, No. 1665, 2014. https://doi.org/10.1007/s00348-014-1665-0.

[21] Parziale, N. J., Shepherd, J. E., and Hornung, H. G., "Observations of hypervelocity boundary-layer instability," *Journal of Fluid Mechanics*, Vol. 781, 2015, pp. 87–112. https://doi.org/10.1017/jfm.2015.489.

[22] Mack, L. M., "Boundary-Layer Linear Stability Theory," Tech. Rep. AGARD Report No. 709, Part 3, California Institute of Technology, Jet Propulsion Laboratory, 1984.

[23] Neet, M. C., Lawson, J. M., and Austin, J. M., "Design, alignment, and calibration of a focused laser differential interferometer," *Applied Optics*, Vol. 60, No. 26, 2021, pp. 7903–7909. https://doi.org/10.1364/AO.435112.

[24] Fulghum, M. R., "Turbulence Measurements in High-Speed Wind Tunnels using Focusing Laser Differential Interferometry," Ph.D. Dissertation, The Pennsylvania State University, 2014.

[25] Settles, G. S., and Fulghum, M. R., "The Focusing Laser Differential Interferometer, an Instrument for Localized Turbulence Measurements in Refractive Flows," *Journal of Fluids Engineering*, Vol. 138, No. 10, 2016. https://doi.org/10.1115/1.4033960.

[26] Chou, A., Leidy, A. N., Bathel, B. F., King, R. A., and Herring, G. C., "Measurements of Freestream Fluctuations in the NASA Langley 20-Inch Mach 6 Tunnel," *2018 Fluid Dynamics Conference, AIAA AVIATION Forum*, American Institute of Aeronautics and Astronautics, 2018. https://doi.org/10.2514/6.2018-3073.

[27] Birch, B., Buttsworth, D., and Zander, F., "Measurements of freestream density fluctuations in a hypersonic wind tunnel," *Experiments in Fluids*, Vol. 61, No. 158, 2020. https://doi.org/10.1007/s00348-020-02992-w.

[28] Bathel, B. F., Herring, G. C., Weisberger, J. M., Chou, A., and Jones, S. B., "Simultaneous focused laser differential interferometry and high-speed schlieren in a Mach 6 flow," *Measurement Science and Technology*, Vol. 32, No. 9, 2021. https://doi.org/10.1088/1361-6501/abf67a.

[29] Kerth, P., "Effect of Transpiration Cooling on Boundary Layer Transition for Hypersonic Flight," Ph.D. Dissertation, University of Oxford, 2022.

[30] Gragston, M., "FLDI Ray Trace and Calculator," , 2024. URL https://www.mathworks.com/matlabcentral/fileexchange/173800-fldi-ray-trace-and-calculator.

[31] Lawson, J. M., Neet, M. C., Grossman, I. J., and Austin, J. M., "Characterization of a Focused Laser Differential Interferometer," *AIAA SciTech 2019 Forum*, American Institute of Aeronautics and Astronautics, 2019. https://doi.org/10.2514/6.2019-2296.

[32] Ramprakash, A., McIntyre, T. J., Wheatley, V., and Mee, D. J., "Performance Analysis of FLDI Technique using Turbulent Jets," *IX Australian Conference on Laser Diagnostics*, 2019.

[33] Gragston, M., Price, T., Davenport, K., Zhang, Z., and Schmisseur, J. D., "Linear array focused-laser differential interferometry for single-shot multi-point flow disturbance measurements," *Optics Letters*, Vol. 46, No. 1, 2021, pp. 154–157. https://doi.org/10.1364/OL.412495.

[34] Hopkins, K. J., Porat, H., McIntyre, T. J., Wheatley, V., and Veeraragavan, A., "Measurements and analysis of hypersonic tripped boundary layer turbulence," *Experiments in Fluids*, Vol. 62, No. 164, 2021. https://doi.org/10.1007/s00348-021-03254-z.

[35] Gillespie, G. I., Ceruzzi, A. P., and Laurence, S. J., "A multi-point focused laser differential interferometer for characterizing freestream disturbances in hypersonic wind tunnels," *Experiments in Fluids*, Vol. 63, No. 180, 2022. https://doi.org/10.1007/s00348-022-03522-6.

[36] Huang, R., Liu, W., Cheng, J., and Wun, J., "Measurement of hypersonic turbulent boundary layer on a flat plate using cylindrical focused laser differential interferometer," *Physics of Fluids*, Vol. 35, No. 3, 2023. https://doi.org/10.1063/5.0141681.

[37] Lunte, J., and Schülein, E., "Wall normal focused laser differential interferometry for measurements of flow disturbances on flat-plate models," *AIAA AVIATION 2023 Forum*, American Institute of Aeronautics and Astronautics, 2023. https://doi.org/10.2514/6.2023-3449.

[38] Hopkins, K. J., Ananthapadmanaban, R., McIntyre, T. J., Mee, D. J., Wheatley, V., and Veeraragavan, A., "Experimental Verification of a Modified Cylindrical Focused Laser Differential Interferometer," *Journal of Spacecraft and Rockets*, Vol. 61, No. 5, 2024, pp. 1194–1203. https://doi.org/10.2514/1.a35842.

[39] Lunte, J., and Schülein, E., "Wall-Normal Focused Laser Differential Interferometry," *AIAA Journal*, Vol. 62, No. 4, 2024, pp. 1366–1374. https://doi.org/10.2514/1.J063258.

[40] Wagner, G. P. C. A., "A low-effort and inexpensive methodology to determine beam separation distance of multi-foci FLDI," *Experiments in Fluids*, Vol. 63, No. 53, 2022. https://doi.org/10.1007/s00348-022-03401-0.

[41] Ceruzzi, A. P., and Cadou, C. P., "Turbulent Air Jet Investigation using Focused Laser Differential Interferometry," *53rd AIAA/SAE/ASEE Joint Propulsion Conference*, American Institute of Aeronautics and Astronautics, 2017. https://doi.org/10.2514/6.2017-4834.

[42] Ceruzzi, A. P., and Cadou, C. P., "Simultaneous Velocity and Density Gradient Measurements using Two-Point Focused Laser Differential Interferometry," *AIAA SciTech 2019 Forum*, American Institute of Aeronautics and Astronautics, 2019. https://doi.org/10.2514/6.2019-2295.

[43] Kawata, S., Shimamura, K., Suzuki, S., Manoharan, R., and Tanno, H., "Hypersonic boundary transition measurement by Focused Laser Differential Interferometry in high-enthalpy shock tunnel HIEST," *AIAA SciTech 2022 Forum*, American Institute of Aeronautics and Astronautics, 2022. https://doi.org/10.2514/6.2022-0733.

[44] Weisberger, J. M., Bathel, B. F., Herring, G. C., King, R. A., Chou, A., and Jones, S. B., "Two-Point Focused Laser Differential Interferometry Second-Mode Measurements at Mach 6," *AIAA AVIATION 2019 Forum*, American Institute of Aeronautics and Astronautics, 2019. https://doi.org/10.2514/6.2019-2903.

[45] Bathel, B. F., Weisberger, J. M., Herring, G. C., King, R. A., Jones, S. B., Kennedy, R. E., and Laurence, S. J., "Two-point, parallel-beam focused laser differential interferometry with a Nomarski prism," *Applied Optics*, Vol. 59, No. 2, 2020, pp. 244–252. https://doi.org/10.1364/AO.59.000244.

[46] Benitez, E. K., Jewell, J. S., and Schneider, S. P., "Focused Laser Differential Interferometry for Hypersonic Flow Instability Measurements with Contoured Tunnel Windows," *AIAA SciTech 2020 Forum*, American Institute of Aeronautics and Astronautics, 2020. https://doi.org/10.2514/6.2020-1282.

[47] Weisberger, J. M., Bathel, B. F., Herring, G. C., Buck, G. M., Jones, S. B., and Cavone, A. A., "Multi-point line focused laser differential interferometer for high-speed flow fluctuation measurements," *Applied Optics*, Vol. 59, No. 35, 2020, pp. 11180–11195. https://doi.org/10.1364/AO.411006.

[48] Bathel, B. F., Weisberger, J. M., Herring, G. C., Jagannathan, R., Johansen, C. T., Jones, S. B., and Cavone, A. A., "Analysis of the Amplitude Response of a Two-Point and a Multi-Point Focused Laser Differential Interferometer," *AIAA SciTech 2021 Forum*, American Institute of Aeronautics and Astronautics, 2021. https://doi.org/10.2514/6.2021-0598.

[49] Benitez, E. K., Jewell, J. S., and Schneider, S. P., "Focused Laser Differential Interferometry with Contoured Tunnel Windows," *AIAA Journal*, Vol. 59, No. 2, 2021, pp. 419–429. https://doi.org/10.2514/1.J060081.

[50] Weisberger, J. M., Bathel, B. F., Herring, G. C., Buck, G. M., Jones, S. B., and Cavone, A. A., "Two-Line Focused Laser Differential Interferometry of a Flat Plate Boundary Layer at Mach 6," *AIAA SciTech 2021 Forum*, American Institute of Aeronautics and Astronautics, 2021. https://doi.org/10.2514/6.2021-0601.

[51] Weisberger, J. M., Bathel, B. F., Lee, J. W., and Cavone, A. A., "Linear Array Photodiode and Data Acquisition System Development for Multi-Point Line FLDI Measurements," *AIAA SciTech 2022 Forum*, American Institute of Aeronautics and Astronautics, 2022. https://doi.org/10.2514/6.2022-1796.

[52] Weisberger, J. M., and Bathel, B. F., "Colinear focused laser differential interferometry and self-aligned focusing schlieren," *Applied Optics*, Vol. 62, No. 18, 2023, pp. 4958–4970. https://doi.org/10.1364/AO.489897.

[53] Weisberger, J. M., Herring, G. C., Bathel, B. F., and Chou, A., "Absorption Laser Differential Interferometry for Simultaneous Colinear Flow Property and Fluctuation Measurements," *AIAA AVIATION 2023 Forum*, American Institute of Aeronautics and Astronautics, 2023. https://doi.org/10.2514/6.2023-4369.

[54] Weisberger, J. M., Bathel, B. F., and Herring, G. C., "Characterization Progress of an Absorption Laser Differential Interferometer," *AIAA SciTech 2024 Forum*, American Institute of Aeronautics and Astronautics, 2024. https://doi.org/10.2514/6.2024-1930.

[55] Houpt, A., and Leonov, S., "Focused Laser Differential Interferometer for Supersonic Boundary Layer Measurements on Flat Plate Geometries," *2018 Plasmadynamics and Lasers Conference, AIAA AVIATION Forum*, American Institute of Aeronautics and Astronautics, 2018. https://doi.org/10.2514/6.2018-3434.

[56] Houpt, A., and Leonov, S., "Focused and Cylindrical-Focused Laser Differential Interferometer Characterization of SBR-50 at Mach 2," *AIAA AVIATION 2019 Forum*, American Institute of Aeronautics and Astronautics, 2019. https://doi.org/10.2514/6.2019-3383.

[57] Houpt, A., and Leonov, S., "Cylindrical Focused Laser Differential Interferometer," *AIAA Journal*, Vol. 59, No. 4, 2021, pp. 1142–1150. https://doi.org/10.2514/1.J059750.

[58] Chism, J. R., Gragston, M., Riley, Z., Spottswood, M., Perez, R., and Hagen, B. J., "Cylindrical and Spherical Lens Linear Array-Focused Laser Differential Interferometry on a Flat Plate at Mach 6," *AIAA SciTech 2022 Forum*, American Institute of Aeronautics and Astronautics, 2022. https://doi.org/10.2514/6.2022-1659.

[59] Chism, J. R., Gragston, M., Peltier, S., and McManus, T., "Camera-Based Detection of FLDI for Measurements in High-Speed Turbulent Boundary Layers," *AIAA AVIATION 2022 Forum*, American Institute of Aeronautics and Astronautics, 2022. https://doi.org/10.2514/6.2022-3474.

[60] Chism, J. R., Shoppell, Z., Gragston, M., and Kreth, P. A., "Camera-Based Detection of Cylindrical Lens Based Focused Laser Differential Interferometry," *AIAA SciTech 2024 Forum*, American Institute of Aeronautics and Astronautics, 2024. https://doi.org/10.2514/6.2024-2125.

[61] Hameed, A., Parziale, N. J., Paquin, L., Butler, C., and Laurence, S. J., "Spectral Analysis of a Hypersonic Boundary Layer on a Right, Circular Cone," *AIAA SciTech 2020 Forum*, American Institute of Aeronautics and Astronautics, 2020. https://doi.org/10.2514/6.2020-0362.

[62] Hameed, A., and Parziale, N. J., "Focused Laser Differential Interferometer Response to a Controlled Phase Object," *AIAA SciTech 2021 Forum*, American Institute of Aeronautics and Astronautics, 2021. https://doi.org/10.2514/6.2021-0602.

[63] Xiong, Y., Zhao, L., and Wu, J., "Characterization of Disturbance Resonance in Postshock of Blunt Body in Hypersonic Flow," *AIAA Journal*, Vol. 61, No. 9, 2023, pp. 3735–3742. https://doi.org/10.2514/1.j062615.

[64] Chen, J. H., Hameed, A., Parziale, N. J., Roy, D., and Duan, L., "Spectral Analysis of Mach 6 Turbulent Boundary Layer over a Hollow Cylinder with FLDI and DNS," *AIAA SciTech 2024 Forum*, American Institute of Aeronautics and Astronautics, 2024. https://doi.org/10.2514/6.2024-2734.

[65] Siddiqui, F., Gragston, M., Saric, W. S., and Bowersox, R. D. W., "Mack-mode instabilities on a cooled flared cone with discrete roughness elements at Mach 6," *Experiments in Fluids*, Vol. 62, No. 213, 2021. https://doi.org/10.1007/s00348-021-03304-6.

[66] Davenport, K., and Gragston, M., "Simultaneous Turbulent Boundary Layer Velocity Profile and Scalar Turbulence Spectra with Linear Array-FLDI," *AIAA SciTech 2022 Forum*, American Institute of Aeronautics and Astronautics, 2022. https://doi.org/10.2514/6.2022-1313.

[67] Siddiqui, F., Bowersox, R. D. W., and Gragston, M., "Measurements of the Influence of Wall Cooling on Boundary-Layer Transition on a Flared Cone at Mach 6 using Focused Laser Differential Interferometry," *AIAA SciTech 2022 Forum*, American Institute of Aeronautics and Astronautics, 2022. https://doi.org/10.2514/6.2022-1825.

[68] Davenport, K., and Gragston, M., "Simultaneous Velocity Profile and Scalar Spectra with Linear Array-Focused Laser Differential Interferometry," *AIAA Journal*, Vol. 61, No. 2, 2023, pp. 934–939. https://doi.org/10.2514/1.J061945.

[69] Davenport, K., Ledbetter, S., Siddiqui, F., and Gragston, M., "Development of a Simple Compact Photodiode Array for use with Linear Array-FLDI," *AIAA SciTech 2023 Forum*, American Institute of Aeronautics and Astronautics, 2023. https://doi.org/10.2514/6.2023-1563.

[70] Constantin, R. U., Edwards, S. C., Webber, N., and Gragston, M., "Demonstrating a Multi-Depth Focused Laser Differential Interferometer Based on Chromatic Dispersion," *AIAA AVIATION Forum and ASCEND 2024*, American Institute of Aeronautics and Astronautics, 2024. https://doi.org/10.2514/6.2024-4271.

[71] Webber, N., Constantin, R., Edwards, S., and Gragston, M., "Multi-depth focused laser differential interferometer based on chromatic aberration," *Applied Optics*, Vol. 63, No. 5, 2024, pp. 1196–1203. https://doi.org/10.1364/AO.507723.

[72] Ceruzzi, A. P., Callis, B. O., Weber, D. C., and Cadou, C. P., "Application of Focused Laser Differential Interferometry (FLDI) in a Supersonic Boundary Layer," *AIAA SciTech 2020 Forum*, American Institute of Aeronautics and Astronautics, 2020. https://doi.org/10.2514/6.2020-1973.

[73] Ceruzzi, A. P., McManamen, B., and Cadou, C. P., "Demonstration of Two-Point Focused Laser Differential Interferometry (2pFLDI) in a Mach 18 flow," *AIAA SciTech 2021 Forum*, American Institute of Aeronautics and Astronautics, 2021. https://doi.org/10.2514/6.2021-0983.

[74] Ceruzzi, A. P., Neisess, C., McManamen, B., and Cadou, C. P., "Investigation of Focused Laser Differential Interferometry (FLDI) Sensitivity Function," *AIAA SciTech 2021 Forum*, American Institute of Aeronautics and Astronautics, 2021. https://doi.org/10.2514/6.2021-1299.

[75] Ceruzzi, A. P., and Cadou, C. P., "Interpreting single-point and two-point focused laser differential interferometry in a turbulent jet," *Experiments in Fluids*, Vol. 63, No. 112, 2022. https://doi.org/10.1007/s00348-022-03459-w.

[76] Holladay, S., and Zhang, Z., "Supersonic and Plasma Flow Characterization by 1D Focused Laser Differential Interferometry," *AIAA SciTech 2022 Forum*, American Institute of Aeronautics and Astronautics, 2022. https://doi.org/10.2514/6.2022-0424.

[77] Holladay, S., and Zhang, Z., "Linear and 2D arrays for Focused Laser Differential Interferometry using a high-speed camera," *Optics Communications*, Vol. 546, 2023. https://doi.org/10.1016/j.optcom.2023.129754.

[78] Holladay, S., and Zhang, Z., "Programmable focused laser differential interferometer with a spatial light modulator as a dynamic diffractive optical element," *Optics Letters*, Vol. 48, No. 19, 2023, pp. 5001–5004. https://doi.org/10.1364/OL.496541.

[79] Price, T. J., Gragston, M., Schmisseur, J. D., and Kreth, P. A., "Measurement of supersonic jet screech with focused laser differential interferometry," *Applied Optics*, Vol. 59, No. 28, 2020, pp. 8902–8908. https://doi.org/10.1364/AO.402011.

[80] Cobourn, J. W., and Schmisseur, J. D., "Focused Laser Differential Interferometry Combined with Schlieren on Hypersonic Hollow Cylinder Flare and Hollow Cylinder Configurations," *AIAA SciTech 2021 Forum*, American Institute of Aeronautics and Astronautics, 2021. https://doi.org/10.2514/6.2021-0369.

[81] Gragston, M., Price, T. J., Davenport, K., Schmisseur, J. D., and Zhang, Z., "An m $\times$ n FLDI Array for Single-Shot, Multipoint Disturbance Measurements in High-Speed Flows," *AIAA SciTech 2021 Forum*, American Institute of Aeronautics and Astronautics, 2021. https://doi.org/10.2514/6.2021-0599.

[82] Gragston, M., Siddiqui, F., and Schmisseur, J. D., "Detection of second-mode instabilities on a flared cone in Mach 6 quiet flow with linear array focused laser differential interferometry," *Experiments in Fluids*, Vol. 62, No. 81, 2021. https://doi.org/10.1007/s00348-021-03188-6.

[83] Price, T. J., Gragston, M., and Kreth, P. A., "Spatially-Resolved Optical Detection of Jet Screech in a Mach 1.5 Underexpanded Jet with Focused-Laser Differential Interferometry," *AIAA SciTech 2021 Forum*, American Institute of Aeronautics and Astronautics, 2021. https://doi.org/10.2514/6.2021-0600.

[84] Gragston, M., Schmisseur, J. D., and Siddiqui, F., "Measurements of Second-Mode Instabilities with Linear Array-Focused Laser Differential Interferometry," *AIAA SciTech 2022 Forum*, American Institute of Aeronautics and Astronautics, 2022. https://doi.org/10.2514/6.2022-1824.

[85] Jiang, N., Hsu, P. S., Slipchenko, M., Roy, S., Lauriola, D. K., Webb, A. M., Meyer, T. R., Gragston, M., Parker, R., Portoni, P., McDemortt, C., Seitz, K., and Wadhams, T. P., "MHz Rate Flow Diagnostics in CUBRC Mach 10 Shock Tunnel," *AIAA SciTech 2022 Forum*, American Institute of Aeronautics and Astronautics, 2022. https://doi.org/10.2514/6.2022-1655.

[86] Price, T. J., Gragston, M., and Kreth, P. A., "Analysis of Screech Phenomena in a Mach 1.0 Jet with Linear Array Focused Laser Differential Interferometry," *AIAA SciTech 2022 Forum*, American Institute of Aeronautics and Astronautics, 2022. https://doi.org/10.2514/6.2022-1798.

[87] Dean, T. S., Bowersox, R. D. W., Siddiqui, F., and Gragston, M., "Index of Refraction Fluctuation Spectra in Aerothermochemical Non-equilibrium Shock Layers," *AIAA SciTech 2023 Forum*, American Institute of Aeronautics and Astronautics, 2023. https://doi.org/10.2514/6.2023-0270.

[88] Gillespie, G. I., Ceruzzi, A. P., and Laurence, S. J., "Multi-point Focused Laser Differential Interferometry for Noise Measurements in High-Speed Tunnels," *AIAA AVIATION 2021 FORUM*, American Institute of Aeronautics and Astronautics, 2021. https://doi.org/10.2514/6.2021-2918.

[89] Maszkiewicz, S. A., Gillespie, G. I., and Laurence, S. J., "Experimental Investigation of Transitional, Sharp-Fin-Induced Shock-Wave/Boundary-Layer Interactions at Mach 6," *AIAA SciTech 2022 Forum*, American Institute of Aeronautics and Astronautics, 2022. https://doi.org/10.2514/6.2022-1818.

[90] Sanderson, S. R., "Simple, adjustable beam splitting element for differential interferometers based on photoelastic birefringence of a prismatic bar," *Review of Scientific Instruments*, Vol. 76, No. 11, 2005. https://doi.org/10.1063/1.2132271.

[91] Berger, A. R., and Borg, M. P., "Co-linear FLDI/Schlieren and Surface Pressure Measurements of Bluntness Induced Elongated Structures in Hypersonic Flow," *AIAA SciTech 2023 Forum*, American Institute of Aeronautics and Astronautics, 2023. https://doi.org/10.2514/6.2023-0473.

[92] Camillo, G. P., Wagner, A., Toki, T., and Scalo, C., "Combined Experimental and Numerical Investigation of a Hypersonic Turbulent Boundary Layer by Means of FLDI and Large-Eddy Simulations," *Aerospace*, Vol. 10, No. 6, 2023. https://doi.org/10.3390/aerospace10060570.

[93] Camillo, G. P., and Wagner, A., "Focused laser differential interferometry post-processing methodology for flowfields with circular symmetry," *Review of Scientific Instruments*, Vol. 94, No. 4, 2023. https://doi.org/10.1063/5.0132874.

[94] Marsh, A. W., Kramer, A. N., Maranto, K. N., and Mazumdar, Y. C., "Imaging focused laser differential interferometry," *Optics Letters*, Vol. 49, No. 8, 2024, pp. 2109–2112. https://doi.org/10.1364/OL.520660.

[95] Smeets, G., "Verwendung eines Laser-Differentialinterferometers zur Bestimmung lokaler Schwankungsgroißen sowie des mittleren Dichteprofils in einem turbulenten Freistrahl," Tech. Rep. 20/74, Institute Franco-Allemand de Recherches de Saint-Louis, 1974.

[96] Schmidt, B. E., and Shepherd, J. E., "Analysis of focused laser differential interferometry," *Applied Optics*, Vol. 54, No. 28, 2015, pp. 8459–8472. https://doi.org/10.1364/AO.54.008459.

[97] Lawson, J. M., "Focused Laser Differential Interferometry," Ph.D. Dissertation, California Institute of Technology, 2021. https://doi.org/10.7907/5thh-f652.

[98] Born, M., and Wolf, E., *Principles of Optics, 7th ed.*, Cambridge University Press, 1999. https://doi.org/10.1017/CBO9781139644181.

[99] Hameed, A., and Parziale, N. J., "Focused Laser Differential Interferometric Investigation of Turbulent Jet Spectra," *Journal of Spacecraft and Rockets*, Vol. 59, No. 5, 2022, pp. 1565–1573. https://doi.org/10.2514/1.A35292.

[100] Siegman, A., *Lasers*, University Science Books, 1986.

[101] Lawson, J. M., and Austin, J. M., "Recovering density disturbance spectra from FLDI. Part 1," *Applied Optics*, Vol. 62, No. 12, 2023, pp. 3042–3053. https://doi.org/10.1364/AO.480352.

[102] Lawson, J. M., and Austin, J. M., "Recovering density disturbance spectra from FLDI. Part 2: comparisons with previous methods," *Applied Optics*, Vol. 62, No. 12, 2023, pp. 3054–3061. https://doi.org/10.1364/AO.480354.

[103] Gladstone, J. H., and Dale, T. P., "XIV. Researches on the refraction, dispersion, and sensitiveness of liquids," *Philosophical Transactions*, Vol. 153, 1863. https://doi.org/10.1098/rstl.1863.0014.

[104] Lawson, J. M., Neet, M. C., Grossman, I. J., and Austin, J. M., "Static and dynamic characterization of a focused laser differential interferometer," *Experiments in Fluids*, Vol. 61, No. 187, 2020. https://doi.org/10.1007/s00348-020-03013-6.

[105] Lawson, J. M., Neet, M. C., Hofferth, J. W., and Austin, J. M., "Supersonic Freestream Density Fluctuations from Focused Laser Differential Interferometry and Pitot-Probe Measurements," *AIAA Journal*, Vol. 60, No. 9, 2022, pp. 5173–5186. https://doi.org/10.2514/1.J061432.

[106] Benitez, E. K., Borg, M. P., Hill, J. L., Aultman, M. T., Duan, L., Running, C. L., and Jewell, J. S., "Quantitative focused laser differential interferometry with hypersonic turbulent boundary layers," *Applied Optics*, Vol. 61, No. 31, 2022, pp. 9203–9216. https://doi.org/10.1364/AO.465714.

[107] Ananthapadmanaban, R., McIntyre, T. J., Wheatley, V., and Mee, D. J., "Noise Generated in a Scramjet Combustor," *Journal of Spacecraft and Rockets*, Vol. 61, No. 4, 2024, pp. 1006–1018. https://doi.org/10.2514/1.A35779.

[108] Lawson, J. M., and Austin, J. M., "Focused laser differential interferometer response to shock waves," *Measurement Science and Technology*, Vol. 32, No. 5, 2021. https://doi.org/10.1088/1361-6501/abdbd3.

[109] Benitez, E. K., Leger, T. J., Tufts, M. W., Hill, J. L., and Borg, M. P., "Hypersonic Transitional Boundary-Layer Measurements using a Linear-Array FLDI," *AIAA Aviation 2023 Forum*, American Institute of Aeronautics and Astronautics, 2023. https://doi.org/10.2514/6.2023-4253.

[110] Ceruzzi, A. P., "Development of Two-Point Focused Laser Differential Interferometry for Applications in High-Speed Wind Tunnels," Ph.D. Dissertation, University of Maryland, College Park, 2022. URL https://www.proquest.com/docview/2681845978/abstract/C18090FBB3034797PQ/1.

[111] Benitez, E. K., Borg, M. P., Rhodes, C., and Jewell, J. S., "Optical-Axis Spatial Sensitivity of a Simulated Focused Laser Differential Interferometer," *AIAA Journal*, Vol. 61, No. 5, 2023, pp. 1925–1938. https://doi.org/10.2514/1.J062270.

[112] Benitez, E. K., Aultman, M., Duan, L., Camillo, G. P., and Jewell, J. S., "Significance of the smaller scales for hypersonic turbulent boundary layers with focused laser differential interferometry," *Physics of Fluids*, Vol. 36, No. 11, 2024.

[113] Ceruzzi, A. P., Page, L. M. L., Kerth, P., Williams, B. A. O., and McGilvray, M., "Simultaneous measurements of freestream disturbances, boundary layer instabilities and transition location on moderately blunt cones," *AIAA SciTech 2024 Forum*, American Institute of Aeronautics and Astronautics, 2024. https://doi.org/10.2514/6.2024-2187.

[114] Jewell, J. S., Parziale, N. J., Lam, K.-Y., Hagen, B. J., and Kimmel, R. L., "Disturbance and Phase Speed Measurements for Shock Tubes and Hypersonic Boundary-Layer Instability," *32nd AIAA Aerodynamic Measurement Technology and Ground Testing Conference, AIAA AVIATION Forum*, American Institute of Aeronautics and Astronautics, 2016. https://doi.org/10.2514/6.2016-3112.

[115] Jewell, J. S., Hameed, A., Parziale, N. J., and Gogineni, S., "Disturbance Speed Measurements in a Circular Jet via Double Focused Laser Differential Interferometry," *AIAA SciTech 2019 forum*, American Institute of Aeronautics and Astronautics, 2019. https://doi.org/10.2514/6.2019-2293.

[116] Lin, C. C., "On Taylor's Hypothesis and the Acceleration Terms in the Navier-Stokes Equations," *Quarterly of Applied Mathematics*, Vol. 10, No. 4, 1953, pp. 295–306. https://doi.org/10.1142/9789814415651_0011.

[117] Taylor, G. I., "The spectrum of turbulence," *Proceedings of the Royal Society of London. Series A - Mathematical and Physical Sciences*, Vol. 164, No. 919, 1938, pp. 476–490. https://doi.org/10.1098/rspa.1938.0032.

[118] Allen, R. D., David, G. B., and Nomarski, G., "The Zeiss-Nomarski differential interference equipment for transmitted-light microscopy," *Zeitschrift für wissenschaftliche Mikroskopie und mikroskopische Technik*, Vol. 69, No. 4, 1969, pp. 193–221.

[119] Gui, Y., Zhang, C., Li, X., Xu, D., and Wu, J., "Hypersonic boundary-layer instability characterization and transition downstream of distributed roughness," *Experiments in Fluids*, Vol. 64, No. 159, 2023. https://doi.org/10.1007/s00348-023-03703-x.

[120] Siddiqui, F., Ledbetter, S., Shine, J., Bowersox, R. D. W., and Gragston, M., "Correlated off-body density fluctuations and surface heating in hypersonic boundary layer transition," *Experiments in Fluids*, Vol. 64, No. 171, 2023. https://doi.org/10.1007/s00348-023-03716-6.

[121] Huang, R., Xue, T., and Wu, J., "Measurement of the Convection Velocities in a Hypersonic Turbulent Boundary Layer Using Two-Point Cylindrical-Focused Laser Differential Interferometer," *Aerospace*, Vol. 11, No. 1, 2024. https://doi.org/10.3390/aerospace11010100.

[122] Optical Society of America, *Handbook of Optics, Vol. 2: Devices, Measurements, and Properties*, 2nd ed., Vol. 2, McGraw-Hill, Inc., 1995.

[123] Brasen, G., Laue, C., and Loeffler, M., "Polarizing Beamsplitter," U.S. Patent 7,167,311, United States of America, 2007.

[124] Pandey, A., Casper, K. M., Guildenbecher, D. R., Beresh, S. J., Bhakta, R., DeZetter, M. E., and Spillers, R., "Instability Measurements in Hypersonic Flow on a Three-Dimensional Cone-Slice-Ramp Geometry," *AIAA SciTech 2022 Forum*, American Institute of Aeronautics and Astronautics, 2022. https://doi.org/10.2514/6.2022-1578.

[125] Xu, Z., Chai, Y., Ma, L., and Zhu, Y., "The visualization of an ultrasonic standing wave field using scanning-focused laser differential interferometry," *Physics of Fluids*, Vol. 36, No. 7, 2024. https://doi.org/10.1063/5.0214856.

[126] Siddiqui, F., Gragston, M., and Bowersox, R. D. W., "Measurement of Wall-Cooling Effects on Hypersonic Boundary-Layer Transition Using Focused Laser Differential Interferometry," *AIAA Journal*, Vol. 60, No. 11, 2022, pp. 6214–6224. https://doi.org/10.2514/1.J061756.

[127] Weisberger, J. M., Bathel, B. F., Herring, G. C., and Page Jr., W. E., "Modification of Mach 6 Freestream Flow by Pitot Probe Bow Shock as Measured by Line FLDI and SAFS," *AIAA SciTech 2025 Forum*, American Institute of Aeronautics and Astronautics, 2025. Accepted for Presentation.

[128] Benitez, E. K., Borg, M. P., Hill, J. L., Davami, J., and Juliano, T. J., "Nosetip Bluntness Effects on the ROTEX-T Cone-Flare," *AIAA AVIATION Forum and ASCEND 2024*, American Institute of Aeronautics and Astronautics, 2024. https://doi.org/10.2514/6.2024-3638.

[129] Hameed, A., Shekhtman, D., Parziale, N. J., Paquin, L., Skinner, S. N., Laurence, S. J., Yu, W. M., and Austin, J. M., "Hypersonic Boundary-Layer Instability on a Highly Cooled Cone. Part I: Q-FLDI Measurement and Instability Calculations," *AIAA SciTech 2022 Forum*, American Institute of Aeronautics and Astronautics, 2022. https://doi.org/10.2514/6.2022-0734.

[130] Hameed, A., Parziale, N. J., Paquin, L., Laurence, S. J., Yu, W. M., and Austin, J. M., "Characterization of Transitional, High-Enthalpy Boundary Layers on a Slightly-Blunted Cone. Part II: FLDI and Higher-Order Spectral Analysis," *AIAA SciTech 2023 Forum*, American Institute of Aeronautics and Astronautics, 2023. https://doi.org/10.2514/6.2023-0288.

[131] Oddo, R., Hill, J. L., Reeder, M. F., Chin, D., Embrador, J., Komives, J., Tufts, M., Borg, M., and Jewell, J. S., "Effect of surface cooling on second-mode dominated hypersonic boundary layer transition," *Experiments in Fluids*, Vol. 62, No. 144, 2021. https://doi.org/10.1007/s00348-021-03237-0.

[132] Benitez, E. K., "Instability Measurements on Two Cone-Cylinder-Flares at Mach 6," Ph.D. Dissertation, Purdue University, 2021. https://doi.org/10.25394/PGS.15050058.v1.

[133] Settles, G. S., and Fulghum, M. R., "The Focusing Laser Differential Interferometer, an Instrument for Localized Turbulence Measurements in Refractive Flows," *Journal of Fluids Engineering*, Vol. 138, No. 10, 2016. https://doi.org/10.1115/1.4033960.

[134] Lawson, J. M., and Austin, J. M., "Expansion Tube Freestream Disturbance Measurements using a Focused Laser Differential Interferometer," *AIAA SciTech 2020 Forum*, American Institute of Aeronautics and Astronautics, 2020. https://doi.org/10.2514/6.2020-1064.

[135] Chaudhry, R. S., Candler, G. V., Gray, K. A., and Schneider, S. P., "Computations of Measured Pitot-Probe Spectra using Angled Freestream Disturbances and Comparisons to Experiments," *AIAA SciTech 2019 Forum*, American Institute of Aeronautics and Astronautics, 2019. https://doi.org/10.2514/6.2019-2149.

[136] Laufer, J., "Some Statistical Properties of the Pressure Field Radiated by a Turbulent Boundary Layer," *Physics of Fluids*, Vol. 7, No. 8, 1964, pp. 1191–1197. https://doi.org/10.1063/1.1711360.

[137] Duan, L., Choudhari, M. M., Chou, A., Schilden, T., Schroder, W., Marineau, E. C., Casper, K. M., Chaudhry, R. S., Candler, G. V., Gray, K. A., and Schneider, S. P., "Characterization of Freestream Disturbances in Conventional Hypersonic Wind Tunnels," *Journal of Spacecraft and Rockets*, Vol. 56, No. 2, 2019, pp. 357–368. https://doi.org/10.2514/1.A34290.

[138] Ceruzzi, A. P., Kanapathipillai, M., Yu, K. H., and Cadou, C. P., "Non-intrusive velocimetry in a supersonic reacting flow using two-point focused laser differential interferometry," *AIAA SciTech 2023 Forum*, American Institute of Aeronautics and Astronautics, 2023. https://doi.org/10.2514/6.2023-0223.

[139] Bisek, N. J., and Brown, M. S., "Computational and Experimental Laser Differential Interferometry for Supersonic Turbulent Boundary-Layer Flow," *46th AIAA Plasmadynamics and Lasers Conference, AIAA AVIATION Forum*, American Institute of Aeronautics and Astronautics, 2015. https://doi.org/10.2514/6.2015-2802.

[140] Benitez, E. K., Borg, M. P., Dungan, S. D., Brehm, C., and Jewell, J. S., "Focused Laser Differential Interferometry Performance Over an Axisymmetric Model," *AIAA SciTech 2024 Forum*, American Institute of Aeronautics and Astronautics, 2024. https://doi.org/10.2514/6.2024-1931.

[141] Benitez, E. K., Borg, M. P., Dungan, S. D., Brehm, C., and Jewell, J. S., "Simulated Focused Laser Differential Interferometry of the Hypersonic Second-Mode Instability," *AIAA SciTech 2025 Forum*, American Institute of Aeronautics and Astronautics, 2025. Accepted for Presentation.

[142] Berger, A. R., and Borg, M. P., "Study of Bluntness-Induced Elongated Structures using Variable Beam Separation FLDI," *AIAA AVIATION 2023 Forum*, American Institute of Aeronautics and Astronautics, 2023. https://doi.org/10.2514/6.2023-3703.

[143] Wong, G., Pilkington, R., and Harvey, A. R., "Achromatization of Wollaston polarizing beam splitters," *Optics Letters*, Vol. 36, No. 8, 2011, pp. 1332–1334. https://doi.org/10.1364/ol.36.001332.

[144] Kudenov, M. W., Miskiewicz, M., Sanders, N., and Escuti, M. J., "Achromatic Wollaston prism beam splitter using polarization gratings," *Optics Letters*, Vol. 41, No. 19, 2016, pp. 4461–4463. https://doi.org/10.1364/ol.41.004461.

[145] Maisto, P. M. F., Martin, N. C., Francis, A., Laurence, S. J., and Papadopoulos, G., "Characterization of High-Frequency Acoustic Sources Using Laser Differential Interferometry," *AIAA SciTech 2021 Forum*, American Institute of Aeronautics and Astronautics, 2021. https://doi.org/10.2514/6.2021-0132.

[146] Elkowitz, L., Wanchek, A., Rockwell, R., Goyne, C. P., and Dedic, C. E., "Dual-mode scramjet control using optical emission sensors," *Applied Optics*, Vol. 63, No. 5, 2024, pp. 1355–1363. https://doi.org/10.1364/AO.507587.